Synthesis, Crystal Structures, and Chloride-ion Conducting Properties of Oxychlorides with Open Borate Frameworks

A Thesis

Submitted by

Yu MENG

In fulfillment for the award of the degree of

Doctor of Science

Graduate School of Chemical Sciences and Engineering,

Hokkaido University

2025

Abstract

Chloride-ion solid electrolytes have been widely investigated as the core components of membranes, gas sensors, and all-solid-state batteries with high energy densities. Several fast chloride-ion solid electrolytes operating at ambient-to-intermediate temperatures have been reported, ranging from inorganic metal chlorides and metal–organic compounds to complexes. However, these chlorides have the major drawback of being thermally and chemically unstable, and design strategies for chloride-ion conductors have not yet been developed compared with those for cation conducting solids, which restricts their practical applications. In contrast, a layered mixed-anion compound $La_{1-x}Ca_xOCl_{1-x}$ with a tetragonal matlockite-type structure possesses great structural stability against humidity and high temperature. Moreover, $La_{0.8}Ca_{0.2}OCl_{0.8}$ prepared via ball milling exhibited chloride-ion conductivity as high as 7×10^{-4} and 1×10^{-2} S cm^{-1} at 400 and 700 °C, respectively. However, making Cl^- transport dominant in mixed-anion sublattices, where the migration barrier for Cl^- ions tends to be higher than that for O^{2-} ions, remains a major challenge.

On the other hand, open borate frameworks are well known to exhibit a rich variety with 0D–3D dimensionality, which are mainly composed of triangular BO_3 and/or tetrahedral BO_4 units. Diverse open structures can be used to design ion migration pathways, and B–O covalent bonds can increase barriers to O^{2-} ions migration. Currently, compounds with open borate structures based on cationic conduction have been reported, including those with Li^+ and Na^+, but compounds based on Cl^- ions have not yet been reported. This study has explored new oxychloride compounds that show water insolubility and thermal stability, resulting in the discoveries of two types of compounds: $(Ca_{1-x}La_x)_2B_5O_9Cl_{1+2x}$ and $(La_{1-x}M_x)(BO_2)_2Cl_{1-x}$ (M = Ca, Sr) exhibit one-dimensional chloride-ion conduction and possible two-dimensional chloride-ion conduction, respectively. The synthesis, crystal structures, and chloride-ion conducting properties have been discussed.

Chapter 1 provides an overview of the research background, including the ion conductor principles and methods of conductivity calculation.

Chapter 2 mainly presents the experimental techniques used in this research.

Chapter 3 presents the investigation of La-doped $Ca_2B_5O_9Cl$, namely, $(Ca_{1-x}La_x)_2B_5O_9Cl_{1+2x}$, which crystallized in an orthorhombic symmetry with the space group of *Pnn*2. The crystal structure of $Ca_2B_5O_9Cl$ consists of $(BO_3)^{3-}$ triangles and $(BO_4)^{5-}$ tetrahedra. Two $(BO_3)^{3-}$ triangles and three $(BO_4)^{5-}$ tetrahedra are linked together by common vertexes to form $(B_5O_9)^{3-}$ open framework with tunnels filled with Ca^{2+} and Cl^- ions. In particular, the Cl^- ions are independently arranged along the *c* axis at a distance of 6.3500(3) Å between the nearest neighbour (NN) ions, which is much longer than those of fast chloride ion conductors. Therefore, the introduction of interstitial chloride ions is essential for facilitating Cl^- ion migration. Single crystal structure determination of a La-doped $Ca_2B_5O_9Cl$ with $x = 0.08$ revealed not only a substantial reduction in the occupancy of the original Cl site but also the presence of interstitial chloride ions within the Cl^- ions channel, resulting in a decrease in the distances between the NN Cl^- ions to lower than 2.10 Å. The $(Ca_{1-x}La_x)_2B_5O_9Cl_{1+2x}$ (x = 0–0.15) solid solutions exhibited the highest conductivity of 1.32×10^{-4} S cm^{-1} at 700 °C when $x = 0.05$. First-principles molecular dynamics simulations indicated that the predominant chloride-ion conduction is attributed to cooperative diffusion of Cl^- ions through the interstitialcy mechanism.

Chapter 4 presents the investigation of Ca or Sr doped $La(BO_2)_2Cl$, namely, $(La_{1-x}M_x)(BO_2)_2Cl_{1-x}$ (M = Ca, Sr), which crystallized in a triclinic symmetry with the space group of *P*–1. $La(BO_2)_2Cl$ consists of zigzag chains of corner-linked $(BO_3)^{3-}$ planar triangles, running along the *a* axis. These one-dimensional chains are separated by La^{3+} ions in the *ab* plane and by Cl along the *c* axis. In particular, the Cl^- ions are arranged in the *ab* plane at distances of 3.45–3.7 Å between the neighbouring ones, which are nearly close to those of fast

chloride ion conductors. Single crystal study of Ca/Sr-doped $La(BO_2)_2Cl$ with $x \sim 0.20$ revealed the presence of chloride ion vacancies, not oxygen vacancies. The $(La_{1-x}M_x)(BO_2)_2Cl_{1-x}$ (M = Ca, Sr, x = 0–0.15) solid solutions exhibited the highest conductivity of 1.84×10^{-4} S cm^{-1} at 700 °C when M = Ca and x = 0.10, and 7.59×10^{-4} S cm^{-1} at 700 °C when M = Sr and x = 0.15, respectively. Notably, the ionic conductivity of the Sr-doped phase was greater than that of La-doped $Ca_2B_5O_9Cl$ over the measured temperature range. The enhanced conductivity suggests possible two-dimensional chloride-ion conduction through the vacancy mechanism.

Chapter 5 presents the overall conclusions and future prospects based on this body of work.

Keywords: Flux synthesis, Solid state reaction, Chloride-ion conductor, Open borate framework, oxychloride.

List of Abbreviations

SSE	Solid state electrolytes
MOFs	Metal organic frameworks
R_i	Electrode-electrolyte interface resistance
R_{gb}	Grain boundary resistance
R_b	Bulk resistance
DC	Direct current
AC	Alternating current
Z	Impedance
CPE	Constant phase elements
σ_{DC}	Direct current conductivity
σ_{AC}	Alternating current conductivity
E_a	Activation energy
PXRD	Powder X-ray diffraction
SCXRD	Single crystal X-ray diffraction
EIS	Electrochemical impedance spectroscopy
TG	Thermal Gravimetric
DTA	Differential Thermal Analysis
SEM	Scanning electron microscope
EDX	Energy dispersive X-ray
BVS	Bond valance sum
DFT	Density Functional Theory

RMSD	Root mean square displacements
RSD	Root square displacements
NEB	Nudged elastic band
NIMS	National Institute for Materials Science
JFCC	Japan Fine Ceramics Center

Synthesis, Crystal Structures, and Chloride-ion Conducting Properties of Oxychlorides with Open Borate Frameworks

Contents

Chapter 1. Introduction

1.1 Solid state electrolyte

Solid state electrolytes (SSE) or ion-conducting solid, which can conduct a specific ion, have been extensively investigated for its wide range of applications such as gas sensors, separators, thermoelectric convertors, all-solid-state batteries and metal purification systems.[1–5] The types of solid electrolytes range from inorganic salts, polymers, and complexes to metal-organic frameworks. Compared with traditional liquid electrolytes, they always exhibit significant advantages in safety, chemical stability, and mechanical stability. Basically, mobile carriers are divided into cations such as Li^+ and Na^+ ions and anions such as $F^–$, $O^{2–}$ and $Cl^–$ ions. Table 1.1 shows some representative ion conductors and their ion conductivity. Recently, increasing attention has been paid to anion-conducting solid electrolytes, particularly for new types of rechargeable batteries that transfer anion charges. This thesis focuses on $Cl^–$ ions conductors because $Cl^–$ ions are not only abundant elemental resources available worldwide, but also offer the potential to create a new range of applications that differ considerably from conventional ones.

Table 1.1 Some representative ion conductors and their ion conductivity.

	Conductive species	Ion conductor	Ion conductivity (S cm^{-1})	
cationic conductors	Li^+	α-Li_3N	5.8×10^{-4}	25°C [6]
		$Li_{1.3}Al_{0.3}Ti_{1.7}(PO_4)_3$	7.0×10^{-4}	25°C [7]
		$Li_{14}Zn(GeO_4)_4$	1.3×10^{-1}	300°C [8]
	Na^+	Na_3PS_4 (cubic)	2.0×10^{-4}	25°C [9]
		$Na_2O\cdot11Al_2O_3$ (β-Al_2O_3)	3.3×10^{-2}	25°C [10]

		Na_2O-ZrO_2-P_2O_5-SiO_2	2.0×10^{-2}	300°C [11]
	K^+	K_2Fe_4O	5.0×10^{-2}	25°C [12]
		$K_{2.92}Sb_{0.92}W_{0.08}S_4$	1.4×10^{-4}	40°C [13]
	H^+	$Cs_3(HSO_4)_2(H_2PO_4)$	6.3×10^{-3}	120°C [14]
		$Cs_XH_{3-X}PMo_{12}O_{40}$	1.0×10^{-3}	280°C [15]
anionic conductors	F^-	LaF_3	3.0×10^{-6}	25°C [16]
		SrF_2	5.0×10^{-3}	850°C [17]
		CaF_2	1.4×10^{-3}	800°C [17]
	O^{2-}	$Bi_2V_{0.9}Cu_{0.1}O_{5.35}$	1.8×10^{-2}	400°C [18]
		$Ce_{0.9}Gd_{0.1}O_{1.95}$	4.6×10^{-2}	700°C [19]
		$Sr_3Sc_2O_5Cl_2$	5.6×10^{-6}	650°C [20]
	H^-	$La_{0.7}Sr_{1.3}LiH_2O_2$	1.2×10^{-2}	300°C [21]
		$LaH_{2.52}O_{0.42}$	2.6×10^{-2}	340°C [22]
		BaH_2	5.0×10^{-3}	420°C [23]
	Cl^-	$SnCl_2$	2.0×10^{-2}	200°C [24]
		$Pb_{0.98}K0_{.02}Cl_{1.98}$	2.3×10^{-4}	160°C [25]
		$La_{0.8}Ca_{0.2}OCl_{0.8}$	1.9×10^{-2}	800°C [26]

1.1.1 Chloride-ion conductor

At present, the variety of chloride-ion conducting solid electrolytes is poor in comparison with a rich variety of cation-conducting solid electrolytes.[27–29] However, chlorine is the third largest electronegative element in the Periodic Table after fluorine and oxygen is therefore very stable as an anion with a large electrochemical stability window. Although there

are still many problems need to be solved for practical applications, there have been many studies on various chloride ion conductors.

1.1.1.1 Simple metal chlorides

Inorganic metal chlorides, typically simple binary and ternary chlorides have been continuously investigated over the last century. $PbCl_2$ was the first investigated chloride-ion conductor, and the Cl^- ion conduction is attributed to anion vacancy.[30] After that, other metal chlorides were investigated, such as $Cs(Pb/Sn)Cl_3$, $(Ca/Sr/Ba/Mg)Cl_2$, and $LaCl_3$.[27,31–33] By cation substitution, these compounds achieve high ionic conductivity even near room temperature, for example, 2.3×10^{-4} S cm^{-1} at 160 °C for $Pb_{0.98}K_{0.02}Cl_{1.98}$ and $1.3–3.45 \times 10^{-4}$ S cm^{-1} at 25 °C for $CsSn_{0.9}Bi_{0.1}Cl_{3.1}$, $CsSn_{0.9}In_{0.067}Cl_3$ and $CsSn_{0.95}Mn_{0.05}Cl_3$.[25,34–36] These chlorides have also been reported to exhibit promising electrochemical properties for all solid-state chloride-ion batteries. However, the major drawback of these chlorides, as well as other metal chlorides, is their low thermal and chemical stability, including high water solubility and low melting points, for example, the melting points of $PbCl_2$ and $CsSnCl_3$ are 501 °C and 368°C respectively.[37,38] Moreover, phase transitions may also lead to a decrease in conductivity, for perovskite-type chlorides, a cubic-to monoclinic phase transition occurs under humid conditions, resulting in a significant reduction in chloride ion conductivity. These drawbacks make it difficult to use metal chlorides in practical applications.

1.1.1.2 Chlorides based on metal-organic frameworks (MOFs)

MOFs are a class of porous polymers consisting of metal clusters (also known as secondary structural units) coordinated with organic ligands to form one-, two- or three-dimensional structures. Due to its structural versatility, MOFs are often used in the field of gas adsorption/storage, molecular separations, catalysts, memory, electronic and optoelectronic devices.[39–43] Compared with inorganic crystals which diffuse ions through vacancies or

interstitial sites, MOFs conduct ions by continuous coordination between mobile ions and polar groups.[44,45] Compared to inorganic metal chlorides, chlorides based on MOFs often exhibit better chemical stability and high conductivity, for example, the polymer electrolyte composed of polyethylene oxide (PEO), succinonitrile (SN) and tributylmethylammonium chloride (TBMACl) shows conductivities ranging from 10^{-5}–10^{-4} S cm^{-1} in the temperature range of 25–70°C.[46] The membranes composed of polyvinylidene fluoride hexafluoropolymer-tetrabutylammonium chloride and tetraethyl ammonium chloride-gelatin shows conductivities of 10^{-4} S cm^{-1} at 25°C.[47] And the $[Al(DMSO)_6]Cl_3$ shows conductivities of 2.17×10^{-5} S cm^{-1} at 25°C, by partial replacement of Cl^- with PF_6^- ,the room-temperature ionic conductivity increased to 2.01×10^{-4} S cm^{-1}.[28] However, although chlorides based on MOFs exhibit good conductivity near room temperature, their high-temperature stability is poor. The operating temperatures of the aforementioned materials are below 150°C, which makes them applicable only to room-temperature environments, such as all-solid-state chloride ion batteries, and it cannot be extended to other high-temperature applications.

1.1.1.3 Oxychlorides

Mixed-anion compounds contain more than one kind of anionic species, affording interesting functional properties.[48,49] The coexistence of multiple anions in a structure can form unusual coordination geometries and structures that cannot be stabilized for the corresponding mono-anionic compounds. For oxychlorides, the instability of metal chloride compounds can be expected to be improved by strong covalent interactions between oxide ions and the metal centers. Therefore, metal oxychloride solids would provide a new good playground for developing chloride-ion conductors. In fact, a layered mixed-anion compound LaOCl with a tetragonal matlockite-type structure possesses great structural stability against humidity and high temperature, by partial replacement of La^{3+} with Ca^{2+}, $La_{0.8}Ca_{0.2}OCl_{0.8}$ prepared via ball milling exhibited the highest chloride-ion conductivity as 7×10^{-4} and 1×10^{-2} S cm^{-1} at 400

and 700 °C, respectively, which are comparable to those of $PbCl_2$ and $CsPbCl_3$.[26] Although the lowest operating temperature is higher than those of doped $PbCl_2$ and $CsSnCl_3$, anion lattice engineering using both oxide and chloride ions is an attractive approach for the design of new chloride-ion solid electrolytes with high structural stability and high ionic conductivity even at moderate temperatures. Since the O^{2-} ion possesses a smaller ionic radius than that of the Cl^- ion, however, making Cl^- transport dominant in mixed-anion sublattices remains a major challenge.[50,51] Indeed, even layered oxychlorides such as $Ba_3M_2O_5Cl_2$ (M = Y, Sc), Sr_2ScO_3Cl, $Bi_{4-x}Sr_xNbO_{8-d}Cl$, and $MBi_{2-x}Te_xO_{4+x/2}Cl$ (M = La, Lu), which adopt two-dimensional (2D) chloride layers similar to those in LaOCl, favor oxide-ion conduction.[52–55] This difference can be attributed to the different migration energies of O^{2-} ions and Cl^- ions in these oxychlorine compounds. Figure 1.1 shows the crystal structure and ionic migration energy of LaOCl.

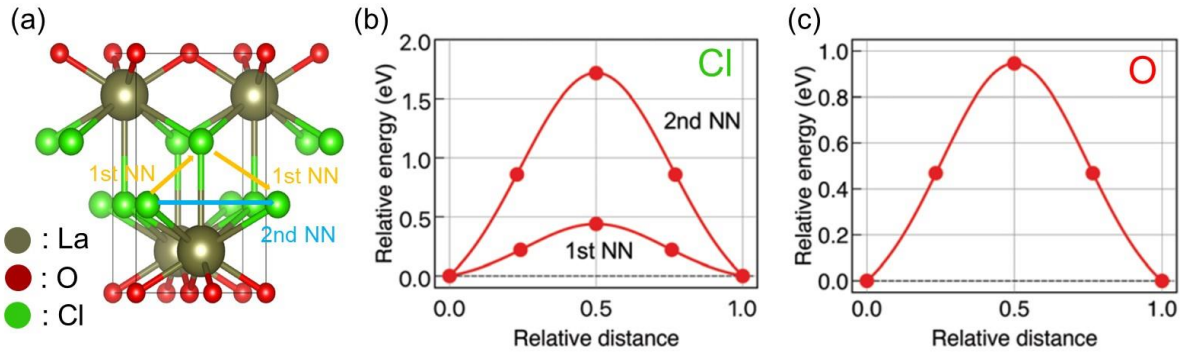

Figure 1.1 (a) Crystal structure and (b)(c) relative energies during migration of Cl^- and O^{2-} ions in LaOCl.[51]

In LaOCl, Cl^- ions have two pathways called first nearest neighbor (1st NN) and second nearest neighbor (2nd NN). By calculating the migration energies of these two pathways and those of the O^{2-} ion migration, it can be found that the energy of the 1st NN pathway of Cl^- ions is the lowest. In contrast, in $Ba_3Y_2O_5Cl_2$, O^{2-} ions have two pathways and the O1–O1 path shows the lowest migration energy. the crystal structure and ionic migration energy are shown

in Figure1.2. Therefore, it is very important to rationally design the structures of oxychlorides to make them have lower chloride-ion migration energy.

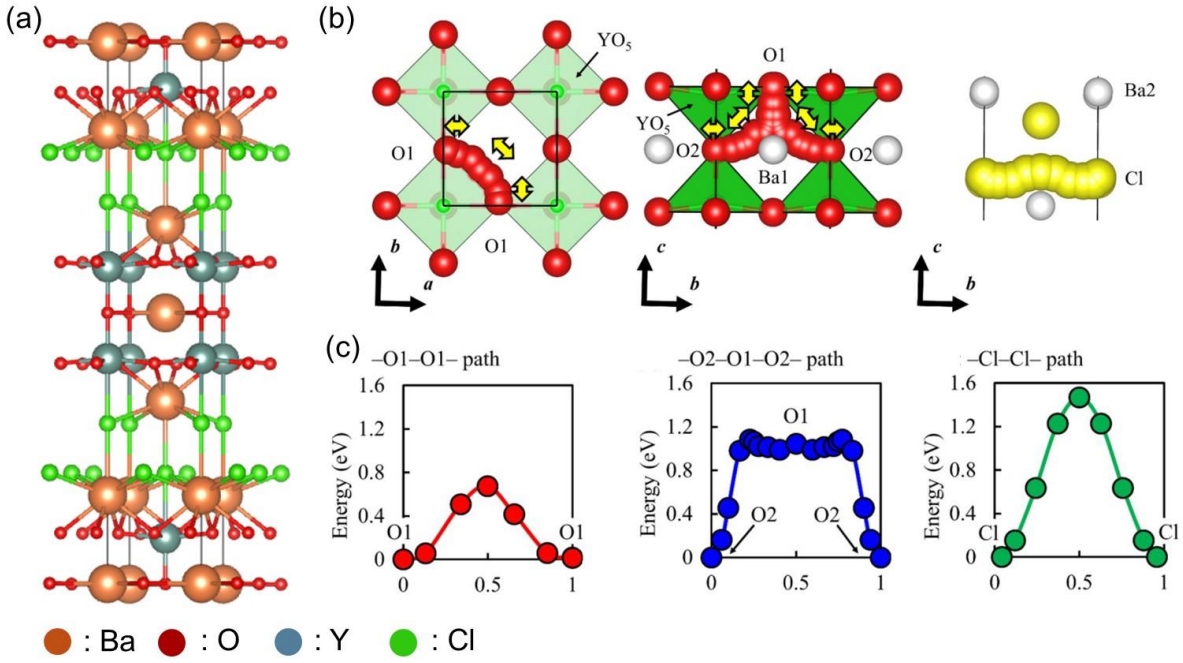

Figure 1.2 (a) Crystal structure, (b) ionic pathway and (c) relative energies during migration of Cl^- and O^{2-} ions in $Ba_3Y_2O_5Cl_2$.[52]

1.1.2 Ionic conductivity and activation energy

By applying a voltage to an SSE, an electric current is generated as the ions diffuse, according to Ohm's law, the resistance R (Ω) can be deduced from the following equation,

$$E = IR \tag{1.1}$$

Here, the resistance R (Ω) is expressed by the specific impedance ρ (Ω · cm), the cross-sectional area S (cm^2) and the distance between the electrodes l (cm), which can be written as:

$$R = \rho \frac{l}{S} \tag{1.2}$$

The reciprocal of the specific impedance is then the ease of diffusion of the ions and is defined as the ionic conductivity σ (S cm^{-1}):

$$\sigma = \frac{1}{\rho} = \frac{l}{S} \cdot \frac{1}{R} \tag{1.3}$$

The unit S is called Siemens. In the actual conductivity measurement, the measurement methods, sample shape and environmental conditions can all affect the results.

1.1.2.1 The measurement method of conductivity

The conductivity is usually measured by applying electrodes at both ends of the SSE, Figure 1.3 illustrates the image, which includes four types of resistance: those from the wire, the interface between electrode and SSE (R_i), as well as the grain boundary (R_{gb}) and the bulk (R_b) from SSE itself.

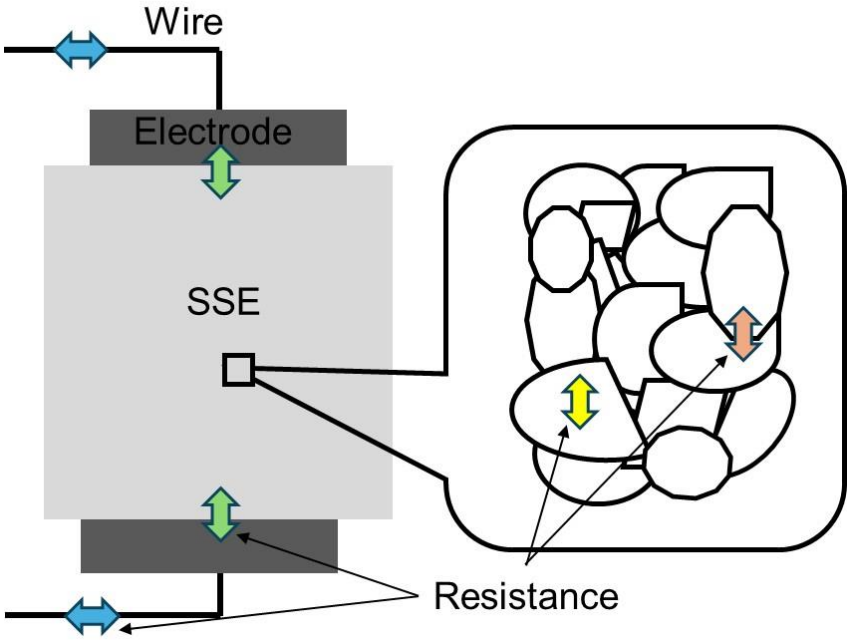

Figure 1.3 Conductivity measurement diagram. The model contains four types of resistance: those from the wire (bule), interface between electrode and SSE (green), grain boundary (orange) and bulk (yellow).

For direct current (DC) measurement, the influence from the wire can be ignored. To eliminate the influence of R_i, the four-terminal measurement method is often used which divides the electrode into current terminal and voltage terminal.[56] Therefore, the measured resistance R_{dc} can be written as:

$$R_{\mathrm{dc}} = R_{\mathrm{gb}} + R_{\mathrm{b}} \tag{1.4}$$

from this equation, it can be seen that the DC measurement cannot distinguish between R_{gb} and R_{b}, moreover, since SSE can only conduct specific ions, it is necessary to continuously inject conducting ions throughout the entire measurement period. Therefore, in actual research, it is usually analyzed together with alternating current (AC) measurement.[57]

AC impedance method is usually used for AC measurement, it applies an AC voltage with a frequency of ω and an amplitude of V_m to the SSE, then the voltage is $V = V_m e^{j\omega t}$ and the current is $I = I_m e^{j(\omega t - \Phi)}$, where Φ is the Phase Difference, j is Imaginary Numbers. According to Ohm's law, the impedance Z can be calculated by:

$$Z = \frac{V}{I} = \frac{V_m}{I_m} e^{j\Phi} = |Z| e^{j\Phi} \tag{1.5}$$

Here the $|Z|$ is the absolute value of impedance. Since $e^{j\Phi} = \cos\Phi + j\sin\Phi$, the impedance Z can be written as:

$$Z = Z' + jZ'', |Z| = \sqrt{Z'^2 + Z''^2} \tag{1.6}$$

In AC circuits, not only should the resistance of each component be considered, but also the constant phase elements (CPE) of the corresponding parts, therefore, the equivalent circuit model of the AC circuit can be simplified as shown in Figure 1.4.

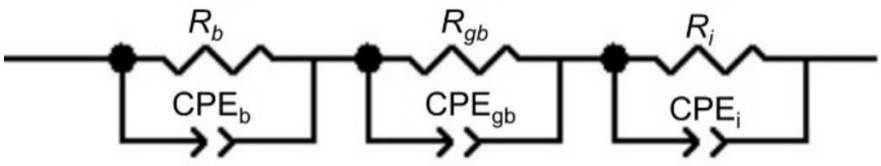

Figure 1.4 Equivalent circuit model of the AC circuit.

In this model, the resistance R and its constant phase element (CPE) form a series circuit. For each part, the impedance from resistance is $Z_R = R$, and the impedance from constant phase element is $Z_C = 1/(j\omega C)$, therefore the total impedance Z can be calculated as:

$$\frac{1}{Z} = \frac{1}{R} + j\omega C \tag{1.7}$$

By transforming this formula, impedance Z can be written as:

$$Z = \frac{R}{1 + \omega^2 C^2 R^2} - j\left(\frac{\omega C R^2}{1 + \omega^2 C^2 R^2}\right) \tag{1.8}$$

Here, combined with Equation (1.6), the real part Z' and the imaginary part Z" can be obtained as:

$$Z' = \frac{R}{1 + \omega^2 C^2 R^2} \qquad Z'' = -\left(\frac{\omega C R^2}{1 + \omega^2 C^2 R^2}\right) \tag{1.9}$$

By removing ω, the relationship between Z' and Z'' can be written as:

$$\left(Z' - \frac{R}{2}\right)^2 + Z''^2 = \left(\frac{R}{2}\right)^2 \tag{1.10}$$

Now, by plotting the graph with Z' on the horizontal axis and Z'' on the vertical axis (Nyquist plots), a semicircle can be formed with the center at (R/2, 0) and a radius of R/2. The diameter of the semicircle is the resistance R of this part.

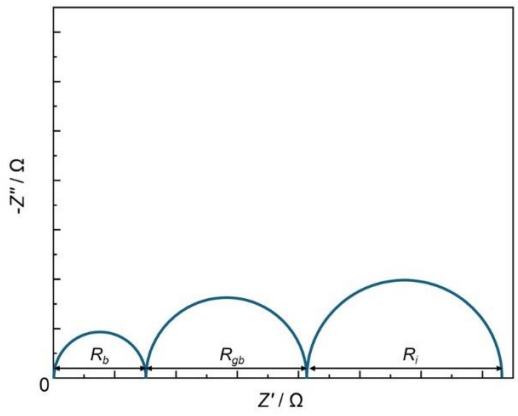

Figure 1.5 Ideal Nyquist plot. The diameters of the three semicircles represent the resistances R_b, R_{gb}, and R_i, respectively.

Therefore, an ideal model should contain 3 semicircles from R_b, R_{gb}, and R_i, respectively, as shown in Figure 1.5. Of course, in practical applications, due to interference from components, the position of the semicircle may be shifted. Moreover, sometimes, bulk

resistance and grain boundary resistance are difficult to distinguish, in such cases, the two semicircles representing them may merge, resulting in only a partial arc being identifiable.

1.1.2.2 Activation energy

Unlike in liquids, where ions can migrate freely, in solid materials, barriers exist between atoms, which often restricts ion diffusion. Since solids are not mobile, the migration of ions requires sufficient energy to overcome these barriers and migrate to other sites. The energy required for ions during this process is referred to as activation energy (E_a). The activation energy is calculated using the following Arrhenius equation:[58]

$$k = Ae^{-\frac{E_a}{RT}} \tag{1.11}$$

Where k is the rate constant of the reaction, A is pre-exponential factor, The reaction rate depends on the temperature T and the conductivity σ, therefore, this equation can be written as follows:[59]

$$\sigma T = Ae^{-\frac{E_a}{RT}} \tag{1.12}$$

Take the logarithm of both sides of the formula:

$$\ln(\sigma T) = -\frac{E_a}{R}\frac{1}{T} + \ln A \tag{1.13}$$

Plot T on the horizontal axis and $\ln(\sigma T)$ on the vertical axis, the activation energy can be determined from the slope of the resulting straight line.

1.1.3 Applications of solid state electrolytes

Unlike electron conductors that can only conduct electrons, the charge in solid state electrolytes migrates with the diffusion of ions. Taking advantage of this property, solid state electrolytes are widely used in secondary batteries, gas sensors, and thermoelectric convertors. Here are some practical applications introduced.

1.1.3.1 Sodium-sulfur battery

β-Alumina, an important solid state electrolyte that can conduct Na^+ ions, is used in sodium-sulfur battery systems. This type of battery uses sulfur for the positive terminal and sodium for the negative terminal, as illustrated in Figure 1.6.

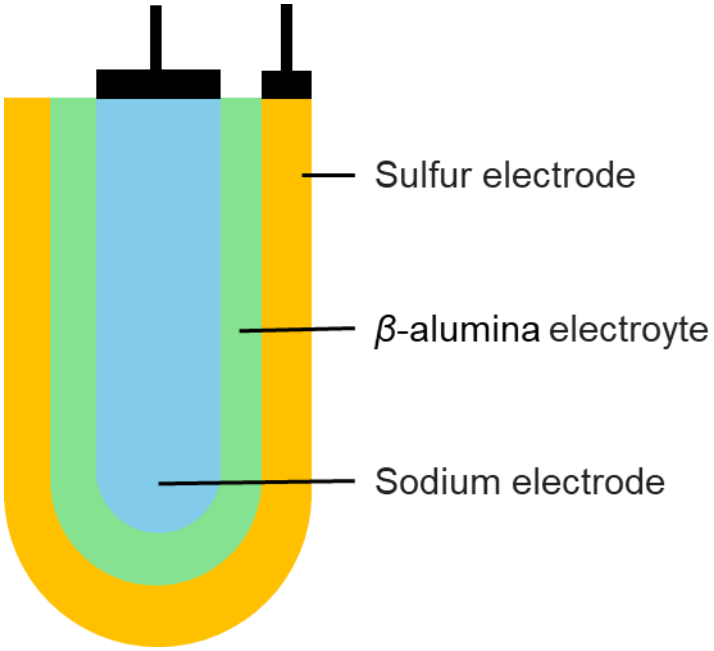

Figure 1.6 Simulated diagram of the composition of a sodium-sulfur battery. Sodium as the positive electrode, sulfur as the negative electrode, and *β*-alumina as the electrolyte.

Sodium and sulfur are heated together to a molten state at temperatures of 300–350°C, transforming them into highly reactive substances. During discharge, the sodium at the negative electrode releases electrons, forming Na^+ ions that migrate to the positive electrode through *β*-alumina. The sulfur at the positive electrode reacts with the electrons from the external circuit and the Na^+ ions migrating through the *β*-alumina to form a sodium-sulfur compound. The discharge reaction is as follows:

Cathode: $$Na \rightarrow Na^+ + e^-$$

Anode: $$Na^+ + \frac{x}{2}S + e^- \rightarrow \frac{1}{2}Na_2S_x$$

During charge, the reverse reaction occurs with the external power supply. The voltage of sodium-sulfur batteries is approximately 2 V, and the energy density is 2–3 times greater than lead-acid batteries. Currently, sodium-sulfur batteries are in practical use. However, to enhance the conductivity of β-alumina, sodium-sulfur batteries must operate in a high-temperature environment.

1.1.3.2 Zirconia oxygen sensor

As a famous example of the application of solid electrolytes in gas sensors, zirconia oxygen sensor is used to detect the oxygen concentration in automobile exhaust. The composition is shown in Figure 1.7.

The essence of the zirconia oxygen sensor is to create a gas concentration cell. The two ends of the zirconia are connected to air and exhaust gas, respectively. The difference in oxygen content causes a potential difference across both sides. O^{2-} ions are formed on the high oxygen content side (air) and migrate to the low oxygen content side (exhaust). The reaction is as follows:

$$\text{Air:} \qquad O_2 + 4e^- \rightarrow 2O^{2-}$$

$$\text{Exhaust:} \qquad 2O^{2-} \rightarrow O_2 + 4e^-$$

The voltage E between the two sides of the zirconia oxygen sensor can be expressed using the Nernst equation as follows:

$$E = \frac{RT}{nF} \ln \frac{P_{O_2(\text{air})}}{P_{O_2(\text{exhoust})}} \tag{1.14}$$

Where R is the gas constant, T is the absolute temperature, F is the Faraday constant, and n is the number of electrons in the half-reaction, which is 4 in here. In practice, the partial pressure of oxygen on the air side remains almost constant, therefore, by measuring the voltage across both sides of the sensor, the partial pressure of oxygen in the exhaust can be calculated.

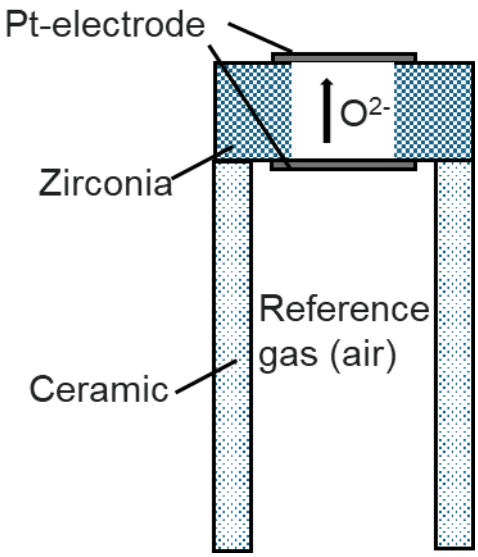

Figure 1.7 Simulated diagram of the composition of a zirconia oxygen sensor. Zirconia as an O^{2-} ions conductor, the two ends are connected to air and exhaust gas respectively.

1.1.3.3 Thermoelectric convertors

In the utilization of energy, there is always a portion of energy that is not utilized but is converted into heat and dissipated. Application of thermoelectric convertors for thermoelectric conversion can utilize this part of the energy. Thermoelectric convertors facilitate the interconversion of electrical and thermal energy through the diffusion of carriers and their interactions within the material. The composition is shown in Figure 1.8.

The converter has two types of electrolytes, P-type and N-type, which allow electrons to migrate in opposite directions. If the upper electrode is the hot end, electrons will migrate spontaneously, generating a current in the wire connected between the two lower electrodes. Conversely, if the upper electrode is the cold end, a power supply must be applied between the two lower electrodes to maintain electron migration, which is how a refrigerator operates. The advantage of the thermoelectric converter over traditional power generation methods is that it has no external rotating parts, allowing it to operate without noise or wear and tear.

Additionally, since there is no fluid medium involved, it can be said that there is essentially no environmental pollution.

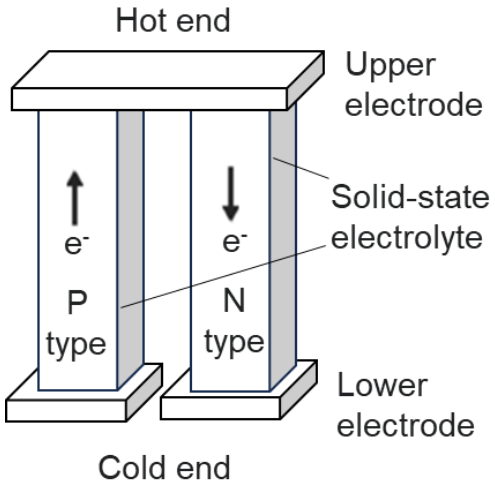

Figure 1.8 Simulated diagram of the composition of a thermoelectric convertor. The upper electrode connects the two lower electrodes through two types of electrolytes.

1.2 Open borate frameworks

Open framework inorganic materials were extensively studied during the 1990s. Most of these materials are based on oxygen-containing compounds, particularly phosphates. However, there is a growing list of examples derived from other chemistries, such as oxyfluorides, nitrides, sulfides, and borates.[60] Among them, borates have attracted significant attention due to their excellent optical and electrical properties.[61–65] Crystalline borates are well known to exhibit a rich variety of open frameworks with 0D–3D dimensionality, which are mainly composed of triangular BO_3 and/or tetrahedral BO_4 units. Due to the strong covalent interactions between B and O atoms, borate frameworks rarely produce oxygen deficiencies and therefore no oxide-ion conduction can be expected. Moreover, these units have no

inversion centers and are prone to polymerization, as illustrated in Figure 1.9. They can be combined in various configurations to attain a broad range of functions.[66–70]

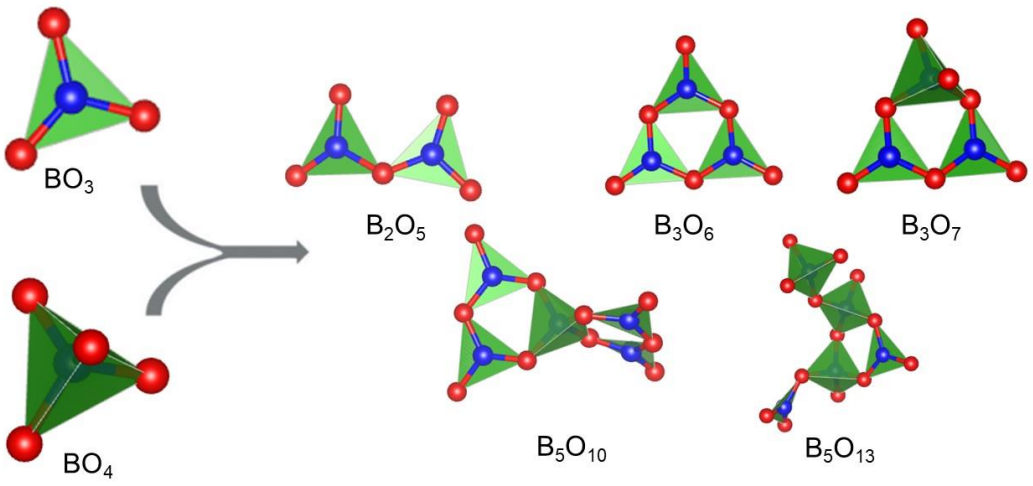

Figure 1.9 Certain structures are composed of BO_3 and/or BO_4 units.

In fact, the negatively charged borate framework typically forms open channels at the molecular scale, which serve as conducting pathways for mobile cations, including Li^+ and Na^+ ions.[71–74] For example, as shown in Figure 1.10, in the structure of $Li_6B_4O_9$, four BO_3 units are linked by vertices to form quasi-planar B_4O_9 groups, These groups are oriented perpendicular to the [100] direction, forming a kind of lamellar structure composed of B_4O_9 groups every $a/2$. Lithium atoms are coordinated only by oxygen atoms belonging to B_4O_9 groups. In the structure of $Li_3B_{11}O_{18}$, one BO_4 unit is linked to two corner-sharing BO_3 units form the B_3O_7 rings, and two crystallo-graphically distinct B_3O_7 building units, plus one that is more specific as the BO_4 tetrahedron connects two B_3O_7 rings that are perpendicular to each other to form B_5O_{10} groups. Moreover, NaB_4O_6F exhibits conductivity for Na^+ ions, as shown in the structure in Figure 1.11, there are four crystallographically independent B atoms, which adopt two types of coordination models: the BO_3 triangle and the distorted BO_3F tetrahedron, three BO_3 triangle and one BO_3F tetrahedron form B_4FO_8 groups.

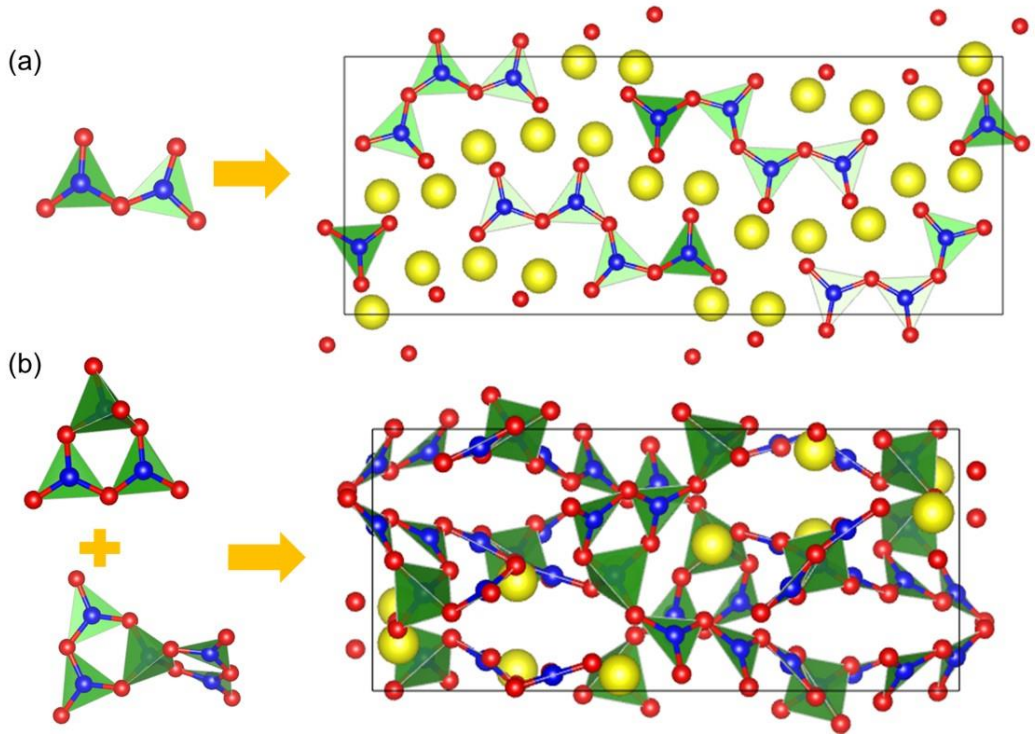

Figure 1.10 Crystal structure of (a) $Li_6B_4O_9$ and (b) $Li_3B_{11}O_{18}$. B, O and Li atoms are colored blue, red, and yellow, respectively.[72]

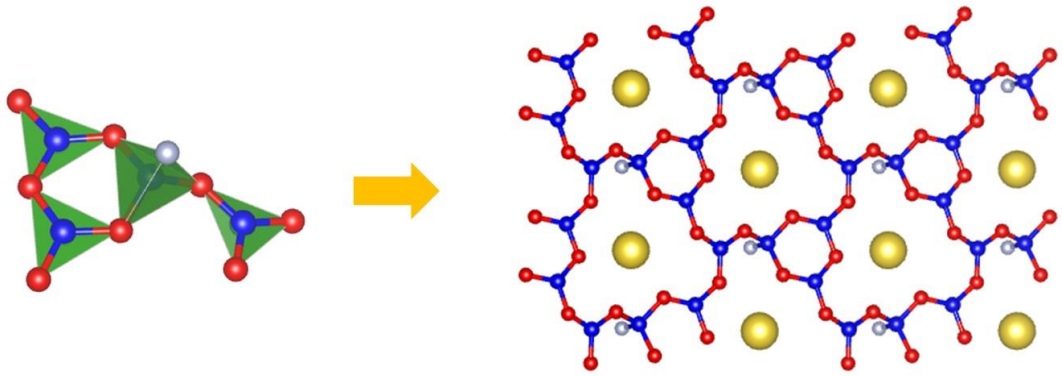

Figure 1.11 Crystal structure of NaB_4O_6F. B, O, F and Na atoms are colored blue, red, grey and yellow, respectively.[73]

However, there are no reports on the application of open borate frameworks structures for chloride-ion conduction, the purpose of this thesis is to explore the application of borate structures in chloride-ion conductors.

1.3 Solid-state reaction

Typically, reaction types can be classified based on the state of the reaction. The reaction between hydrogen and nitrogen to form ammonia occurs in the gas phase and is called a gas-state reaction, while the neutralization reaction of an acid-base mixture occurs in the liquid phase and is therefore called a liquid-state reaction. Correspondingly, the reaction occurs in the solid phase is called solid-state reaction. Compared to liquid or gas methods, solid-state reaction is an economic, efficient, and easily scalable approach.[75–78] Solid-state reactions can be roughly divided into three steps, beginning with the migration of the reactants to the phase interface, which includes processes such as evaporation-condensation or dissolution-deposition. Then the chemical reaction occurs at the phase interface, and finally the migration of the reactants is completed by diffusion. Solid-state reactions are often used in the synthesis of complex oxides. For example, MgO and Al_2O_3 can be used to synthesize $MgAl_2O_4$ with a completely different crystal structure due to atomic substitution (Figure 1.12).[79]

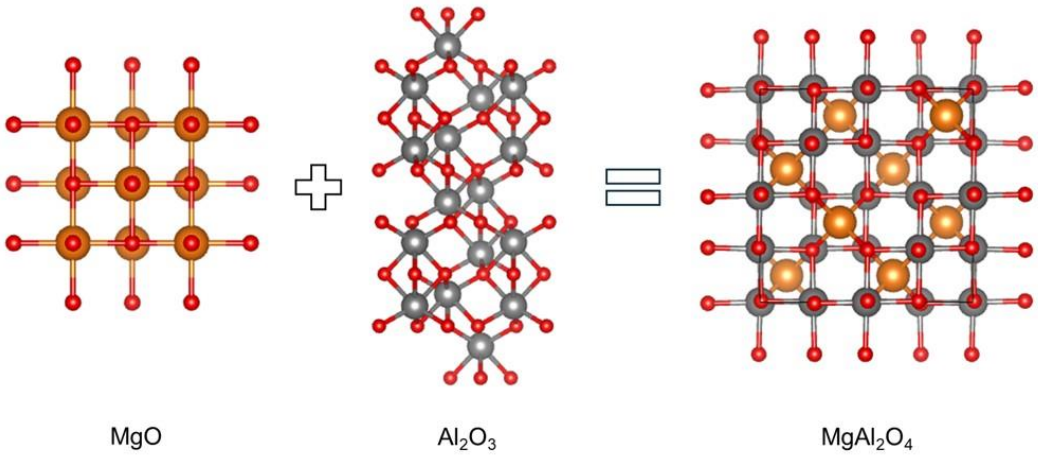

Figure 1.12 MgO and Al_2O_3 react to form $MgAl_2O_4$.

The solid-state reaction process is illustrated in Figure 1.13. The raw materials are first weighed and mixed, then the mixed powder is pressurized, and finally, the pressurized pellets

are sintered at high temperatures. Sometimes, in order to maintain the homogeneity of the composition, the product is crushed after sintering, then pressurized, and sintered a second time.

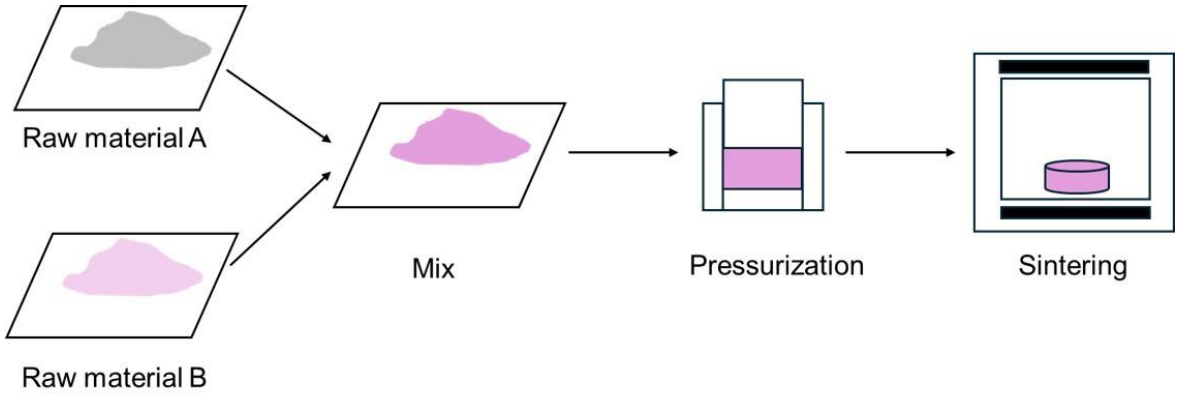

Figure 1.13 Solid-state reaction flow diagram.

1.3.1 Fick's laws of diffusion

In both gas-state and liquid-state reactions, molecules or atoms react through collisions. However, in the solid phase, molecules or atoms are not free to migrate, the reaction proceeds by the diffusion of atoms, therefore, solid-state reactions require an increase in the rate of atomic diffusion at high temperatures. Diffusion of atoms usually from high to low concentrations, the process can be described using Fick's law:

$$J = D\frac{dc}{dx} \qquad (1.15)^{80}$$

where J (mol m^{-2} s^{-1}) is the amount of substance of atoms that traverses a unit area within a unit time, D is diffusion coefficient, c is concentration, x is coordinate. According to Einstein relation (kinetic theory), the value of D depends on temperature, fluid viscosity, and molecular size, and is proportional to the square of the average velocity of the diffusing molecules. Can be described as:

$$D = \mu kT \qquad (1.15)$$

Where μ is the "mobility", k is the Boltzmann constant, T is the absolute temperature. Here we still use MgO and Al_2O_3 to form $MgAl_2O_4$ as an example (Figure 1.14).

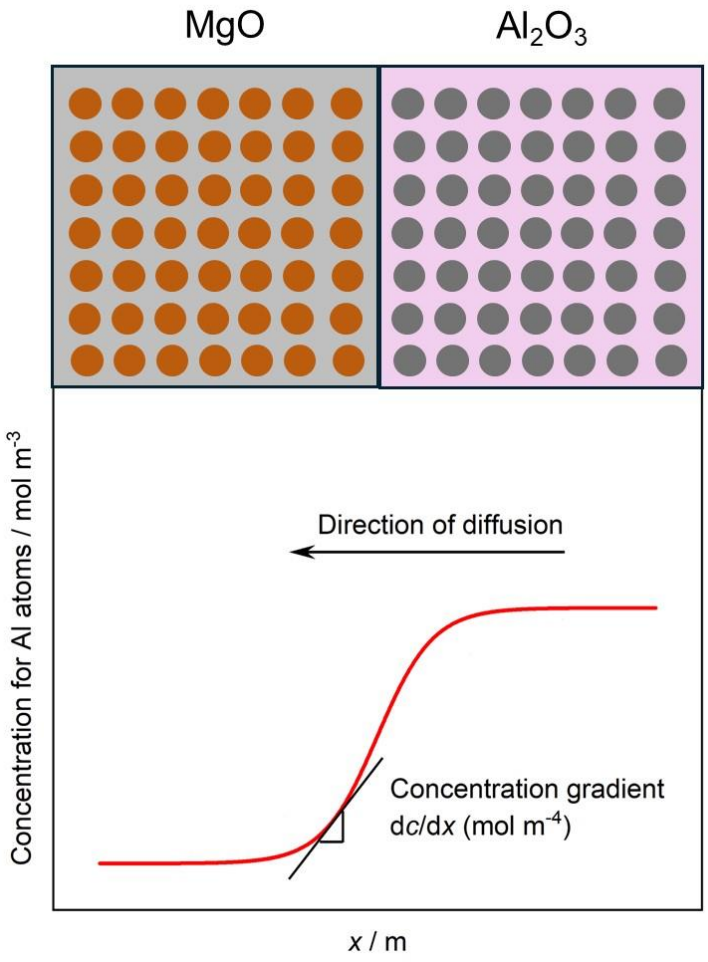

Figure 1.14 Concentration gradient and direction of diffusion.

For Al atoms before the reaction starts, their concentration and position coordinates decrease from right to left. The diffusion coefficient is positive from right to left. Therefore J is positive in the direction from right to left, meaning that Al atoms migrate from right to left. Similarly, Mg atoms migrate from left to right. Along with the diffusion, the $MgAl_2O_4$ phase begins to form until MgO and Al_2O_3 phase disappear (Figure 1.15).

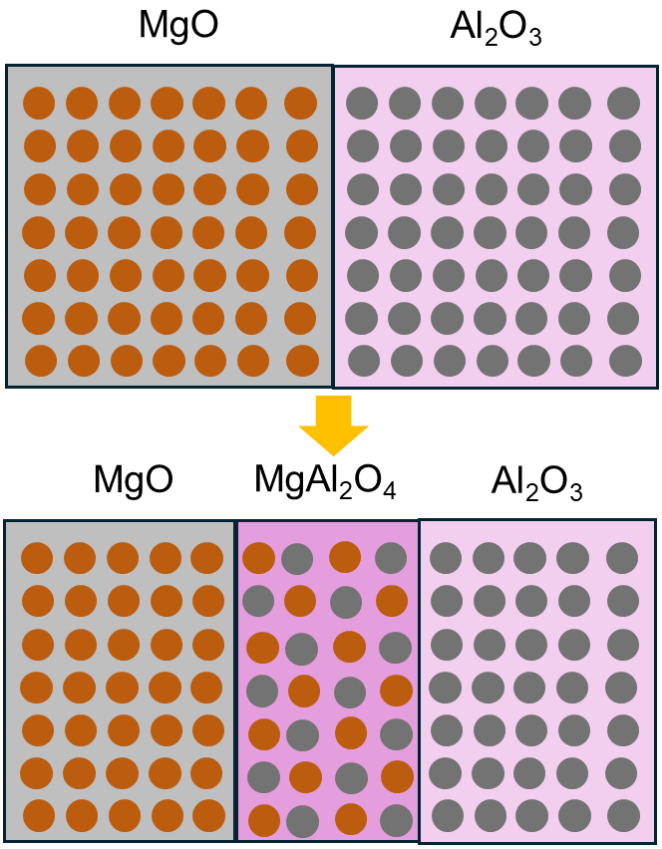

Figure 1.15 Solid-state reaction process, the $MgAl_2O_4$ phase begins to form until MgO and Al_2O_3 phase disappear.

1.3.2 Driving force for solid-state reaction

According to equation 1.15 the rate of solid-state reaction is related to the diffusion coefficient *D*, which can also be described by the Arrhenius equation:

$$D = D_0 e^{-\frac{E_a}{RT}} \tag{1.16}$$

Where D_0 is the maximal diffusion coefficient, E_a is the activation energy for diffusion, *T* is the absolute temperature, *R* is the universal gas constant. The diffusion coefficient *D* increases with absolute temperature, which is why solid-state reactions are conducted at high temperatures. In contrast, the diffusion coefficient *D* at room-temperature conditions are so small that little diffusion occurs. The driving force for solid-state reaction can be explained by

the change in surface energy. At high temperatures, the pores between the particles of the raw material shrink, reducing the specific surface area of the material, this means that the surface energy of the raw material is decreasing and thus the solid-state reaction is spontaneous.

1.4 Flux growth method

Flux growth method is a commonly used crystal growth method in which raw materials are dissolved in a flux to crystallize and precipitate the desired compound, forming crystals.[81–83] The flux usually uses inorganic compounds with lower melting points, such as $BaCl_2$, $CaCl_2$, NaCl, KI, etc. The melting point can be further reduced by the combination of inorganic compounds, which forms a lower melting eutectic. A good flux usually has the following characteristics, including:

1. Dissolving a large quantity of the regents,
2. Relatively low melting point,
3. Solubility changed with temperature,
4. Non-volatility and non-toxicity,
5. Unreaction toward the crucible,
6. Easy separation from crystals after growth,
7. Low cost

During crystal growth, when the reagent is dissolved in the solvent, the solution becomes supersaturated, and crystals begin to precipitate as the solvent evaporates and cools.

The flux growth method offers several significant advantages, compared to other methods of crystal growth, the flux growth method has such broad applicability that suitable fluxes can often be found for growing single crystals of nearly any material. The temperature of flux growth method is low, many refractory compounds and those that decompose readily

at their melting points are usually difficult to grow as complete single crystals directly from their melts, in contrast, the flux growth method can produce more uniform and complete crystals, therefore, for mixed-anion compounds, the flux growth method is an efficient method for growing single crystals. In addition, the equipment of flux growth method is simple and inexpensive.

At present, many types of mixed-anion compound single crystals have been grown using alkali chloride fluxes in a sealed fused silica tube under a relatively vacuum environment. For example, $Sr_3Ge_2O_4Se_3$ single crystals were found in the reaction productions on the SrSe, $GeSe_2$, $Sb2Se_3$, and Sb_2O_3, where Sb_2Se_3 with the lowest melting point (611°C) acts as the flux and facilitates the reaction to take place at lower temperature. $AeGeS_2O$ (Ae = Sr, Ba) single crystals were prepared by the mixtures of starting materials and KI as the molten flux.[84,85] In this thesis, we have used the flux method to obtain single crystals of several oxychlorides, details of which will be introduced in the following chapter.

1.5 Targets and objectives of this thesis

The development of chloride-ion conductors is challenging, as simple chlorides usually do not meet the conditions for practical applications, while in oxychlorides, oxygen atoms migrate more readily due to their smaller ionic radii. On the other hand, open borate frameworks allow for the design of ionic migration pathways due to their structural diversity, while the strong B-O covalent bonding can also limit the migration of oxygen atoms. As our target, we work on the application of open borate frameworks to oxychlorides to synthesize water-insoluble, high-temperature resistant chloride-ion conductors. In this thesis, all powder samples were synthesized by solid-state reaction, all single crystals were synthesized by flux growth method in a fused silica tube. Three series compounds of oxychloride based open borate frameworks were introduced.

1.5.1 $(Ca_{1-x}La_x)_2B_5O_9Cl_{1+2x}$ (x = 0–0.15)

In order to develop novel chloride-ions conductor, we aims to examine possible chloride ion conductivity for open borate framework oxychlorides. $Ca_2B_5O_9Cl$ is a hilgardite-type oxychloride,[86] which is water-insoluble and thermally stable even at 700 °C. In structure, each Cl^- ion forms a flattened tetrahedron with Ca^{2+} ions in the *ab* plane, confining the chloride ions to one-dimensional channels. To improve the conductivity, here we report the samples of $(Ca_{1-x}La_x)_2B_5O_9Cl_{1+2x}$ (x = 0–0.15) by replacing part of the Ca site by La. It exhibits the highest conductivity of 1.32×10^{-4} S cm^{-1} at 700 °C when x = 0.05. Experimental and first-principles molecular dynamics simulations indicate that the predominant chloride-ion conduction is attributed to cooperative diffusion through interstitial chloride sites. The details will be given in Chapter 3.

1.5.2 $(La_{1-x}M_x)(BO_2)_2Cl_{1-x}$ (M = Ca, Sr, x = 0–0.15)

The success of $(Ca_{1-x}La_x)_2B_5O_9Cl_{1+2x}$ (x = 0–0.15) show that the rational design of chloride-ion channels and conduction paths based on the dimensionality of the borate framework would provide a new direction for the development of the variety and conducting properties of chemically and thermally stable chloride-ion solid electrolytes. In order to explore more chloride ion conductors with open borate framework, we focus on $La(BO_2)_2Cl$ with a 2D layered structure.[87] Here we report the samples of $(La_{1-x}M_x)(BO_2)_2Cl_{1-x}$ (M = Ca, Sr, x = 0–0.15) by replacing part of the La site by Ca or Sr. It exhibits the highest conductivity of 1.84×10^{-4} S cm^{-1} at 700 °C when M = Ca, x = 0.10, and 7.59×10^{-4} S cm^{-1} at 700 °C when M = Sr, x = 0.15, respectively. The details will be given in Chapter 4.

References in chapter 1

(1) Lei, B.; Bai, S.; Ju, S.; Yin, C.; Chen, C.; Zhang, J. Review on Advances in Thermoelectric Conversion Using Ion-Conducting Polymers. *Mater. Res. Express*. **2021**, *8*(6), 062001.

(2) Yamazoe, N.; Miura, N. Gas Sensors Using Solid Electrolytes. *MRS Bulletin*. **1999**, *24*(6), 37-43.

(3) Famprikis, T.; Canepa, P.; Dawson, J. A.; Islam, M. S.; Masquelier, C. Fundamentals of Inorganic Solid-State Electrolytes for Batteries. *Nature Materials*. **2019**, *18*, 1278–1291.

(4) Nestler, T.; Schmid, R.; Münchgesang, W.; Bazhenov, V.; Schilm, J.; Leisegang, T.; Meyer, D.C. Separators - Technology Review: Ceramic based Separators for Secondary Batteries. *AIP Conf Proc*. **2014**, *1597*, 155–184.

(5) Ueda, M.; Imasawa, K.; Konda, S.; Sasaki, T.; Ishikawa, T.; Ohtsuka, T. Improvement of Chlorine Electrode in Al-Cl_2 Cell in NaCl-KCl Melt by Rotation. *Electrochemistry*. **1999**, *67*(6), 695–699.

(6) Li, W.; Wu, G.; Araújo, C. M.; Scheicher, R. H.; Blomqvist, A.; Ahuja, R.; Xiong, Z.; Feng, Y.; Chen, P. Li+ Ion Conductivity and Diffusion Mechanism in α-Li_3N and β-Li_3N. *Energy Environ. Sci*. **2010**, *3*, 1524–1530.

(7) Aono, H.; Sugimoto, E.; Sadaoka, Y.; Imanaka, N.; Adachi, G. Ionic Conductivity of Solid Electrolytes Based on Lithium Titanium Phosphate. *J. Electrochem. Soc*. **1990**, *137*(4), 1023–1027.

(8) Hong, Y.-P. Crystal Structure and Ionic Conductivity of $Li_{14}Zn(GeO_4)_4$ and Other New Li^+ Superionic Conductors. *Mat. Res. Bul*. **1978**, *13*(2), 117–124.

(9) Hayashi, A.; Noi, K.; Tanibata, N.; Nagao, M.; Tatsumisago, M. High Sodium Ion Conductivity of Glass-Ceramic Electrolytes with Cubic Na_3PS_4. *J Power Sources*. **2014**, *258*, 420–423.

(10) Kummer, J.T. *β*-Alumina Electrolytes. Ford Motor Company, Chemistry Department. **1972**, *7*, 141–175.

(11) Morimoto, S. Ionic Conductivity of Na_2O-ZrO_2-P_2O_5-SiO_2 System Glass Ceramic. *Journal of the Ceramic Society of Japan*. **1989**, *98*(10), 1097–1103.

(12) Yuan, H.; Li, H.; Zhang, T.; Li, G.; He, T.; Du, F.; Feng, S. A $K_2Fe_4O_7$ Superionic Conductor for All-Solid-State Potassium Metal Batteries. *J. Mater. Chem. A*. **2018**, *6* (18), 8413–8418.

(13) Shao, J.; Zheng, J.; Qin, L.; Zhang, S.; Ren, Y.; Wu, Y. K_3SbS_4 as a Potassium Superionic Conductor with Low Activation Energy for K–S Batteries. *Angew.Chem. Int. Ed*. **2022**, *61*, e202200606.

(14) Haile, S. M.; Lentz, G.; Kreuer, K.-D.; Maier, J. Superprotonic Conductivity in $Cs_3(HSO_4)_2(H_2PO_4)$. *Solid State Ionics*. **1995**, *77*, 128–134.

(15) Huang, M.; Huang, X.; Fei, M.; Sun, J.; Deng, Y.; Xu, C.; Cheng, J. Proton-Exchanged Graphite Oxide-Incorporated $Cs_XH_{3-X}PMo_{12}O_{40}$ with High Conductivity at Intermediate Temperatures. *Int. J. Electrochem. Sci*. **2017**, *12* (1), 240–247.

(16) Schoonman, J.; Oversluizen, G.; Wapenaar, K. E. D. Solid Electrolyte Properties of LaF_3. *Solid State Ionics*. **1980**, *1*, 211–221.

(17) Voronin, B. M.; Volkov, S. V. Ionic Conductivity of Fluorite Type Crystals CaF_2, SrF_2, BaF_2, and $SrCl_2$ at High Temperatures. *Journal of Physics and Chemistry of Solids*. **2001**, *62*, 1349–1358.

(18) Nimat, R. K.; Joshi, R. S.; Pawar, S. H. Temperature Dependent Conductivity and Dielectric Properties of $Bi_2V_{0.9}Cu_{0.1}O_{5.35}$ Solid Electrolyte Thin Films. *Materials Science and Engineering: B.* **2007**, *137* (1–3), 93–98.

(19) Cheng, J.-G.; Zha, S.-W.; Huang, J.; Liu, X.-Q.; Meng, G.-Y. Sintering Behavior and Electrical Conductivity of $Ce_{0.9}Gd_{0.1}O_{1.95}$ Powder Prepared by the Gel-Casting Process. *Materials Chemistry and Physics*. **2003**, *78*, 791–795.

(20) Yaguchi, H.; Fujii, K.; Tsuchiya, Y.; Ogino, H.; Tsujimoto, Y.; Yashima, M. Ruddlesden-Popper Oxychlorides $Ba_3Y_2O_5Cl_2$, $Sr_3Sc_2O_5Cl_2$, and Sr_2ScO_3Cl: First Examples of Oxide-Ion-Conducting Oxychlorides. *ACS Appl. Energy Mater*. **2022**, *5* (1), 295–304.

(21) Bai, Q.; He, X.; Zhu, Y.; Mo, Y. First-Principles Study of Oxyhydride H^- Ion Conductors: Toward Facile Anion Conduction in Oxide-Based Materials. *ACS Appl. Energy Mater.* **2018**, *1* (4), 1626–1634.

(22) Fukui, K.; Iimura, S.; Tada, T.; Fujitsu, S.; Sasase, M.; Tamatsukuri, H.; Honda, T.; Ikeda, K.; Otomo, T.; Hosono, H. Characteristic Fast H^- Ion Conduction in Oxygen-Substituted Lanthanum Hydride. *Nat Commun*. **2019**, *10* (1), 2578.

(23) Verbraeken, M. C.; Cheung, C.; Suard, E.; Irvine, J. T. S. High H^- Ionic Conductivity in Barium Hydride. *Nat Mater*. **2015**, *14* (1), 95–100.

(24) Kimura, N.; Niizeki, Y. Inoic Conducticity of $SnCl_2$. *Solid State Ionics*. **1981**, *3–4*, 385–388.

(25) Sakamoto, R.; Shirai, N.; Inoishi, A.; Okada, S. All-Solid-State Chloride-Ion Battery with Inorganic Solid Electrolyte. *ChemElectroChem*. **2021**, *8* (23), 4441–4444.

(26) Imanaka, N.; Okamoto, K.; Adachi, G. Y. Water-Insoluble Lanthanum Oxychloride-Based Solid Electrolytes with Ultra-High Chloride Ion Conductivity. *Angew. Chem. Int. Ed*. **2002**, *41* (20), 3890–3892.

(27) Murin, I. V.; Glumov, O. V.; Mel'Nikova, N. A. Solid Electrolytes with Predominant Chloride Conductivity. *Russian Journal of Electrochemistry*. **2009**, *45*, 411–416.

(28) Wu, B.; Luxa, J.; Šturala, J.; Wei, S.; Děkanovský, L.; Parameswaran, A. K.; Li, M.; Sofer, Z. A Room-Temperature Chloride-Conducting Metal–Organic Crystal $[Al(DMSO)_6]Cl_3$ for Potential Solid-State Chloride-Shuttle Batteries. *Energy Environ. Mater*. **2024**, *7* (1), e12530.

(29) Gschwind, F.; Euchner, H.; Rodriguez-Garcia, G. Chloride Ion Battery Review: Theoretical Calculations, State of the Art, Safety, Toxicity, and an Outlook towards Future Developments. *Eur. J. Inorg. Chem*. **2017**, *21*, 2784–2799.

(30) Hoshibo, H.; Yamazaki, M.; Nakamura, Y.; Shimoji, M. Ionic Conductivity of Lead Chloride Crystals. *J. Phys. Cos. Jpn*. **1969**, *26*(6), 1422–1426.

(31) Mizusaki, J.; Arai, K.; Fueki, K. Ionic Conduction of The Perovskite-Type Halides. *Solid State Ionics*. **1983**, *11*, 203–211.

(32) Derrington, C. E.; Lindner, A.; O'keeffe, M. Ionic Conductivity of Some Alkaline Earth Halides. Journal of Solid State Chemistry. **1975**, *15*, 171–174.

(33) Choudhuri, S. P.; Bichile, G. K. The Electrical Conductivity and Dielectric Behaviour of Polycrystalline Calcium Fluoride. *Solid State Communications*. **1987**, *64*(6), 993–995.

(34) Xia, T.; Li, Q.; Zhao, X.; Shen, X. Bismuth and Chlorine Dual-Doped Perovskite Chloride as a Phase-Structure-Stable and Moisture-Resistant Solid Electrolyte for Chloride Ion Batteries. *Adv. Mater*. **2024**, *36* (4), 2310565.

(35) Panja, S.; Miao, Y.; Döhn, J.; Choi, J.; Fleischmann, S.; Guddehalli Chandrappa, S.; Diemant, T.; Groß, A.; Karkera, G.; Fichtner, M. Synthesis, Structural Analysis, and Degradation Behavior of Potassium Tin Chloride as Chloride-Ion Batteries Conversion Electrode Material. *Adv. Funct. Mater*. **2024**, 2413489.

(36) Sakamoto, R.; Shirai, N.; Zhao, L.; Inoishi, A.; Sakaebe, H.; Okada, S. Room-Temperature Operation of All-Solid-State Chloride-Ion Battery with Perovskite-Type $CsSn_{0.95}Mn_{0.05}Cl_3$ as a Solid Electrolyte. *Electrochemistry*. **2023**, *91* (7), 077003.

(37) Verwey, J. F.; Westerink, N. G. Photoconductivity in Lead Chloride and Lead Bromide. *Physica*. **1969**, *42*, 293–302.

(38) Mizusaki, J.; Arai, K.; Fueki, K. Ionic Conduction of The Perovslite-Type Halides. *Solid State Ionics*. **1983**, *11*, 203–211.

(39) Zhang, Y.; Zheng, X.; Saito, Y.; Takeda, T.; Hoshino, N.; Takahashi, K.; Nakamura, T.; Akutagawa, T.; Noro, S. ichiro. Solution State-Like Reactivity of a Flexible Crystalline Werner-Type Metal Complex. *Angew. Chem. Int. Ed*. **2024**, e202407924.

(40) Noro, S. I.; Mizutani, J.; Hijikata, Y.; Matsuda, R.; Sato, H.; Kitagawa, S.; Sugimoto, K.; Inubushi, Y.; Kubo, K.; Nakamura, T. Porous Coordination Polymers with Ubiquitous and Biocompatible Metals and a Neutral Bridging Ligand. *Nat. Commun*. **2015**, *6*, 5851.

(41) Noro, S. ichiro; Nakamura, T. Fluorine-Functionalized Metal–Organic Frameworks and Porous Coordination Polymers. *NPG Asia Materials*. **2017**, *9*, e433.

(42) Noro, S. I.; Meng, Y.; Suzuki, K.; Sugiura, M.; Hijikata, Y.; Pirillo, J.; Zheng, X.; Takahashi, K.; Nakamura, T. A Temporarily Pore-Openable Porous Coordination Polymer for Guest Adsorption/Desorption. *Inorg Chem*. **2021**, *60* (7), 4531–4538.

(43) Zheng, X.; Kato, M.; Uemura, Y.; Matsumura, D.; Yagi, I.; Takahashi, K.; Noro, S. I.; Nakamura, T. Composite with a Glassy Nonporous Coordination Polymer Enhances Gas Adsorption Selectivity. *Inorg Chem*. **2023**, *62* (3), 1257–1263.

(44) Chen, R.; Qu, W.; Guo, X.; Li, L.; Wu, F. The Pursuit of Solid-State Electrolytes for Lithium Batteries: From Comprehensive Insight to Emerging Horizons. *Materials Horizons*. **2016**, *3*, 487–516.

(45) Forsyth, M.; Porcarelli, L.; Wang, X.; Goujon, N.; Mecerreyes, D. Innovative Electrolytes Based on Ionic Liquids and Polymers for Next-Generation Solid-State Batteries. *Acc Chem Res*. **2019**, *52* (3), 686–694.

(46) Chen, C.; Yu, T.; Yang, M.; Zhao, X.; Shen, X. An All-Solid-State Rechargeable Chloride Ion Battery. *Advanced Science*. **2019**, *6* (6), 1802130.

(47) Gschwind, F.; Steinle, D.; Sandbeck, D.; Schmidt, C.; von Hauff, E. Facile Preparation of Chloride-Conducting Membranes: First Step towards a Room-Temperature Solid-State Chloride-Ion Battery. *ChemistryOpen*. **2016**, *5* (6), 525–530.

(48) Kageyama, H.; Hayashi, K.; Maeda, K.; Attfield, J. P.; Hiroi, Z.; Rondinelli, J. M.; Poeppelmeier, K. R. Expanding Frontiers in Materials Chemistry and Physics with Multiple Anions. *Nature Communications*. **2018**, *9*, 772.

(49) Tsujimoto, Y.; Yamaura, K.; Takayama-Muromachi, E. Oxyfluoride Chemistry of Layered Perovskite Compounds. *Appl. Sci.* **2012**, *2*, 206–219.

(50) Matsumoto, H.; Miyake, T.; Iwahara, H. Chloride Ion Conduction in $PbCl_2$-PbO System. *Materials Research Bulletin*. **2001**, *36*, 1177–1184.

(51) Shitara, K.; Kuwabara, A.; Hibino, K.; Fujii, K.; Yashima, M.; Hester, J. R.; Umeda, M.; Nunotani, N.; Imanaka, N. Ionic Conduction Mechanism in Ca-Doped Lanthanum Oxychloride. *Dalton Transactions*. **2021**, *50* (1), 151–156.

(52) Yaguchi, H.; Fujii, K.; Tsuchiya, Y.; Ogino, H.; Tsujimoto, Y.; Yashima, M. Ruddlesden-Popper Oxychlorides $Ba_3Y_2O_5Cl_2$, $Sr_3Sc_2O_5Cl_2$, and Sr_2ScO_3Cl: First Examples of Oxide-Ion-Conducting Oxychlorides. *ACS Appl Energy Mater*. **2022**, *5* (1), 295–304.

(53) Kluczny, M.; Song, J. T.; Akbay, T.; Niwa, E.; Takagaki, A.; Ishihara, T. Sillén-Aurivillius Phase Bismuth Niobium Oxychloride, Bi_4NbO_8Cl, as a New Oxide-Ion Conductor. *J Mater Chem A Mater*. **2022**, *10* (5), 2550–2558.

(54) Ueno, N.; Yaguchi, H.; Fujii, K.; Yashima, M. High Conductivity and Diffusion Mechanism of Oxide Ions in Triple Fluorite-Like Layers of Oxyhalides. *J Am Chem Soc*. **2024**, *146*, 11235–11244.

(55) Yaguchi, H.; Morikawa, D.; Saito, T.; Tsuda, K.; Yashima, M. High Oxide-Ion Conductivity through the Interstitial Oxygen Site in Sillén Oxychlorides. *Adv Funct Mater*. **2023**, *33* (27), 2214082.

(56) Tanaka, Y.; Inada, M.; Enomoto, N.; Hojo, J.; Yamashita, K. Charge Fixation on Ionic Conductive Ceramics. *Journal of Smart Processing*. **2012**, *1*(4), 167–177.

(57) 平山 雅章. 無機固体電解質の電気化学特性評価. 電気化学. **2018**, 86, 53–59.

(58) Menzinger, M.; Wolfgang, R. The Meaning and Use of the Arrhenius Activation Energy. *Angew. Chem. Int. Ed*. **1969**, *8* (6), 438–444.

(59) Saito, Y.; Maruyama, T. 固体の高イオン伝導 内田老鶴圃 齋藤安俊, 丸山俊夫. **1999**.

(60) Cheetham, A. K.; Férey, G.; Loiseau, T. Open-Framework Inorganic Materials. *Angew. Chem. Int. Ed*. **1999**, *38*, 3268–3292.

(61) Mutailipu, M.; Poeppelmeier, K. R.; Pan, S. Borates: A Rich Source for Optical Materials. *Chem. Rev*. **2021**, *121*, 1130–1202.

(62) Qiu, H.; Li, F.; Li, Z.; Yang, Z.; Pan, S.; Mutailipu, M. Breaking the Inherent Interarrangement of $[B_3O_6]$ Clusters for Nonlinear Optics with Orbital Hybridization Enhancement. *J Am Chem Soc*. **2023**, *145* (44), 24401–24407.

(63) Tran, T. T.; Yu, H.; Rondinelli, J. M.; Poeppelmeier, K. R.; Halasyamani, P. S. Deep Ultraviolet Nonlinear Optical Materials. *Chem. Mater*. **2016**, *28*, 5238–5258.

(64) Kang, L.; Liang, F.; Jiang, X.; Lin, Z.; Chen, C. First-Principles Design and Simulations Promote the Development of Nonlinear Optical Crystals. *Acc Chem Res*. **2020**, *53* (1), 209–217.

(65) Nagai, T.; Kimura, T. Chemical Switching of Ferroaxial and Nonferroaxial Structures Based on Second-Order Jahn-Teller Activity in $(Na,K)_2Hf(BO_3)_2$. *Chem. Mater*. **2023**, *35* (10), 4109–4115.

(66) Wei, Q.; He, C.; Ge, B. Di; Wan, M. X.; Wei, L.; Wang, G. M. Zeolitic Open-Framework Borates with Noncentrosymmetric Structures and Nonlinear Optical Properties. *Inorg Chem*. **2019**, *58* (5), 3527–3534.

(67) Zhao, S.; Gong, P.; Luo, S.; Liu, S.; Li, L.; Asghar, M. A.; Khan, T.; Hong, M.; Lin, Z.; Luo, J. Beryllium-Free Rb3Al3B3O10F with Reinforced Interlayer Bonding as a Deep-Ultraviolet Nonlinear Optical Crystal. *J Am Chem Soc*. **2015**, *137* (6), 2207–2210.

(68) Yao, W.; Jiang, X.; Huang, H.; Xu, T.; Wang, X.; Lin, Z.; Chen, C. $Sr_8MgB_{18}O_{36}$: A New Alkaline-Earth Borate with a Novel Zero-Dimensional $(B_{18}O_{36})^{18-}$ Anion Ring. *Inorg Chem*. **2013**, *52* (15), 8291–8293.

(69) Altahan, M. A.; Beckett, M. A.; Coles, S. J.; Horton, P. N. A New Decaoxidooctaborate($^{2-}$) Anion, $[B_8O_{10}(OH)_6]^{2-}$: Synthesis and Characterization of

[$Co(En)_3$][$B_5O_6(OH)_4$][$B_8O_{10}(OH)_6$)]·5H_2O (En = 1,2-Diaminoethane). *Inorg Chem*. **2015**, *54* (2), 412–414.

(70) Daub, M.; Krummer, M.; Hoffmann, A.; Bayarjargal, L.; Hillebrecht, H. Synthesis, Crystal Structure, and Properties of Bi_3TeBO_9 or $Bi_3(TeO_6)(BO_3)$: A Non-Centrosymmetric Borate–Tellurate(VI) of Bismuth. *Chemistry - A European Journal*. **2017**, *23* (6), 1331–1337.

(71) Calès, B. :; Levasseur, A.; Fouassier, C.; Réau, J. M.; Hagenmuller, P. Conductive Ionique Du Lithium Dans Les Solutions Solides De Structure Boracite $Li_{4+x}B_7O_{12+x/2}X$(X = CI, Br)($0 \leq x \leq 1$). *Solid State Communications*. **1977**, *24*, 323–325.

(72) Rousse, G.; Baptiste, B.; Lelong, G. Crystal Structures of $Li_6B_4O_9$ and $Li_3B_{11}O_{18}$ and Application of the Dimensional Reduction Formalism to Lithium Borates. *Inorg Chem*. **2014**, *53* (12), 6034–6041.

(73) Zhang, Z.; Wang, Y.; Zhang, B.; Yang, Z.; Pan, S. Polar Fluorooxoborate, NaB_4O_6F: A Promising Material for Ionic Conduction and Nonlinear Optics. *Angewandte Chemie*. **2018**, *130* (22), 6687–6691.

(74) Duchêne, L.; Lunghammer, S.; Burankova, T.; Liao, W. C.; Embs, J. P.; Copéret, C.; Wilkening, H. M. R.; Remhof, A.; Hagemann, H.; Battaglia, C. Ionic Conduction Mechanism in the $Na_2(B_{12}H_{12})_{0.5}(B_{10}H_{10})_{0.5}$ Closo-Borate Solid-State Electrolyte: Interplay of Disorder and Ion-Ion Interactions. *Chem. Mater*. **2019**, *31* (9), 3449–3460.

(75) PETTIT, F. S.; RANDKLEV, E. H.; FELTEN, E. J. Formation of $NiAl_2O_4$ by Solid State Reaction. *Journal of the American Ceramic Society*. **1966**, *49* (4), 199–203.

(76) Cohn, G. Reactions in The Solid State. *Chemical Research Laboratory, Baker & Co., Inc. Chemical Kinetics*. **1947**, 22.

(77) Maitre, A.; Lefort´laboratoire, P. Solid State Reaction of Zirconia with Carbon. *Solid State Ionics*. **1997**, *104*, 109–122.

(78) CAHOON, H. P.; CHRISTENSEN, C. J. Sintering and Grain Growth of Alpha-Alumina. *Journal of the American Ceramic Society*. **1956**, *39* (10), 337–344.

(79) Păcurariu, C.; Lazău, I.; Ecsedi, Z.; Lazău, R.; Barvinschi, P.; Mărginean, G. New Synthesis Methods of $MgAl_2O_4$ Spinel. *J Eur Ceram Soc.* **2007**, *27* (2–3), 707–710.

(80) Zhou, L.; Nyberg, K.; Rowat, A. C. How We Teach: Classroom And Laboratory Research Projects Understanding Diffusion Theory and Fick's Law through Food and Cooking. *Adv Physiol Educ.* **2015**, *39*, 192–197.

(81) Rosa, P. F. S.; Fisk, Z. Flux Methods for Growth of Intermetallic Single Crystals.

(82) Beaurain, M.; Armand, P.; Papet, P. Growth of Piezoelectric Single Crystals by the Flux Method. *Journal of Crystal Growth*. **2005**, *275*, e279–e282.

(83) Watanabe, K. An Approach to The Growth of $YBa_2Cu_3O_{7-x}$ Single Crystals by The Flux Method. *Journal of Crystal Growth*. **1990**, *100*, 293–296.

(84) Juillerat, C. A.; Klepov, V. V.; Morrison, G.; Pace, K. A.; Zur Loye, H. C. Flux Crystal Growth: A Versatile Technique to Reveal the Crystal Chemistry of Complex Uranium Oxides. *Dalton Transactions*. **2019**, *48*, 3162–3181.

(85) Bugaris, D. E.; Zur Loye, H. C. Materials Discovery by Flux Crystal Growth: Quaternary and Higher Order Oxides. *Angew. Chem. Int. Ed*. **2012**, *51*, 3780–3811.

(86) Wang, Z.; He, J.; Hu, B.; Shan, P.; Xiong, Z.; Su, R.; He, C.; Yang, X.; Long, X. $Ca_2B_5O_9Cl$ and $Sr_2B_5O_9Cl$: Nonlinear Optical Crystals with Deep-Ultraviolet Transparency Windows. *ACS Appl Mater Interfaces*. **2020**, *12* (4), 4632–4637.

(87) Nikelski, T.; Schleid, T. $LaCl(BO_2)_2$ Und $Er_2Cl_2[B_2O_5]$: Zwei Chlorid-Oxoborate Dreiwertiger Lanthanide. *Z Anorg Allg Chem*. **2003**, *629* (11), 2028–2033.

Chapter 2. Experimental methods

As mentioned in last chapter, the diversity of open borate frameworks enables structural design, while the strong B–O covalent bond makes it difficult for O atoms to migrate. Although open borate frameworks have been used for cationic conductors, no applications have been reported for chloride ion conductors. This thesis focuses on the synthesis of oxychlorides with open borate frameworks and explores their chloride ion conductivity. In this work, all the samples were prepared in the fused silica tube under vacuum. Crystal structures, conductivity properties, and air/thermal stabilities were investigated, through single crystal X-ray diffraction (SCXRD), electrochemical impedance spectroscopy (EIS), powder X-ray diffraction (PXRD), and thermal gravimetric analysis (TG-DTA).

2.1 Sample synthesis

In this work, all other reagents were purchased commercially, except for CaO, which was obtained by heating $CaCO_3$ (Rare Metallic, 99.99%) overnight in air at 950°C, some reagents were dried at high temperatures prior to use. All raw materials were stored in an Ar-filled glovebox (moisture and oxygen levels less than 0.1 ppm).

2.1.1 Solid state synthesis

In this thesis, all the polycrystalline samples were prepared using solid state synthesis. The starting reagents were weighed in a stoichiometric ratio and ground thoroughly with an agate mortar and pestle in the glove box, because the precursors were sensitive to the moisture. Then, the mixture was pelletized by pressing at 8 kN into a pellet with a diameter of 6.9 mm, flame-sealed in silica tube under a vacuum level of 1 Pa, and then heated in a muffle furnace at 880°C or 900°C for 24h and cooled to room temperature for 6h. After the reaction was completed, the pellet was ground and pressing at 8 kN into a pellet again with a diameter of

6.9 mm to ensure more complete reaction of the raw materials. It was then sintered a second time under the same conditions. However, the samples used for conductivity measurements were pressed into pellets with a diameter of 10 mm by pressing at 100 KN before secondary sintering. The quality of the polycrystalline samples was checked by PXRD. Polycrystalline of high purity was used for the further characterization and measurement.

2.1.2 Flux growth method

In this thesis, all the crystal samples were prepared using flux crystal growth method. The starting reagents were weighed in a stoichiometric ratio and mixed in the glove box, but the mixture was sealed in silica tube under a vacuum level of 1 Pa instead of being pressed into pellets and heated in the muffle furnace at 1000°C for 24h, to promote better growth of the single crystal, the cooling rate is controlled at 5°C/h until it reaches 600°C, after which the power is turned off to allow natural cooling. Finally, the products were washed with sonicated water and extracted from the flux. Colorless single crystals were collected by vacuum filtration for the structural analysis.

2.2 X-ray diffraction

The properties of a substance depend largely on its structure, therefore, structural research is particularly important. As a highly effective method for studying material structure, X-ray diffraction measurements and their technical applications have been thoroughly studied and applied.[1] In this thesis, two main X-ray diffraction methods were applied and the details will be illustrated in the following sections.

2.2.1 Powder X-ray diffraction

Powder X-ray diffraction (PXRD) is an important technique for the preliminary characterization of the phase state of materials and plays a crucial role in structural studies. In

this work, room temperature PXRD data collection was performed using a Desktop X-ray Diffractometer MiniFlex (Rigaku) as shown in Figure 2.1, This machine equips a graphite monochromator and Cu Kα radiation (λ = 1.5418 Å). In the measurements, the increment is 0.2° and the scanning range is 5°< 2θ <60° with a scanning rate of 1°/min.

2.2.2 Single crystal X-ray diffraction

The structure of the single crystals was determined using a Rigaku XtaLab Mini II diffractometer (Mo *Kα* radiation) at the room temperature, as shown in Figure 2.2. Raw area detector data frames were reduced and corrected for absorption effects using the SAINT+ and SADABS programs. The final unit cell parameters were determined by least-squares refinement of the data set. The initial structural models were performed with the SHELX package, through the OLEX2 GUI.[2–4]

Figure 2.1 Photograph of an X-ray powder diffractometer (MiniFlex, Rigaku).

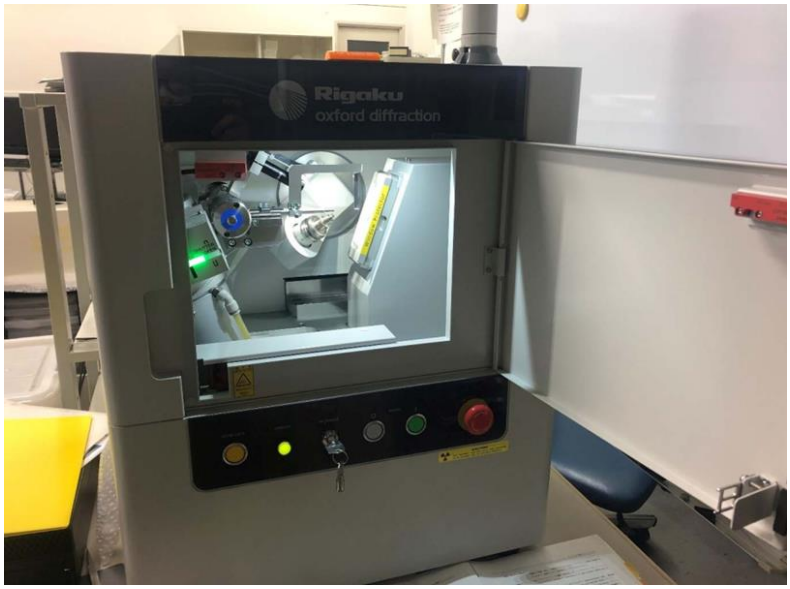

Figure 2.2 Photograph of a single crystal X-ray diffractometer (XtaLab mini II, Rigaku).

2.3 Electrochemical impedance spectroscopy (EIS) measurements.

Electrochemical impedance spectroscopy is widely used in the fields of secondary batteries, fuel cells, and corrosion protection. It is a commonly employed electrochemical technique for analyzing electrode process kinetics and diffusion. EIS measurements usually require gold spraying of the sample pellets to enhance the conductivity between the sample and the electrode. In this thesis, the measurements consist of two parts: AC measurements and DC measurements.

2.3.1 Gold Spraying

Formation of a gold sputtering layer in the center of the pellet surface using an ion coater IB-3 Eiko, as shown in Figure 2.3. The side of the sample pellets were wrapped with tinfoil while exposing only the areas to be gold-sprayed, and then placed in the chamber of the ion coater. The chamber was evacuated to 2.8 Pa and then gold was deposited on both sides of

the pellet by applying a current of 40 mA for 10 min. The tinfoil was carefully removed with tweezers.

Figure 2.3 Photograph of an ion coater (IB-3, Eiko) (Ref. https://www.1974eiko.co.jp/).

To prevent the evaporation of the deposited gold, gold powder dispersed in toluene was applied to both sides of the pellet. The photo of pellet after treatment as shown in Figure 2.4. Finally, both of the top and bottom sides of the pellet were connected with gold wire and sandwiched between sping-loaded alumina disks. A self-made temperature sensor was placed inside the cell, near the gold electrodes, to monitor the temperature. The photographs are shown in Figure 2.5.

Figure 2.4 Photographs of surface gold coating on a pellet by ion coating (left), followed by further coating with gold paste (right).

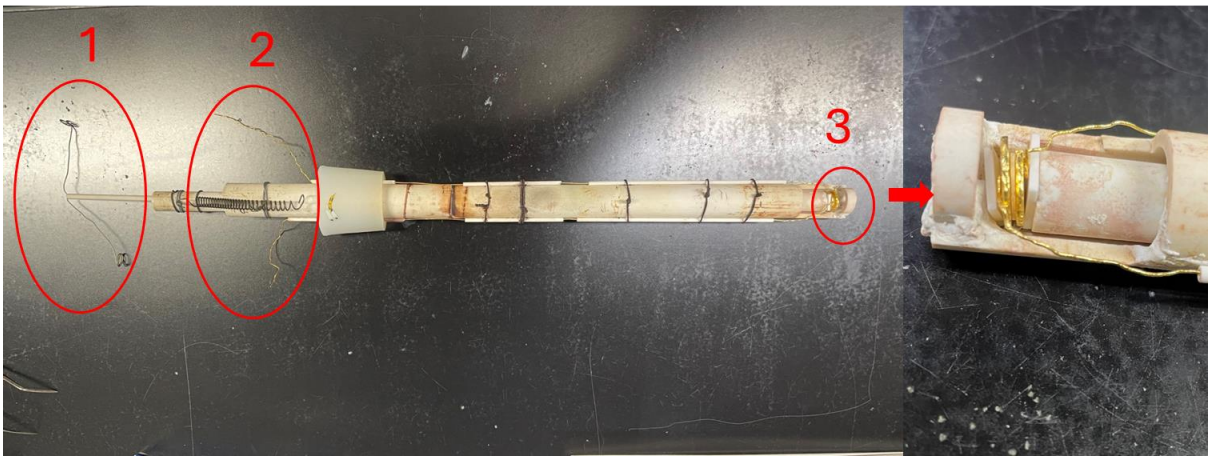

Figure 2.5 Photographs of the setup for electrical conductivity measurements. A pellet is placed between two gold electrodes (3), the cell shell is handmade by alumina. The gold electrodes are connected to the outside through gold wires to facilitate the application of current (2). A simple temperature sensor is placed near the gold electrodes to detect the cell temperature, which is also extended outside with a wire (1). After setting, use a spring to fix to prevent loosening.

2.3.2 AC measurements

AC EIS of the pellets was measured using the 1260 impedance analyzer, Solartron, as shown in Figure 2.6. The measured voltage is 300mV, frequency range between 1 Hz and 10 MHz. Starting at 400°C and testing at 100°C intervals up to 700°C in an Ar or O_2 gas atmosphere. A photograph of a furnace used for electrical conductivity measurements is shown in Figure 2.7.

Figure 2.6 Photograph of a 1260 impedance analyzer (Solartron).

Figure 2.7 Photograph of a furnace used for electrical conductivity measurements.

2.3.3 DC measurements

DC EIS of the pellets was measured using a DC voltage/current generator, R6144 Advantest, is shown in Figure 2.8. The measurement uses a constant voltage of 300mV or a constant current of 0.1μA at 700°C in an Ar gas atmosphere.

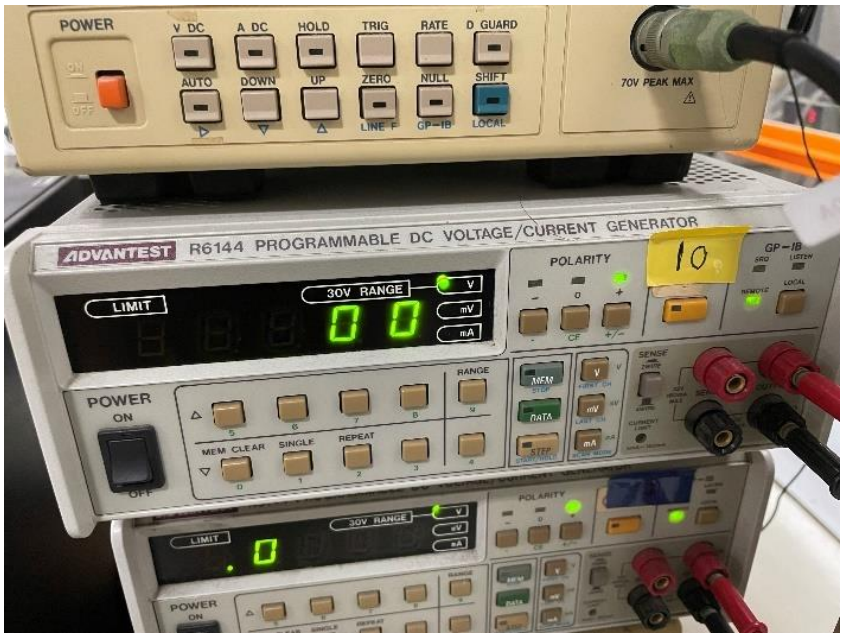

Figure 2.8 Photograph of a DC voltage/current generator (R6144 Advantest).

2.4 Elemental analysis.

Energy Dispersive X-ray (EDX) spectroscopy is a technique for elemental and compositional analysis that detects characteristic X-rays generated by electron irradiation and utilizes energy spectroscopy. In this thesis, elemental analysis was carried out using a scanning electron microscope (SEM), HITACHI-TM3000, equipped with an EDX spectrometer, Oxford Instruments, Swift ED3000, as shown in Figure 2.9. The accelerating voltage was 15 keV.

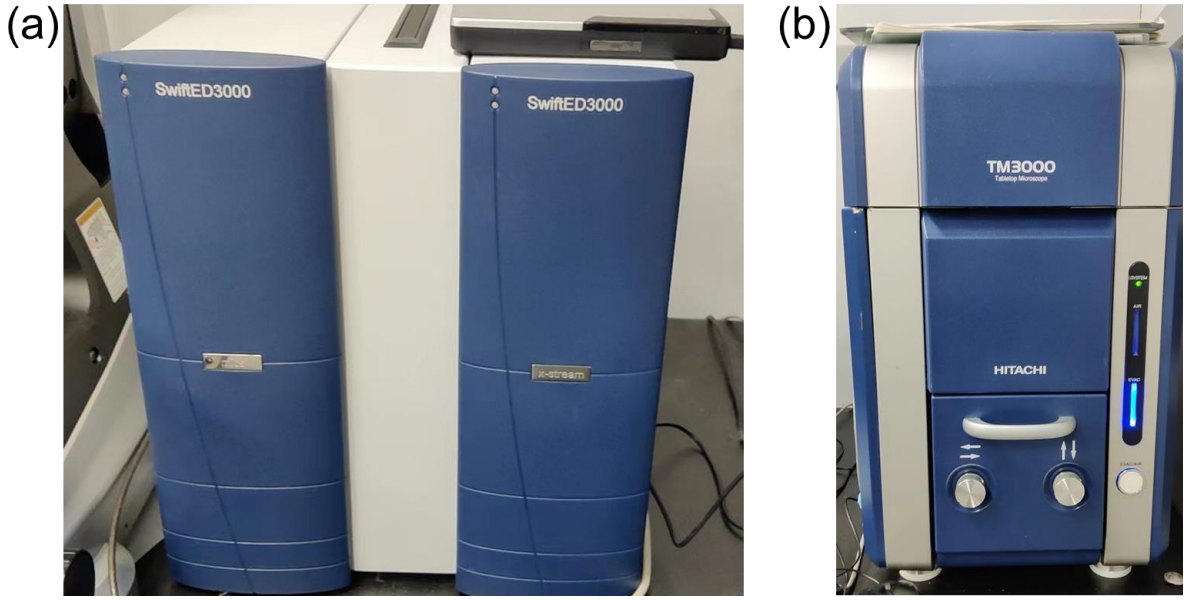

Figure 2.9 Photographs of (a) an EDX spectrometer (Oxford Instruments, Swift ED3000) and (b) a SEM (HITACHI-TM3000).

2.5 Thermal gravimetric analysis

TG-DTA observes the endothermic or exothermic behaviors when the sample undergoes phase transitions or chemical reaction. In this thesis, TG-DTA of powder samples were performed using a Rigaku TG-DTA8188 system is shown in Figure 2.10. The sample was loaded in a Pt crucible and heated up to elevated temperature at a rate of 10°C /min under N_2 or O_2 gas atmosphere. Alumina was used as the standard.

Figure 2.10 Photograph of a Rigaku TG-DTA8188 system.

2.6 Other technologies used in this work.

First-principles calculations. Density Functional Theory (DFT) is a powerful computational method used extensively in physics, chemistry, and materials science to study the electronic and nuclear structure of many-body systems, including atoms, molecules, and condensed phases.[6–8] By using functionals, which are functions of another function, DFT can determine the properties of a many-electron system based on the electron density. In this thesis, the formation energies of point defects in $Ca_2B_5O_9Cl$ were evaluated using first-principles total energy calculations. To calculate the point defects, we optimized the unit cell and positional parameters before the calculation and constructed a supercell model containing the optimized unit cells. First-principles calculations based on DFT were performed to investigate the

optimized structure, defect formation energy, and migration energy using the projector augmented-wave (PAW) method implemented in the VASP code.[9–12] The exchange correlation term was treated with GGA-PBE.[6] The plane-wave cutoff energy was set to 550 eV. Structure optimization was conducted until all residual forces acting on each atom were less than 0.01 eV/Å. First-principles molecular dynamics simulations were also performed. The simulation cells were the same as those used for the point defect. The total simulation time was 100 ps with a time step of 2 fs. The first 10 ps were removed from the analysis. The temperature was set to 2000 K to detect atomic jumps, though it is higher than the experimental conditions. The migration energies of Cl'_i ion via the interstitialcy mechanism were calculated using the nudged elastic band (NEB) method with three intermediate images.

References in Chapter 2

(1) Anthony R. West *Solid State Chemistry and Its Applications*; John Wiley & Sons, **2014**.

(2) G. M. Sheldrick. SHELXT - Integrated space-group and crystal-structure determination. *Acta Cryst*. **2015**, A71, 3-8.

(3) C. B. Hubschle, G. M. Sheldrick, B. Dittrich. ShelXle: a Qt graphical user interface for SHELXL. *J. Appl. Crystallogr*. **2011**, 44, 1281–1284.

(4) O. V. Dolomanov, A. J. Blake, N. R. Champness, M. Schröder. OLEX: new software for visualization and analysis of extended crystal structures. *J. Appl. Crystallogr*. **2003**, 36, 1283–1284.

(5) N. Imanaka, M. R. I. B. Misran, N. Nunotani. Evidence for enormous iodide anion migration in lanthanum oxyiodide–based solid. *Science Advances*. **2021**, 43, 812–816.

(6) J. P. Perdew, A. Ruzsinszky, G. I. Csonka, O. A. Vydrov, G. E. Scuseria, L. A. Constantin, X. Zhou and K. Burke, *Phys Rev Lett*, **2008**, 100, 136406.

(7) G. Henkelman and H. Jónsson, *J Chem Phys*, **2000**, 113, 9978–9985.

(8) G. Henkelman, B. P. Uberuaga and H. Jónsson, *J Chem Phys*, **2000**, 113, 9901–9904.

(9) G. Kresse and D. Joubert, *Phys Rev B*, **1999**, 59, 1758–1775.

(10) G. Kresse and J. Furthmüller, *Phys Rev B*, **1996**, 54, 11169–11186.

(11) G. Kresse and J. Furthmüller, *Comput Mater Sci*, **1996**, 6, 15–50.

(12) G. Kresse and J. Hafner, *Phys Rev B Condens Matter*, **1993**, 47, 558–561.

Chapter 3 $(Ca_{1-x}La_x)_2B_5O_9Cl_{1+2x}$ (x = 0–0.15): Rational design of chloride ion transport channels in an open borate framework

3.1. Introduction

Currently, SSEs are widely used in all-solid-state batteries, gas sensors, separators, thermoelectric convertors and other applications due to their excellent safety, chemical and mechanical stability.[1–6] However, most of the application are conduction of small radius ions, as exemplified by yttria-stabilized zirconia for solid oxide fuel cells,[7] Na-β alumina for sodium-sulfur batteries,[8] and Li_6PO_5Cl for Li-ion batteries,[9] the variety of chloride-ion conducting SSEs is poor.[10–12] Although inorganic metal chlorides, typically simple binary and ternary chlorides, have been continuously investigated over the last century, compounds such as $PbCl_2$ (cotunnite-type structure), $Cs(Sn/Pb)Cl_3$ (perovskite-type structure) and others achieve high ionic conductivities via cation substitution even near room temperature.[13–21] the major drawback of these metal chlorides, is their low thermal and chemical stability, including low melting points and high water solubility.[22–24] For perovskite-type chlorides, a cubic to monoclinic phase transition occurs under humid conditions, resulting in a significant reduction in chloride ion conductivity. In contrast, a layered mixed-anion compound $La_{1-x}Ca_xOCl_{1-x}$ ($0 \leq x \leq 0.2$) with a tetragonal matlockite-type structure possesses great structural stability against humidity and high temperature.[25] Moreover, $La_{0.8}Ca_{0.2}OCl_{0.8}$ (x = 0.2) prepared via ball milling exhibited chloride-ion conductivity as high as 7×10^{-4} and 1×10^{-2} S cm^{-1} at 400 and 700 °C, respectively, which are comparable to those of $PbCl_2$ and $CsPbCl_3$. Although the lowest operating temperature is higher than those of doped $PbCl_2$ and $CsSnCl_3$, anion lattice engineering using both oxide and chloride ions is an attractive approach for the design of new chloride-ion solid electrolytes with high structural stability and high ionic conductivity even at moderate temperatures. On the other hand, making Cl^- transport dominant in mixed-anion

sublattices, where the migration barrier for Cl^- ions tends to be higher than that for O^{2-} ions, remains a major challenge.[26,27] Indeed, even layered oxychlorides such as $Ba_3M_2O_5Cl_2$ (M = Y, Sc),[28] Sr_2ScO_3Cl,[28] $Bi_{4-x}Sr_xNbO_{8-d}Cl$,[29] and $MBi_{2-x}Te_xO_{4+x/2}Cl$ (M = La, Lu),[30,31] which adopt two-dimensional (2D) chloride layers similar to those in LaOCl, favor oxide-ion conduction.

Crystalline borates are well known to exhibit a rich variety of open frameworks with 0D–3D dimensionality, which are mainly composed of triangular BO_3 and/or tetrahedral BO_4 units.[32] The negatively charged borate framework typically forms open channels at the molecular scale, which serve as conducting pathways for mobile cations, including Li^+ and Na^+.[33–36] Importantly, borate frameworks rarely produce oxygen deficiencies due to the strong covalent interactions between B and O atoms,[37] and therefore no oxide-ion conduction can be expected. To examine possible chloride ion conduction in open framework borates, we chose a hilgardite-type oxychloride, $Ca_2B_5O_9Cl$,[38] which is water-insoluble and thermally stable even at 700 °C. This borate chloride has been studied for applications of deep UV non-linear optics and photoluminescence,[39–40] but not as an ionic conductor. Each Cl^- ion forms a flattened tetrahedron with Ca^{2+} ions in the *ab* plane, confining the chloride ions to one-dimensional channels. In this chapter, we report that La-doped $Ca_2B_5O_9Cl$ exhibits one-dimensional chloride-ion conduction within the $(B_5O_9)^{3-}$ borate framework, which reaches 1.32×10^{-4} S cm^{-1} at 700 °C with 5% La doping. Single-crystal structure analysis revealed an increased concentration of Cl^- ions by La^{3+} doping in chloride-ion transport channels, involving significant chlorine deficiencies at the original site and site disorder along the channel directions. First-principles molecular dynamics simulation indicated one-dimensional diffusion of chloride ions through the interstitialcy mechanism influenced by the association between La and Cl defects. The open borate framework would provide a useful tool for rational

design of chloride-ion channels and conduction paths, further developing chloride-ion conductors.

3.2 Experimental details of Chapter 3

Reagents. B_2O_3 (Sigma-Aldrich, 99.98%), $CaCl_2$ (Wako Pure Chemical Industries, 95.0%) powders were used as received. La_2O_3 (Rare Metallic, 99.99%) was heated overnight in a dry oven at 1000°C prior use. CaO was obtained by heating $CaCO_3$ (Rare Metallic, 99.99%) overnight in air at 950°C. All raw materials were stored in an Ar-filled glovebox (moisture and oxygen levels less than 0.1 ppm)

Crystal Growth. Single crystals of $Ca_2B_5O_9Cl$ and $(Ca_{0.92}La_{0.08})_2B_5O_9Cl_{1.16}$ were obtained by the flux growth method using a $CaCl_2$ molten salt. 4.5 mmol of B_2O_3, 2.7 mmol of CaO, and 1g of $CaCl_2$ for the undoped sample and 4.5 mmol of B_2O_3, 2.16 mmol of CaO, 0.18 mmol of La_2O_3, and 1g $CaCl_2$ for the La-doped sample were thoroughly mixed, loaded into a silica tube with a diameter of 11 mm, and flame-sealed under a vacuum level of 1 Pa. The starting materials were heated in a muffle furnace to 1000°C within 6h and held for 24h, cooled to 600°C at 5°C/h, and finally naturally cooled to room temperature by turning off the heater. The products were then washed with sonicated water and extracted from the flux. Colorless transparent rod-shaped crystals of $Ca_2B_5O_9Cl$ and $(Ca_{0.92}La_{0.08})_2B_5O_9Cl_{1.16}$ were collected by vacuum filtration, respectively.

Solid State Reaction. Polycrystalline powder samples of $(Ca_{1-x}La_x)_2B_5O_9Cl_{1+2x}$ (x = 0, 0.05, 0.10, 0.125, 0.15) were synthesized from a stoichiometric mixture of B_2O_3, CaO, $CaCl_2$, and La_2O_3. The mixture was ground thoroughly with an agate mortar and pestle, pelletized by pressing at 8 kN into a pellet with a diameter of 6.9 mm, flame-sealed under a vacuum level of 1 Pa, and then heated in a muffle furnace at 880°C for 24h and cooled to room temperature for 6h. After the reaction was completed, the pellet was ground and pressing at 8 kN into a pellet

again with a diameter of 6.9 mm to ensure more complete reaction of the raw materials. It was then sintered a second time under the same conditions.

Elemental Analysis. Elemental analysis on the single crystals of undoped and La-doped Ca2B5O9Cl was carried out using a scanning electron microscope (SEM, HITACHI-TM3000) equipped with an energy dispersive X-ray (EDX) spectrometer (Oxford Instruments, Swift ED3000). The accelerating voltage was 15 keV.

Single-Crystal Structure Determination. Single crystal X-ray diffraction (SCXRD) data of undoped and La-doped $Ca_2B_5O_9Cl$ that were obtained by flux method were collected at room temperature using a Rigaku XtaLab mini II diffractometer (Mo *Ka* radiation). The data collection covered 99% of the reciprocal space to $2\theta_{max}$ = 61.0° with R_{int} = 5.64% (undoped phase) and 3.01% (La-doped phase) after absorption correction. The crystal structures were solved by a dual-space algorithm method (SHELXT)[41] and refined by a full-matrix least-squares method with SHELXL,[42] using an Olex2 graphical user interface.[43]

Laboratory X-ray Powder Diffraction. Powder X-ray diffraction (PXRD) measurements of $(Ca_{1-x}La_x)_2B_5O_9Cl_{1+2x}$ (x = 0, 0.05, 0.10, 0.125, 0.15) powder samples were performed using a Rigaku MiniFlex600 diffractometer (Cu *Ka* radiation) in the 2θ range from 5° to 60° at room temperature.

Thermal Gravimetric Analysis. Thermogravimetric analysis (TGA) of x = 0.10 powder samples were performed using a Rigaku TG-DTA8188 system under flowing N_2 atmosphere (1.0 L/min). The sample was loaded in an alumina crucible and heated up to 700°C at 10°C/min.

EIS Measurements. $(Ca_{1-x}La_x)_2B_5O_9Cl_{1+2x}$ (x = 0, 0.05, 0.10, 0.125, 0.15) powder samples were pelletized by pressing at 100 kN with diameter and thickness of 10 mm and 1 mm, respectively, followed by a second sintering with the same heating conditions. These obtained pellets were polished with waterproof abrasive papers until they were less than 0.6

mm thick. Formation of a gold sputtering layer in the center of the pellet surface using an ion coater (IB-3, Eiko), and then a gold paste was fixed on the sputtered layer. AC EIS of the pellets was measured using the complex impedance method (1260 impedance analyzer, Solartron) at 300 mV in the frequency range between 1 Hz and 10 MHz, starting at 400°C and testing at 100°C intervals up to 700°C in an Ar gas atmosphere. The Nyquist plot was fitted by using an equivalent circuit model composed of a total resistance (R_{total}), its constant phase element (CPE_{total}), an electrode-electrolyte interface resistance (R_i), and its constant phase element (CPE_i), The ac conductivity (σ_{ac}) was estimated from the total resistance. In order to investigate polarization behavior, dc conductivity (σdc) was calculated as a function of time at 700°C in an Ar gas atmosphere by applying a dc current of 0.1 μA using a dc voltage/current generator (R6144, Advantest) and an electrometer (R8240, Advantest). Tubandt for $(Ca_{1-x}La_x)_2B_5O_9Cl_{1+2x}$ (x = 0.05) was measured at 600°C in air atmosphere by applying a dc voltage of 10V.

Computational Methods. The formation energies of point defects in $Ca_2B_5O_9Cl$ were evaluated using first-principles total energy calculations. First, we optimized the unit cell and positional parameters of $Ca_2B_5O_9Cl$. To calculate point defects, a supercell model containing 1 × 1 × 2 optimized unit cells was constructed. The total number of atoms in the perfect supercell model was 126. In this chapter, we investigated the following point defects: B vacancy (V_B), O vacancy (V_O), Cl vacancy (V_{Cl}), Ca vacancy (V_{Ca}), substitutional La at Ca site (La_{Ca}), interstitial O (O_i), and interstitial Cl (Cl_i). All the sites for each defect type were calculated. Candidates for interstitial sites of O and Cl were generated based on Voronoi polyhedral using the pymatgen code. The formation energies of point defects, $E_f(D^q)$ are obtained using the following relation:

$$E_f(D^q) = \{E(D^q) + E_{fcorr}(D^q)\} - E(\text{perfect}) - \sum_i n_i\mu_i + q(\varepsilon_{\text{VBM}} + \Delta\varepsilon_F) \qquad (3.1)^{42}$$

where $E(D^q)$ and E(perfect) are the total energies of a supercell with a defect D in the charge state q and of a perfect crystal supercell, respectively. n_i represents the number of i atoms removed ($n_i < 0$) or added ($n_i > 0$) to form defect D, and μ_i is the chemical potential of atom i. ε_{VBM} denotes the energy level of the valence band maximum, and $\Delta\varepsilon_f$ represents the Fermi level referenced to ε_{VBM}. $E_{corr}(D^q)$ corresponds to the sum of the image charge and potential alignment correction.[45] To determine the chemical potentials, we considered the condition of oxidation and chloridation limits that are consistent with the experimental conditions. Chemical potentials for the elements other than O and Cl were determined from the most stable phase in equilibrium on the convex hull in free energy-composition plots. The convex hull was obtained by calculating all possible phases in the system recorded in the Materials Project.[46]

First-principles calculations based on DFT were performed to investigate the optimized structure, defect formation energy, and migration energy using the projector augmented-wave (PAW) method implemented in the VASP code.[47–50] The exchange correlation term was treated with GGA-PBE.[51] The plane-wave cutoff energy was set to 550 eV. Integration in reciprocal spaces for the $Ca_2B_5O_9Cl$ supercell was performed using 2 × 2 × 4 and 2 × 2 × 2 Γ-centered grids for the unit cell and supercell, respectively. Structure optimization was conducted until all residual forces acting on each atom were less than 0.01 eV/Å. First-principles molecular dynamics simulations were also performed for Cl_i-La_{Ca} association model and O_i model with the *NVT* ensemble. The simulation cells were the same as those used for the point defect. The total simulation time was 100 ps with a time step of 2 fs. The first 10 ps were removed from the analysis. The temperature was set to 2000 K to detect atomic jumps, though it is higher than the experimental conditions. The migration energies of $Cl_i^{'}$ ion via the interstitialcy mechanism were calculated using the nudged elastic band (NEB) method with three intermediate images.[52,53]

3.3 Results and discussion

3.3.1 Crystal Structure

Colorless transparent single crystals of $Ca_2B_5O_9Cl$ were grown by the self-flux method using a $CaCl_2$ molten salt and extracted by washing the products with water. The phone is shown in Figure 3.1.

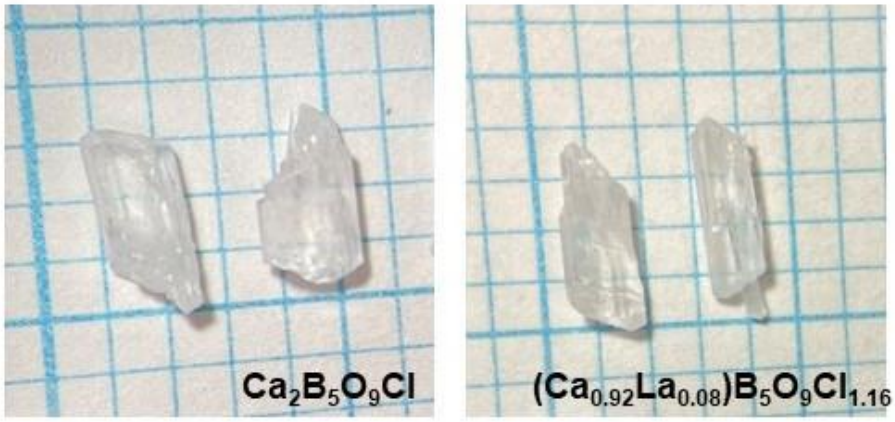

Figure 3.1 Photographs of single crystals of undoped (left) and La-doped (right) $Ca_2B_5O_9Cl$ on a 1mm-grid paper. The single crystals grew preferentially along the crystallographic *c*-axis.

The crystal structure of $Ca_2B_5O_9Cl$ determined by single-crystal structure analysis at room temperature, is shown in Figure 3.2. The borate chloride crystallizes in an orthorhombic cell (space group *Pnn*2) with cell parameters a = 11.3572(5) Å, b = 11.2309(4) Å, c = 6.3500(3) Å, and V = 809.95(6) Å^3. The crystallographic data including the atomic coordinates (Tables 3.1–3.3) are consistent with previous reports.[38] We notice that the Cl1 atoms placed at 2b Wyckoff positions are significantly underbonded against the surrounding Ca atoms compared with the Cl2 atoms at 2*a* positions: the bond-valence-sum (BVS) value for the Cl1 atom is 0.69, considerably smaller than 0.98 for the Cl2 atom, reflecting the difference in the $ClCa_4$

tetrahedral volume. The underbonding state of the Cl1 atom would be favorable for Cl^- ion migration.

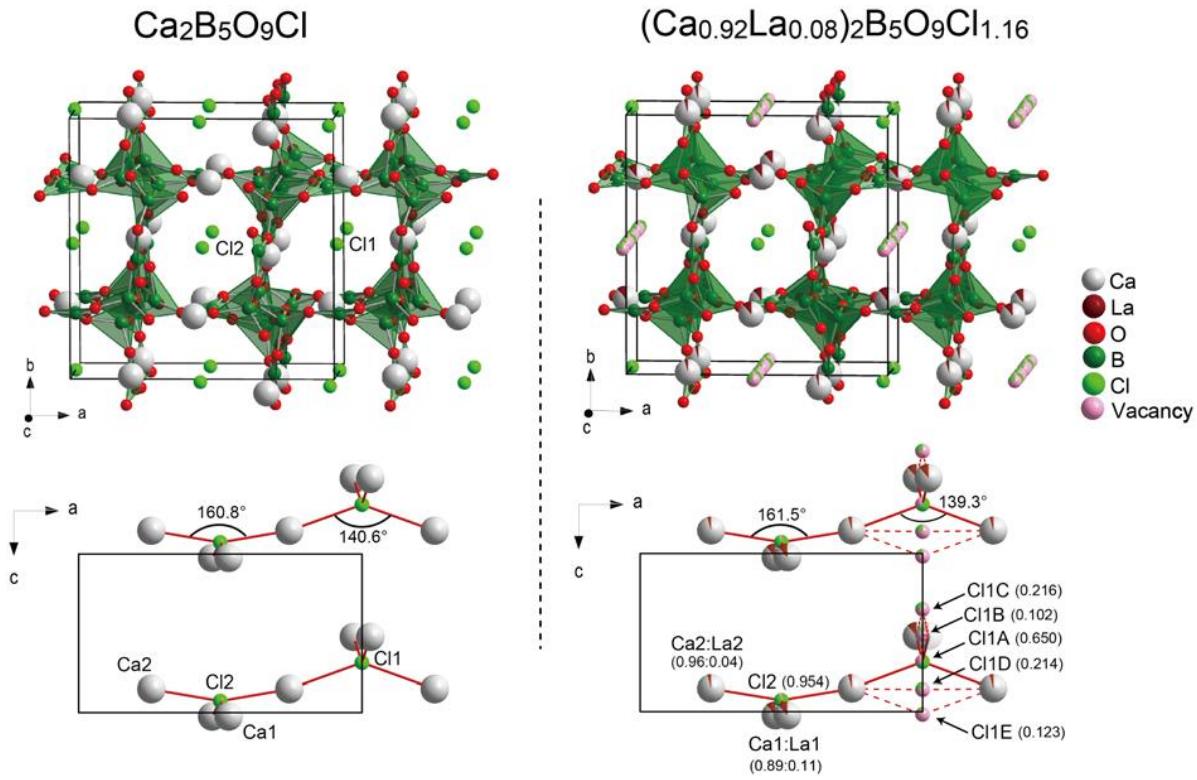

Figure 3.2 Crystal structures of $Ca_2B_5O_9Cl$ (left panels) and $(Ca_{0.92}La_{0.08})_2B_5O_9Cl_{1.16}$ (right panels) and the local coordination environment around Ca^{2+} ions, highlighting the Cl^- ion distribution. Site occupancy factors for the Ca/La and Cl atoms are presented in parentheses.

Table 3.1 Results of Structure Refinement of undoped and La-doped $Ca_2B_5O_9Cl$ Using Single-Crystal XRD Data.

Formula	$Ca_2B_5O_9Cl$	$(Ca_{0.92}La_{0.08})_2B_5O_9Cl_{1.16}$
Formula weight	313.66	335.14
Radiation	Mo *K*α (λ=0.71073 Å)	Mo *K*α (λ=0.71073 Å)
***T* (K)**	293	293
Crystal system	Orthorhombic	Orthorhombic
Space group	*Pnn*2	*Pnn*2
***a* (Å)**	11.3572(5)	11.3807(5)

***b* (Å)**	11.2309(4)	11.3109(6)
***c* (Å)**	6.3500(3)	6.3692(3)
***V* (Å^3)**	809.95(6)	819.88(7)
Z	4	4
***D*$_{calc}$ (g/cm^3)**	2.572	2.703
***F*$_{000}$**	616	648
no. of measured reflns	11503	5926
no. of unique reflns	2391	1636
no. of observed reflns ($F^2 > 2\sigma(F^2)$)	2391	1636
***R*$_{int}$ (%)**	5.64	3.01
$R[F^2 > 2\sigma(F^2)]/wR(F^2)$ (%)	4.34/6.53	2.87/5.87
GoF	1.07	1.08

Table 3.2 Refined Structural Parameters for the Single Crystal of $Ca_2B_5O_9Cl$.

atom	site	*x*	*y*	*z*	SOF[1]	U_{iso}/Å^2×10^2
Ca1	4c	-0.02906(8)	0.25646(8)	0.52456(15)	1	1.144(19)
Ca2	4c	-0.24359(9)	-0.03237(8)	0.35193(16)	1	1.030(19)
B1	4c	-0.1971(4)	0.2277(4)	0.0222(8)	1	0.65(9)
B2	4c	-0.3114(4)	0.2934(4)	0.3366(9)	1	0.67(9)
B3	4c	-0.2730(4)	0.1818(4)	0.6614(8)	1	0.56(10)
B4	4c	-0.2301(4)	0.0167(4)	0.8967(8)	1	0.80(11)
B5	4c	0.0237(4)	0.2576(4)	1.0655(7)	1	0.82(11)
O1	4c	-0.0905(3)	0.2672(2)	0.1319(4)	1	0.94(7)
O2	4c	-0.2959(2)	0.2978(3)	0.1084(5)	1	0.54(6)
O3	4c	-0.2753(3)	0.4006(2)	0.4579(5)	1	1.31(7)
O4	4c	-0.2479(3)	0.1950(2)	0.4391(4)	1	0.66(6)
O5	4c	-0.1903(2)	0.2534(2)	0.7928(5)	1	0.63(6)
O6	4c	-0.2559(2)	0.0516(3)	0.6977(5)	1	1.02(7)
O7	4c	-0.2139(3)	0.0972(2)	1.0570(4)	1	0.97(7)

O8	4c	0.0573(3)	0.2226(3)	0.8667(5)	1	1.08(7)
O9	4c	0.1040(3)	0.2856(3)	0.2185(5)	1	0.95(6)
Cl1	2a	0	0.5	0.6866(3)	1	2.00(4)
Cl2	2b	0	0	0.4261(3)	1	1.75(4)

[1] SOF stands for site occupancy factor.

Table 3.3 Anisotropic Displacement Parameters U_{ij} (Å^2) for $Ca_2B_5O_9Cl$.

atom	U_{11}	U_{22}	U_{33}	U_{23}	U_{13}	U_{12}
Ca1	0.0134(4)	0.0133(4)	0.0075(4)	-0.0001(4)	0.0014(4)	-0.0022(4)
Ca2	0.0138(5)	0.0105(4)	0.0066(4)	0.0000(4)	-0.0014(5)	-0.0016(4)
B1	0.009(2)	0.005(2)	0.006(2)	-0.0022(19)	-0.002(2)	0.0002(16)
B2	0.005(3)	0.009(2)	0.006(2)	-0.002(2)	0.001(2)	-0.0015(18)
B3	0.004(2)	0.007(2)	0.006(2)	0.0003(17)	-0.0016(19)	-0.0029(17)
B4	0.007(2)	0.009(2)	0.007(3)	0.0002(18)	-0.0004(19)	0.0017(18)
B5	0.008(2)	0.007(2)	0.009(3)	0.0038(18)	0.003(2)	-0.002(2)
O1	0.0047(15)	0.0184(17)	0.0051(16)	-0.0032(13)	0.0004(12)	0.0000(12)
O2	0.0052(15)	0.0071(15)	0.0040(15)	0.0003(12)	-0.0012(12)	0.0020(11)
O3	0.027(2)	0.0050(15)	0.0070(16)	-0.0002(12)	-0.0026(14)	-0.0039(13)
O4	0.0086(16)	0.0066(15)	0.0045(14)	0.0003(12)	-0.0007(13)	0.0011(11)
O5	0.0048(16)	0.0098(15)	0.0043(14)	-0.0017(12)	0.0011(11)	-0.0002(12)
O6	0.0180(17)	0.0041(16)	0.0084(16)	0.0010(12)	-0.0018(16)	0.0006(12)
O7	0.0184(17)	0.0079(15)	0.0028(16)	-0.0008(12)	-0.0006(13)	0.0020(12)
O8	0.0069(15)	0.0180(16)	0.0074(16)	-0.0033(13)	0.0010(15)	-0.0014(12)
O9	0.0057(15)	0.0175(15)	0.0053(15)	-0.0020(12)	-0.0003(13)	-0.0013(12)
Cl1	0.0189(9)	0.0135(8)	0.0277(10)	0.000	0.000	-0.0013(6)
Cl2	0.0108(8)	0.0127(8)	0.0289(9)	0.000	0.000	-0.0010(6)

However, the nearest neighbor (NN) distance between Cl ions in each 1D open channel is 6.3500(3) Å, much longer than those of fast chloride ion conductors (for example, 3.413(6) Å for $PbCl_2$ and 3.416(3) Å for LaOCl). Therefore, the introduction of interstitial chloride ions or site disorder into chloride ion channels is essential for facilitating Cl^- ion migration in $Ca_2B_5O_9Cl$. To examine the possibility of additional chloride ion insertion via the aliovalent substitution of Ca^{2+} by La^{3+}, a flux method using a $CaCl_2$ molten salt was employed again under conditions similar to those of undoped $Ca_2B_5O_9Cl$, but La_2O_3 was used as a La source with an atomic ratio of Ca/La = 31/1. La-doped $Ca_2B_5O_9Cl$ single crystals with similar morphologies and dimensions were obtained (Figure 3.1). SEM-EDX elemental analysis estimated the atomic ratio of Ca : La to be 1.80 : 0.21, that is, approximately 10% substitution of La for Ca (Figure 3.3). The cell volume was also found to increase by 1.2% (*a* = 11.3807(5) Å, *b* = 11.3109(6) Å, *c* = 6.3692(3) Å, and V = 819.88(7) $Å^3$), thereby maintaining structural symmetry. The cell expansion can be explained by considering the introduction of La^{3+}, which has a larger ionic radius (1.30 Å) than Ca^{2+} (1.26 Å), and the insertion of additional chloride ions, as discussed below. Single-crystal structure analysis at the initial stages could readily identify the borate framework composed of $(B_5O_9)^{3-}$ units and the random occupations of two nonequivalent 4*c* sites by Ca and La atoms in ratios of 0.89/0.11 (Ca1/La1) and 0.96/0.04 (Ca2/La2), respectively. The total atomic ratio of Ca to La determined by SCXRD was consistent with the results of the EDX measurements. Further structural analysis revealed not only a substantial reduction in the occupancy (g = 0.65) of the Cl1A atom corresponding to the Cl1 atom in the undoped phase but also the presence of interstitial chloride ions within the Cl1 channels at Cl1B: 1.10(4) Å, Cl1C: 2.12(2) Å, Cl1D: 1.10(2) Å, and Cl1E: 2.10(4) Å from the Cl1A site, which are even shorter than the NN distances between the chloride ions in the undoped phase. The site occupancies of Cl1B–Cl1E were refined to 0.102, 0.216, 0.214, and 0.123, respectively, based on the overall charge valence. The chloride site disorder in the Cl1

channels contrasts with the absence of interstitial chloride ions and almost no Cl2 site vacancies (g = 0.954) within the Cl2 channels.

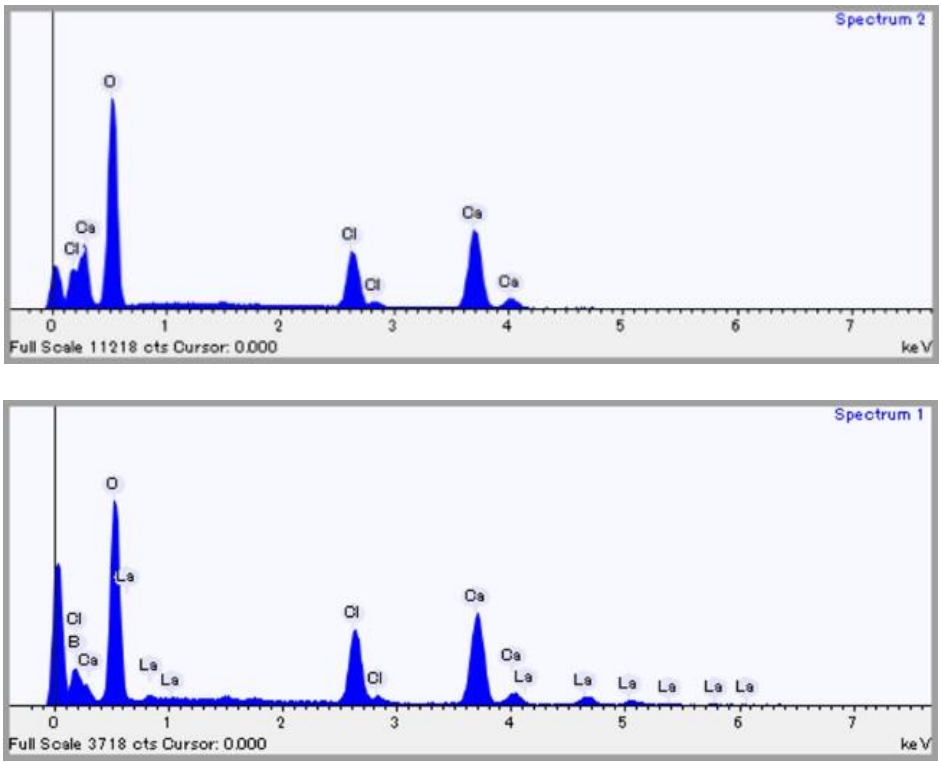

Figure 3.3 EDX spectra of undoped (upper panel) and La-doped (lower panel) $Ca_2B_5O_9Cl$. The EDX analysis indicates that the molar ratio of Ca/Cl/La is 2.00/1.14/0 and 1.80/1.21/0.21, which are consistent with the results of single-crystal structure analysis.

The final refined chemical composition was $(Ca_{0.92}La_{0.08})_2B_5O_9Cl_{1.16}$. The final refined crystal structure and crystallographic data are shown in Figure 3.2 and Table 3.1, Table 3.4, and Table 3.5.

Table 3.4 Refined Structural Parameters for the Single Crystal of $(Ca_{0.92}La_{0.08})_2B_5O_9Cl_{1.16}$.

atom	site	*x*	*y*	*z*	SOF[1]	U_{iso}/Å^2×10^2
Ca1	4c	-0.02098	0.26466	0.52476	0.889	1.95(3)
Ca2	4c	-0.24941	-0.02796	0.35481	0.957	1.46(3)

La1	4c	-0.02098	0.26466	0.52476	0.111	1.95(3)
La2	4c	-0.24941	-0.02796	0.35481	0.043	1.46(3)
B1	4c	-0.1904	0.2292	0.0255	1	0.94(11)
B2	4c	-0.3021(5)	0.3006(5)	0.3374(10)	1	0.96(11)
B3	4c	-0.2641(5)	0.1907(5)	0.6640(9)	1	0.90(12)
B4	4c	-0.2329(5)	0.0237(5)	0.8980(10)	1	1.23(15)
B5	4c	0.0332(5)	0.2494(5)	1.0637(10)	1	1.23(15)
O1	4c	-0.0799(3)	0.2559(3)	0.1342(6)	1	1.74(9)
O2	4c	-0.2699(3)	0.4083(3)	0.4597(6)	1	1.88(9)
O3	4c	-0.2824(3)	0.3072(3)	0.1134(6)	1	1.12(8)
O4	4c	-0.2372(3)	0.2041(3)	0.4431(6)	1	1.16(8)
O5	4c	-0.1803(3)	0.2561(3)	0.7967(6)	1	0.96(8)
O6	4c	-0.2508(3)	0.0602(3)	0.6969(6)	1	1.44(8)
O7	4c	-0.2204(3)	0.1028(3)	1.0592(6)	1	1.52(8)
O8	4c	0.0674(3)	0.2192(3)	0.8646(6)	1	1.39(8)
O9	4c	0.1147(3)	0.2718(3)	0.2198(6)	1	1.32(8)
Cl1A	2b	0	0.5	0.6876	0.65	2.99(8)
Cl1B	2b	0	0.5	0.515	0.102	2.99(11)
Cl1C	2b	0	0.5	0.354	0.216	2.99(11)
Cl1D	2b	0	0.5	0.861	0.214	2.99(11)
Cl1E	2b	0	0.5	1.018	0.123	2.99(11)
Cl2	2a	0	0	0.4277	0.954	1.77(6)

[1] SOF stands for site occupancy factor.

Table 3.5 Anisotropic Displacement Parameters U_{ij} (Å^2) for $(Ca_{0.92}La_{0.08})_2B_5O_9Cl_{1.16}$.

atom	U_{11}	U_{22}	U_{33}	U_{23}	U_{13}	U_{12}
Ca1	0.0129(4)	0.0382(6)	0.0073(4)	0.0016(5)	0.0011(4)	0.0011(4)
Ca2	0.0247(5)	0.0116(5)	0.0075(5)	0.0012(4)	0.0001(4)	-0.0040(4)

La1	0.0129(4)	0.0382(6)	0.0073(4)	0.0016(5)	0.0011(4)	0.0011(4)
La2	0.0247(5)	0.0116(5)	0.0075(5)	0.0012(4)	0.0001(4)	-0.0040(4)
B1	0.008(2)	0.009(2)	0.011(3)	0.002(3)	-0.004(3)	-0.002(2)
B2	0.007(2)	0.012(3)	0.009(3)	0.000(2)	0.000(2)	0.002(2)
B3	0.005(3)	0.009(3)	0.013(3)	0.003(2)	0.000(2)	0.002(2)
B4	0.014(3)	0.012(3)	0.011(5)	0.000(2)	0.001(2)	0.000(2)
B5	0.010(2)	0.012(3)	0.015(5)	0.000(2)	-0.004(3)	0.000(3)
O1	0.0071(16)	0.033(2)	0.012(2)	-0.0025(17)	-0.0004(15)	-0.0032(16)
O2	0.034(2)	0.0117(17)	0.0106(19)	-0.0005(15)	-0.0012(17)	-0.0058(17)
O3	0.0167(18)	0.0129(18)	0.0040(18)	0.0010(15)	-0.0008(15)	0.0052(14)
O4	0.0137(17)	0.0148(17)	0.0062(17)	0.0009(14)	0.0022(15)	0.0050(15)
O5	0.0115(18)	0.0105(17)	0.0068(18)	0.0005(13)	0.0004(14)	-0.0008(15)
O6	0.025(2)	0.0094(19)	0.009(2)	-0.0008(16)	-0.0020(17)	0.0012(15)
O7	0.0271(19)	0.0094(17)	0.009(2)	-0.0020(15)	0.0008(16)	-0.0018(15)
O8	0.0076(17)	0.0242(19)	0.010(2)	-0.0042(16)	0.0009(17)	-0.0007(14)
O9	0.0082(17)	0.0238(19)	0.0077(18)	-0.0007(16)	-0.0015(15)	-0.0023(15)
Cl1A	0.0269(15)	0.0145(16)	0.0485(17)	0.000	0.000	-0.0002(13)
Cl1B	0.027(2)	0.0145(15)	0.0485(16)	0.000	0.000	-0.0002(17)
Cl1C	0.027(2)	0.0145(15)	0.0485(16)	0.000	0.000	-0.0002(17)
Cl1D	0.027(2)	0.0145(15)	0.0485(16)	0.000	0.000	-0.0002(17)
Cl1E	0.027(2)	0.0145(15)	0.0485(16)	0.000	0.000	-0.0002(17)
Cl2	0.0088(9)	0.0147(10)	0.0296(12)	0.000	0.000	-0.0005(7)

3.3.2 Polycrystalline samples of $(Ca_{1-x}La_x)_2B_5O_9Cl_{1+2x}$ (x = 0–0.15) solid solutions

From the chloride site disorder observed by the single-crystal structure analysis, we can

expect Cl^- ion conduction, especially along the Cl1 channels. To investigate the possible chloride ion conductivity and carrier concentration dependence, polycrystalline samples of $(Ca_{1-x}La_x)_2B_5O_9Cl_{1+2x}$ (x = 0–0.15) solid solutions were synthesized using a conventional solid-state reaction. Figure 3.4 shows the room temperature PXRD patterns of the La-doped $Ca_2B_5O_9Cl$ along with the data for the undoped phase.

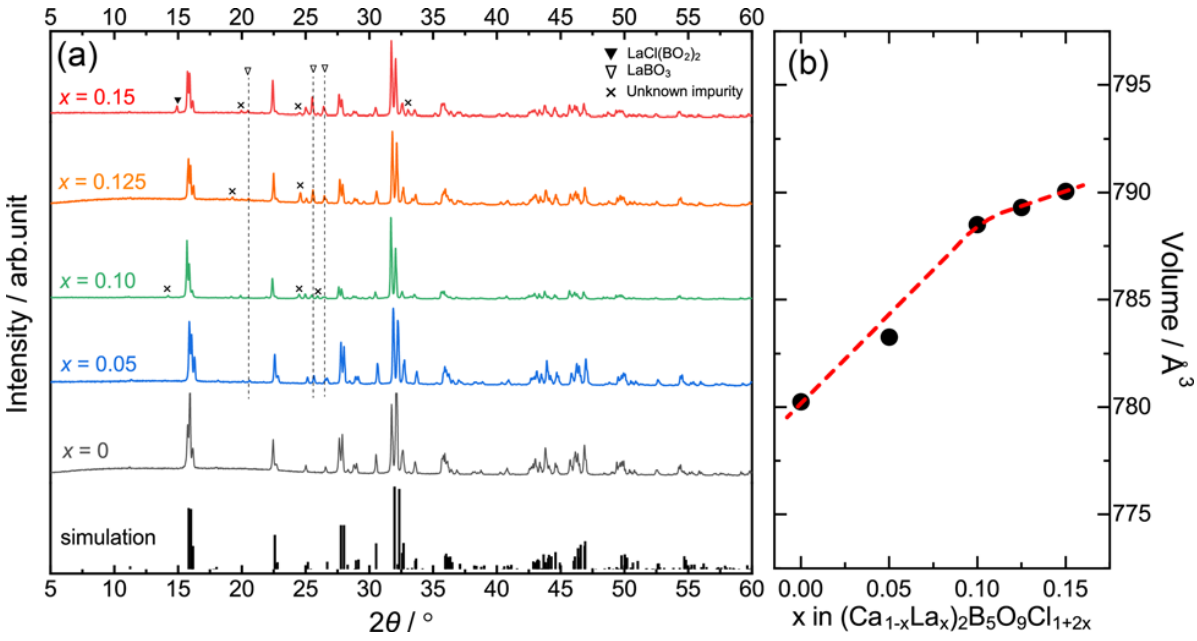

Figure 3.4 (a) Powder X-ray diffraction patterns of $(Ca_{1-x}La_x)_2B_5O_9Cl_{1+2x}$ (x = 0–0.15) solid solutions recorded at room temperature. (b) The cell volume as a function of x in $(Ca_{1-x}La_x)_2B_5O_9Cl_{1+2x}$. The dashed line is a guide to the eye.

All solid solutions could be obtained as the main phase, but several tiny peaks assigned to $LaBO_3$ and/or $La(BO_2)_2Cl$ were detected, suggesting deviation from the nominal chemical compositions. The cell volume increased monotonically with an increase in $x \leq 0.10$; however, it remained almost unchanged at $0.125 \leq x$. It is likely that the solid solubility limit was between 0.10 and 0.125.

3.3.3 Humidity and thermal stability

Undoped $Ca_2B_5O_9Cl$ exhibit excellent humidity and thermal stability, polycrystalline samples PXRD measurements were conducted after the preparation of polycrystalline samples, which were then placed in an atmospheric environment. After several days, none of the PXRD results changed (Figure 3.5). Thermal stability was assessed using PXRD results before and after placing the samples at various temperatures, either in N_2 or O_2 atmospheres, with no changes observed in the PXRD patterns (Figure 3.6). Moreover, for La-doped $Ca_2B_5O_9Cl$ samples, the thermal stability in a flowing N_2 and O_2 gas atmosphere was studied using thermogravimetric and differential thermal analysis (TG-DTA) measurements of $x = 0.1$. The TG curve remained largely unchanged up to 700°C, indicating that the sample shows minimal decomposition. The DTA curve displayed no sharp peaks, implying that there is no phase change in the sample. No change in PXRD pattern after TG measurements also illustrates the excellent thermal stability of the samples (Figure 3.7).

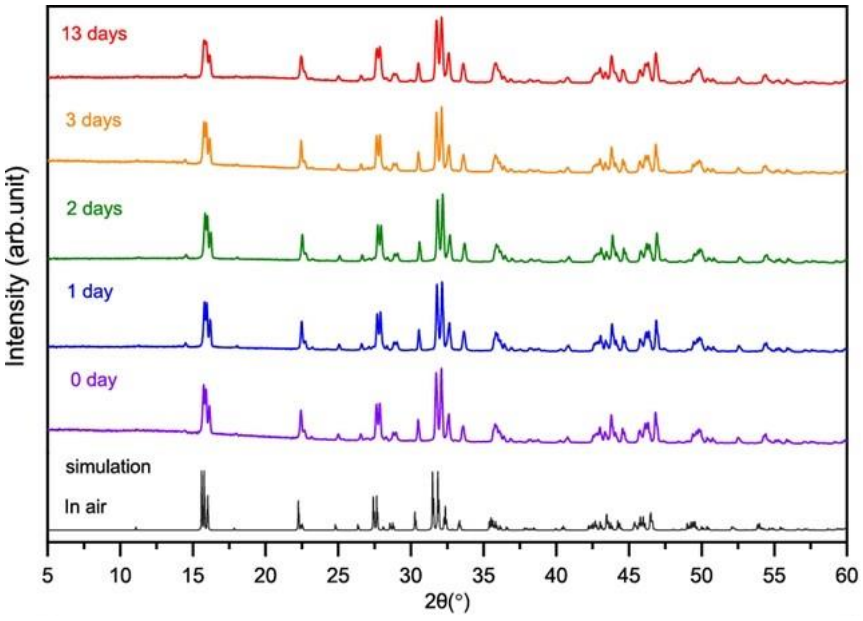

Figure 3.5 Stability of $Ca_2B_5O_9Cl$ in air atmospheres. Room-temperature PXRD patterns collected from the borate chloride after 1–13 days of exposure to air atmosphere. No change in XRD patterns was observed under these experimental conditions.

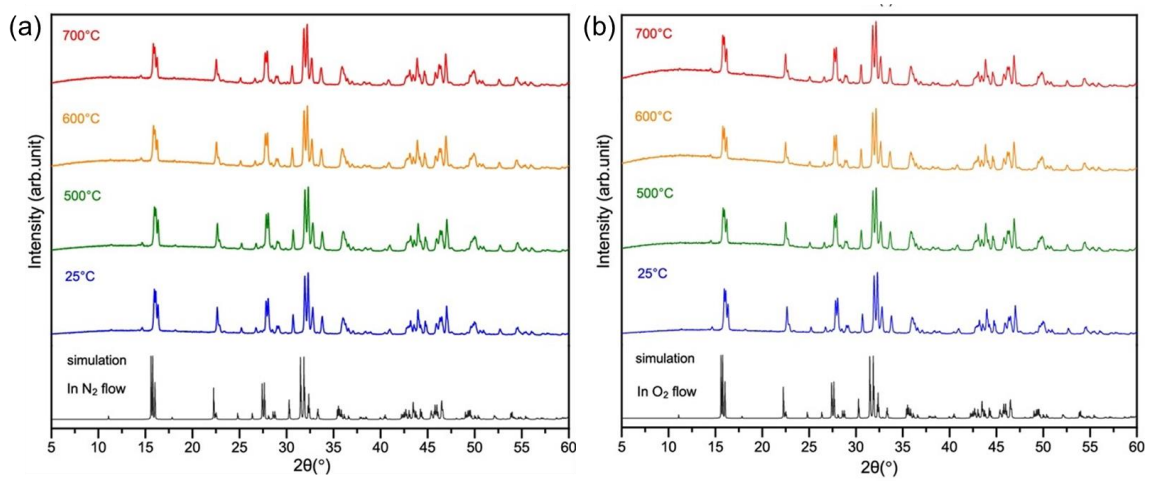

Figure 3.6 Stability of $Ca_2B_5O_9Cl$ in N_2 and O_2 gas atmospheres. Room-temperature PXRD patterns collected from the borate chloride after heating at several temperatures in N_2 or O_2 gas atmosphere. No change in XRD patterns was observed under these experimental conditions.

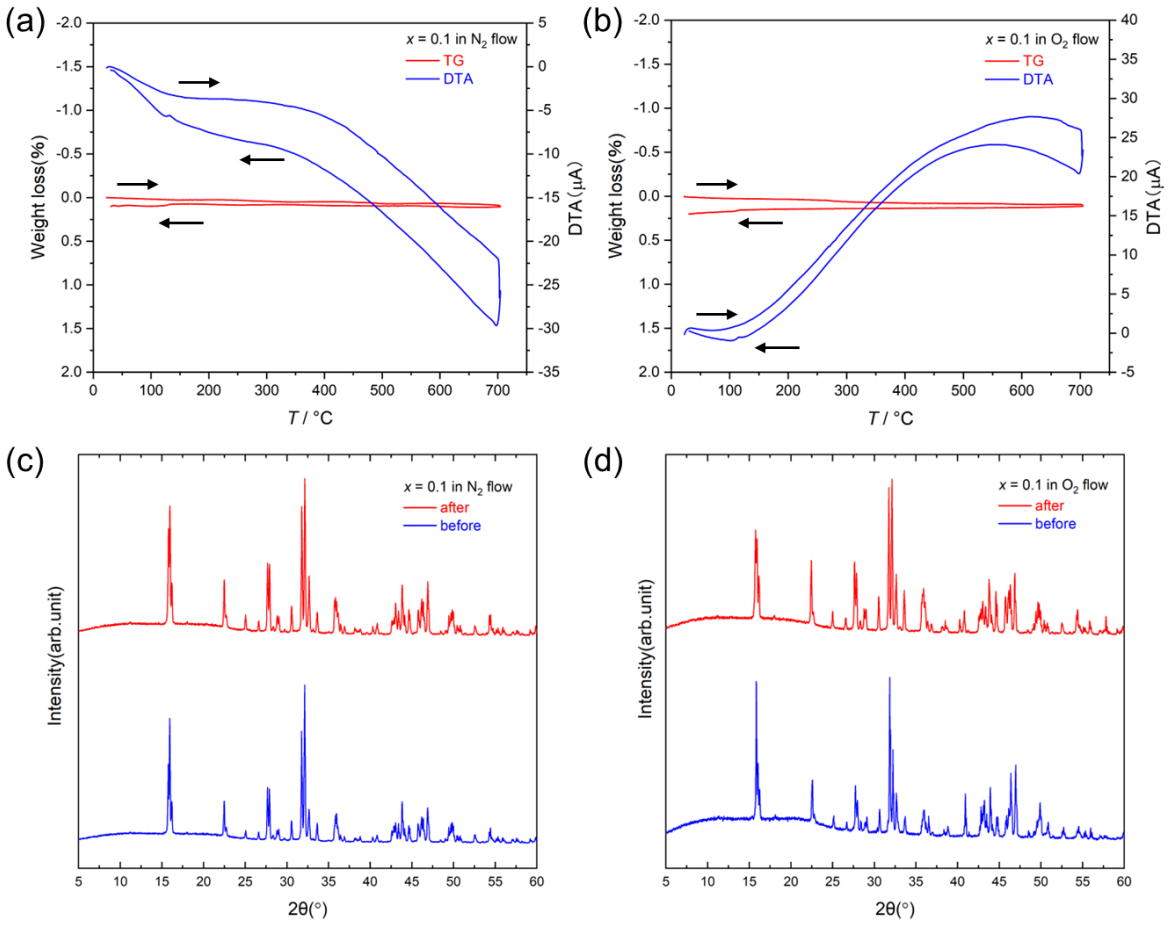

Figure 3.7 (a)(b) TG-DTA curves of x = 0.10 in a N_2 and O_2 gas atmosphere. The weight change was negligible within the instrumental resolutions. (c)(d) Room-temperature PXRD patterns of x = 0.10 before and after the TG-DTA measurements. It remained unchanged after heating up to 700°C in N_2 and O_2 gas.

3.3.4 Conductive property of $(Ca_{1-x}La_x)_2B_5O_9Cl_{1+2x}$ (x = 0–0.15)

The typical Nyquist plots of $(Ca_{1-x}La_x)_2B_5O_9Cl_{1+2x}$ (x = 0–0.15) were recorded by impedance methods in an Ar gas atmosphere. The data obtained at 400, 500, 600, and 700 °C are shown in Figure 3.8. For each sample, the plot was fitted using a total resistance (R_{total}), its constant phase element (CPE_{total}), an electrode–electrolyte interface resistance (R_i), and its constant phase element (CPE_i), where the total components include the contributions from bulk and grain boundary components.

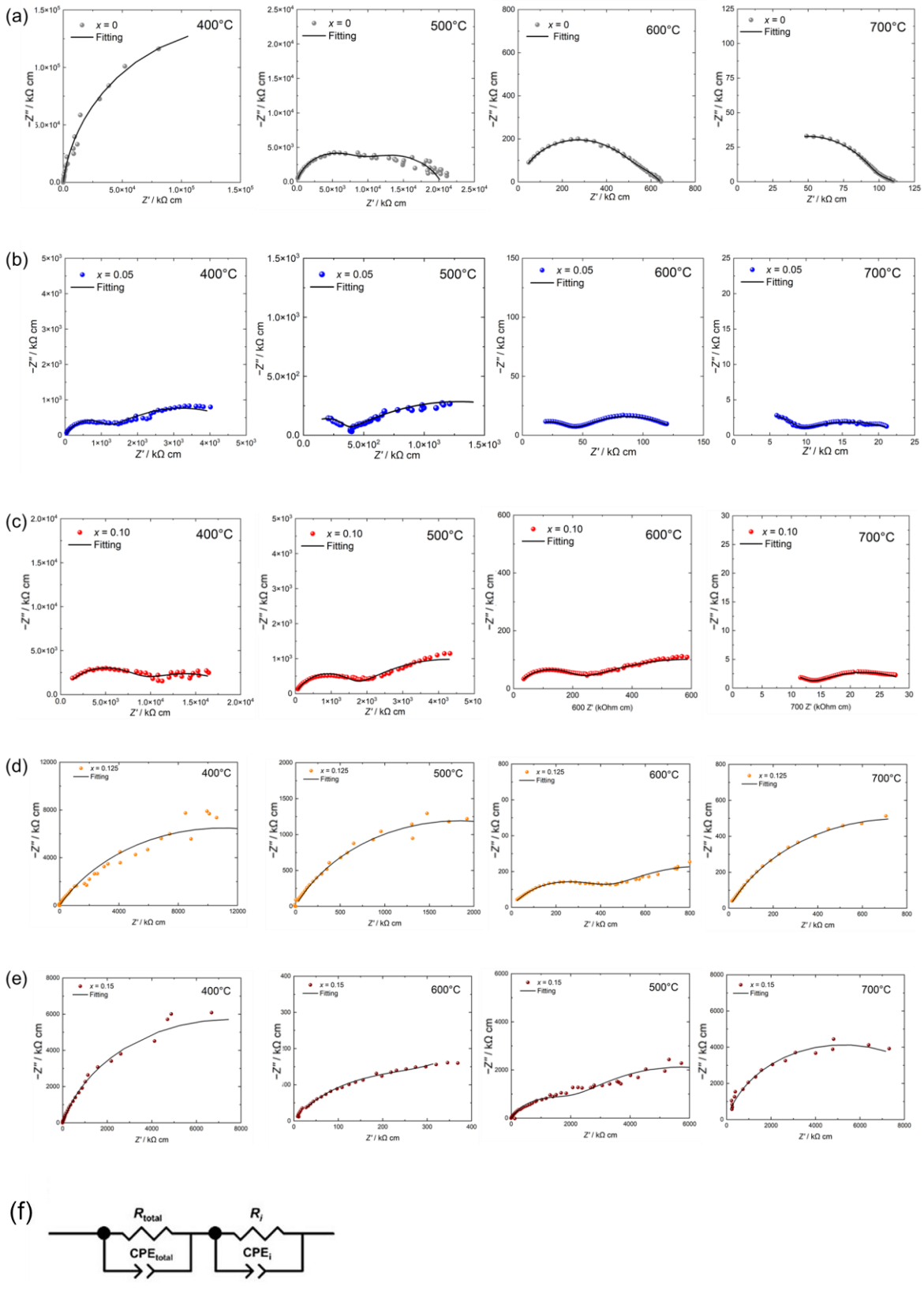

Figure 3.8 (a-e) Representative Nyquist plots of $(Ca_{1-x}La_x)_2B_5O_9Cl_{1+2x}$ (x = 0–0.15) solid

solutions recorded under an Ar gas atmosphere at 400, 500, 600, and 700 °C in an Ar gas atmosphere. Fitting curves are indicated by black lines. (f) Equivalent circuit model used to fit all data: a total resistance (R_{total})including bulk and grain-boundary resistances, its constant phase element (CPE_{total}), an electrode-electrolyte interface resistivity (R_i), and its constant phase elements (CPE_i).

The temperature dependence of the ac conductivity (σ_{ac}) of $(Ca_{1-x}La_x)_2B_5O_9Cl_{1+2x}$ (x = 0–0.15) solid solutions was estimated from the total resistance (Figure 3.9). The σ_{ac} of the undoped phase is comparable to the ionic conductivity of LaOCl at 600–700 °C, and on the order of 10^{-5} S cm^{-1} at 700 °C. Interestingly, 5% La doping into $Ca_2B_5O_9Cl$ improved the conductivity of x = 0 by more than one order of magnitude. x = 0.05 exhibits the highest conductivity of 1.32×10^{-4} S cm^{-1} at 700 °C.

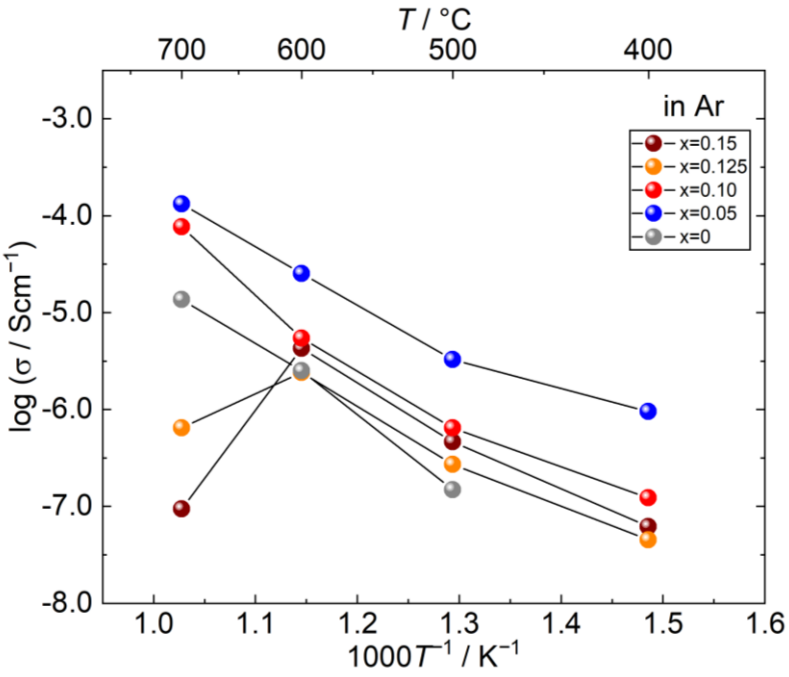

Figure 3.9 Arrhenius plots of the ac conductivity (σ_{ac}) of $(Ca_{1-x}La_x)_2B_5O_9Cl_{1+2x}$ (x = 0–0.15) as a function of temperature.

The conductivities of $(Ca_{1-x}La_x)_2B_5O_9Cl_{1+2x}$ are lower than those of ball-milled $La_{0.8}Ca_{0.2}OCl_{0.8}$ but become comparable to those of non-ball-milled $La_{0.8}Ca_{0.2}OCl_{0.8}$ with increasing temperature (Figure 3.10).

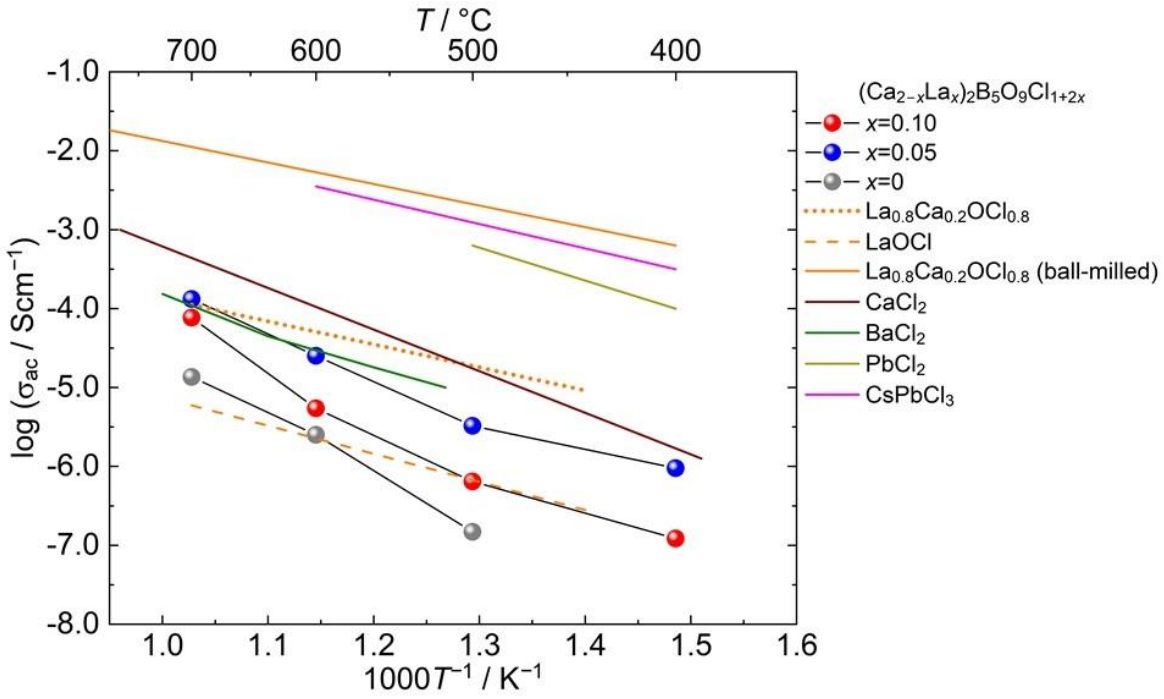

Figure 3.10 Comparison of the ac conductivity of $(Ca_{1-x}La_x)_2B_5O_9Cl_{1+2x}$ (x = 0, 0.05, 0.10) with those of conventional chloride-ion conductors.

The enhanced conductivity of $(Ca_{1-x}La_x)_2B_5O_9Cl_{1+2x}$ can be attributed to the increased carrier (or chloride ion) concentration and the presence of interstitial chloride ions. However, a further increase ($x \geq 0.125$) in the amount of La doping tends to reduce the conductivity, which is probably because of the overdoping effects associated with clustering among the dopants (La^{3+} ions) and interstitial chloride ions. The activation energy (E_a) of $(Ca_{1-x}La_x)_2B_5O_9Cl_{1+2x}$ estimated using the Arrhenius equation is 1.67, 1.1, and 1.21 eV for x = 0, 0.05, and 0.10, respectively. 5–10% La doping into $Ca_2B_5O_9Cl$ reduces the activation energy in comparison with that of the undoped phase. To gain insight into the conducting species in $(Ca_{1-x}La_x)_2B_5O_9Cl_{1+2x}$, polarization measurements for x = 0.05 were carried out at 700 °C in an

Ar gas atmosphere (Figure 3.11). The time evolution of σ_{dc}/σ_{ac}, where σ_{dc} stands for the DC conductivity, exhibited a considerably high degree of polarization ($\sigma_{dc}/\sigma_{ac} < 0.1$ over 30 min), suggesting that ions are the dominant migrating species, not electrons, as expected from its high insulating nature.

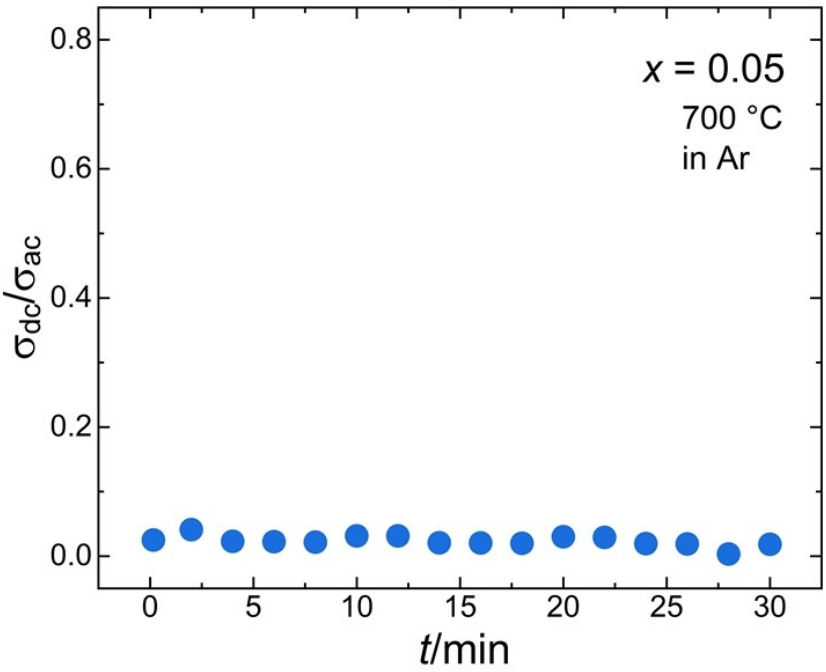

Figure 3.11 Polarization behavior for $(Ca_{1-x}La_x)_2B_5O_9Cl_{1+2x}$ (x = 0.05) in Ar gas atmosphere at 700°C.

3.3.5 First-principles calculation for $(Ca_{1-x}La_x)_2B_5O_9Cl_{1+2x}$

To understand the defect chemistry of $Ca_2B_5O_9Cl$, the formation energies of point defects were investigated using first-principles calculations. Figure 3.12 shows the plots of the calculated formation energies against the variation of the Fermi level under the assumed equilibrium condition of oxidation and chloridation limits. For each defect type, the most stable sites are depicted. The gradient of the lines in the plot indicates the charge states of defects. A positive (negative) slope of the lines of defect formation energy indicates a donor (acceptor)-type defect. The Fermi level position in the band gap balances the concentrations of positive

and negative point defects and electronic carriers (holes and electrons) to meet the condition of charge neutrality.

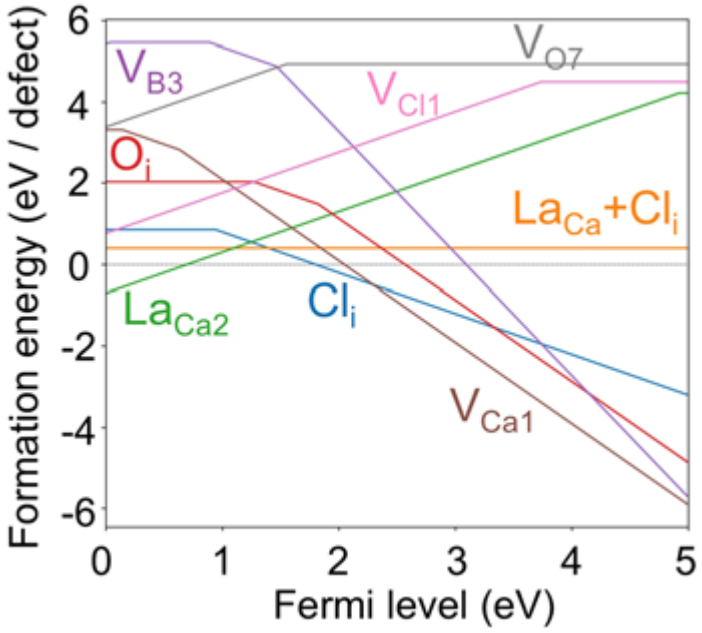

Figure 3.12 Formation energies of point defects as a function of the Fermi level on oxidation and chloridation limits. For each defect type, only the most stable sites are depicted.

In the $Ca_2B_5O_9Cl$ system, the concentrations of positive and negative point defects determine the Fermi level because of its high insulation (Figure 3.13). As seen in Figure 3.12, $La^{\cdot}_{Ca}$ and $Cl^{'}_{i}$ have the lowest formation energies for positive and negative point defects, respectively, and thus, these defects should be dominant over the other defects. $La^{\cdot}_{Ca}$ and $Cl^{'}_{i}$ stand for a La atom on a Ca site with single positive charge and a Cl atom on an interstitial site with single negative charge, respectively, in Kröger–Vink notation. The association energy between $La^{\cdot}_{Ca}$ and $Cl^{'}_{i}$ was also estimated to be 0.70 eV from all possible configurations of $La^{\cdot}_{Ca}$ in the cell containing the most stable $Cl^{'}_{i}$. The formation energies of the complex defects of $La^{\cdot}_{Ca}$ and $Cl^{'}_{i}$ are lower than those of isolated $La^{\cdot}_{Ca}$ and $Cl^{'}_{i}$ under the condition of charge neutrality, suggesting the presence of these associated defects in La-doped $Ca_2B_5O_9Cl$.

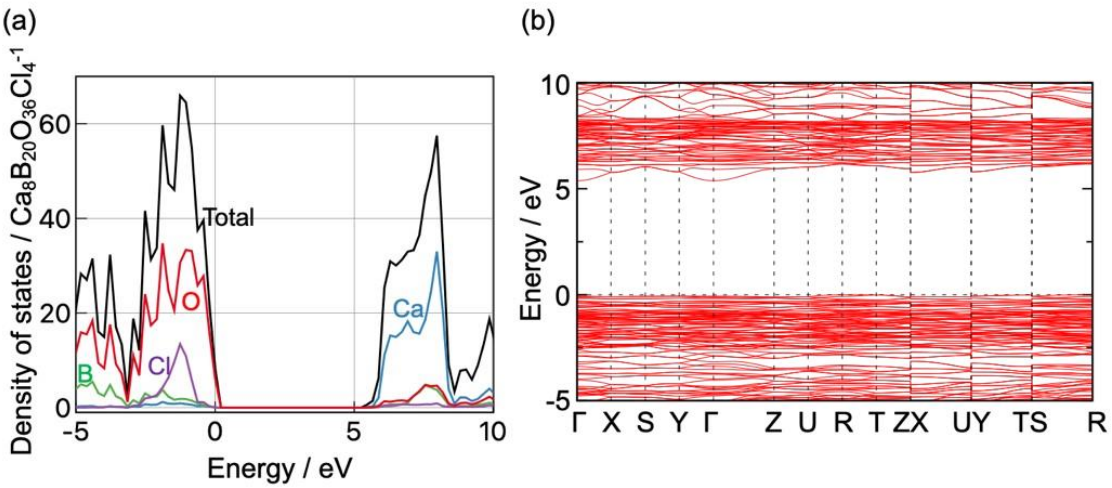

Figure 3.13 (a) Total and partial density of states and (b) band diagrams of $Ca_2B_5O_9Cl$. The band gap value was calculated to be 5.4 eV, very close to that previously reported value obtained by DFT calculations using the PBEsol exchange-correlation functional. The band gap value estimated from UV-vis spectrum is 7.3 eV. Underestimation of the band gap value is typical of DFT calculations using semi-local functionals.

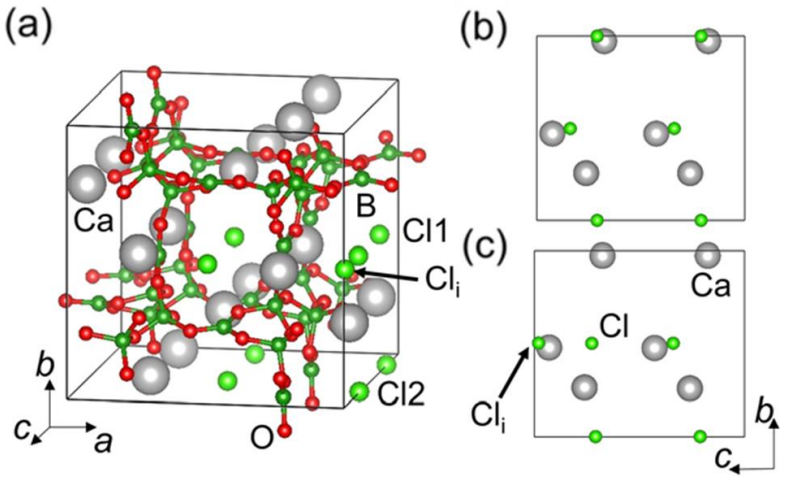

Figure 3.14 (a) Obtained structure with the most stable Cl'_i, (b)(c) obtained structure seen from the *a*-axis of perfect crystal and point defect models with Cl'_i, only Cl and Ca are drawn in the range of the internal coordinates of the a-axis from 0.6 to 1.0. The structure models were drawn using the VESTA program.

Figure 3.14a shows the calculated structure containing the most stable Cl'_i, which is located in the Cl1 channel. Figure 3.14b and Figure 3.14c show the structures of the perfect crystal and Cl'_i defect models, respectively, viewed along the *a*-axis. For clarity, only Ca and Cl atoms are drawn in the range of internal coordinates of the *a*-axis from 0.6 to 1.0. It should be noted that the Cl atom at the original Cl1 site closest to the interstitial Cl atom is significantly displaced along the *c*-axis. This result is consistent with the single-crystal structure analysis, revealing complex Cl-site disorder in the Cl1 channel.

Based on the results of the single-crystal structure analysis and point defect calculations, Cl'_i should be a dominant conduction species. To identify chloride ion diffusion and its conduction mechanism, first-principles molecular dynamics calculations were performed for the association model involving $La^{\cdot}_{Ca}$ and Cl'_i. The O_i model, which has a higher formation energy than Cl'_i, was also used to determine whether oxide ion conduction occurred. The Cl^- ion distribution density revealed 1D Cl^- ion diffusion along the *c*-axis in the Cl1 channel during the simulation of the Cl'_i model, while the Cl ions in other channels remained stationary (Figure 3.15).

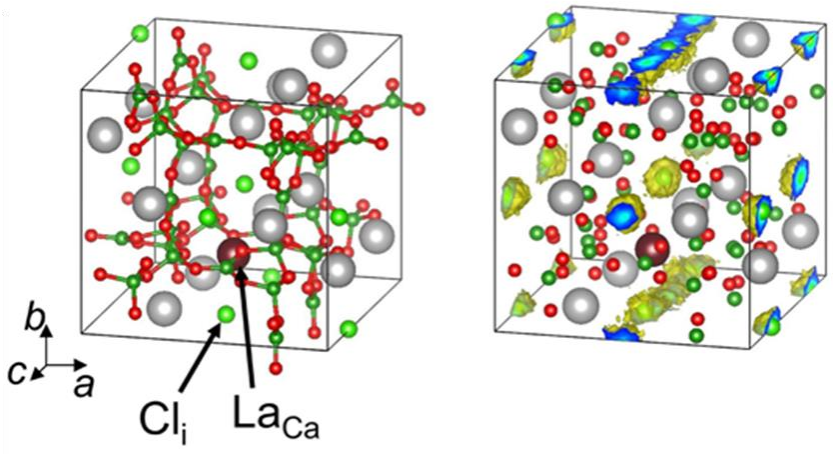

Figure 3.15 The most stable structure containing complex defects of $La^{\cdot}_{Ca}$ and Cl'_i (left) and the corresponding atomic distribution of Cl during molecular dynamics simulation (right).

The root mean square displacement (RMSD) result clearly showed only Cl jumps associated with the diffusion of Cl atoms, in contrast to the absence of jumps of the other elements, including O atoms (Figure 3.16). Furthermore, the root square displacement (RSD) calculations for Cl atoms revealed that three Cl atoms in the Cl1 channel cooperatively jump (Figure 3.17). In contrast, no jumps of the O atoms were observed in the Oi model (Figure 3.18). Therefore, we can conclude that Cl'_i is the dominant point defect for ionic conduction.

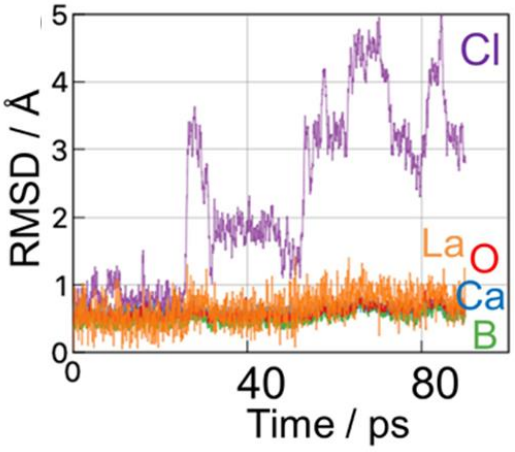

Figure 3.16 Root mean square displacements (RMSD) during molecular dynamics simulations of the model containing complex defects of $La^{\cdot}_{Ca}$ and Cl'_i.

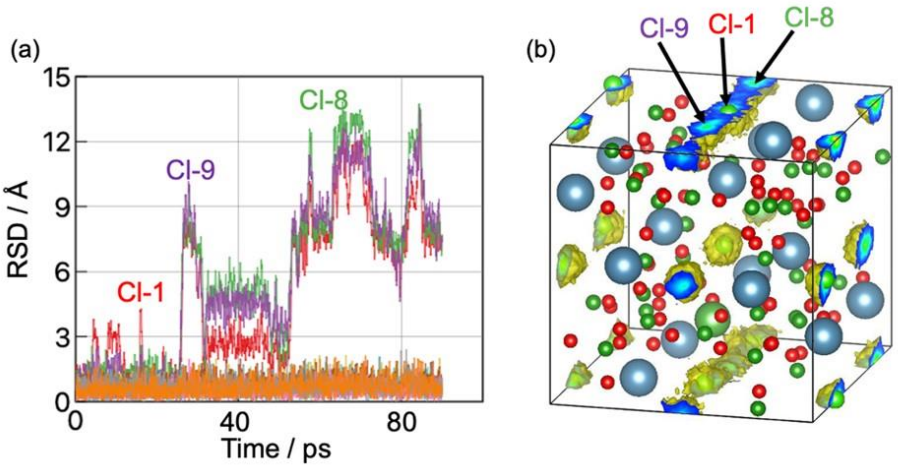

Figure 3.17 (a) Root square displacements (RSD) for each Cl during molecular dynamics simulations of the model containing a complex defect of $La^{\cdot}_{Ca}$ and Cl'_i. (b) Cl-1, Cl-8, and Cl-9 atoms in (a).

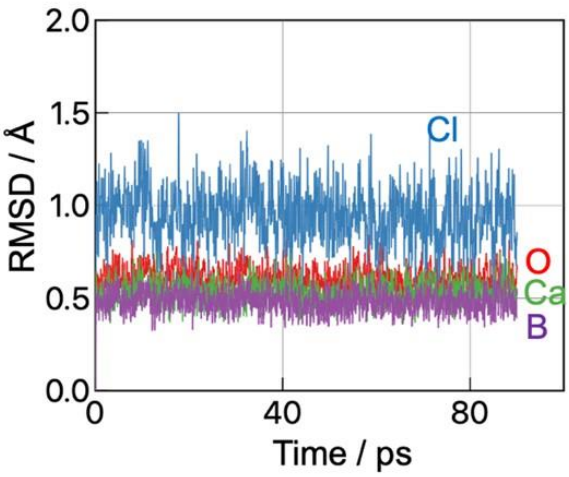

Figure 3.18 Root mean square displacements (RMSD) for the O_i model during molecular dynamics simulations.

Chloride ion migration in $Ca_2B_5O_9Cl$ was also investigated by nudged elastic band (NEB) calculations for two models of the Cl'_i point defect and associated defects with $La^{\cdot}_{Ca}$ and Cl'_i via the interstitialcy mechanism. The estimated energy barrier for the Cl ion migration in the former model was 0.52 eV (Figure 3.19a). This value is much lower than the experimental activation energies of $(Ca_{1-x}La_x)_2B_5O_9Cl_{1+2x}$. The discrepancy between the experimental and calculated values can be attributed to the formation of Cl'_i and the association between $La^{\cdot}_{Ca}$ and Cl'_i in the undoped and La-doped phases, respectively. Assuming that conducting Cl'_i is perfectly released from the association with La in the dilute state of the La-doped system, the activation energy can be expressed as the sum of the migration energy of Cl'_i and the association energy of $La^{\cdot}_{Ca}$–Cl'_i. This value was 1.22 eV, which is higher than that of $x = 0.05$, implying the possibility that conducting Cl is not fully released from the association with the dopant like other ionic conductors. Thus, the migration energy of Cl'_i in the association model of a 1 × 1 × 3 supercell with $Ca_{23}La_1Cl_{13}B_{60}O_{108}$ ($x = 0.0417$) was calculated yielding 1.05 eV (Figure 3.19b). This value agrees well with the experimental E_a value for $x = 0.05$, which suggests that the association with $La^{\cdot}_{Ca}$ significantly affects the activation energy of Cl'_i

conduction in La-doped $Ca_2B_5O_9Cl$. Since the migration energy of free $Cl^{\cdot}_i$ from association with La in $Ca_2B_5O_9Cl$ is comparable to those of related metal (oxy)chlorides, for example 0.54 eV for $La_{0.8}Ca_{0.2}OCl_{0.8}$ and 0.15–0.69 eV for $CsSnCl_3$, optimizing dopant species and compositions could improve the ionic conductivity of $Ca_2B_5O_9Cl$.

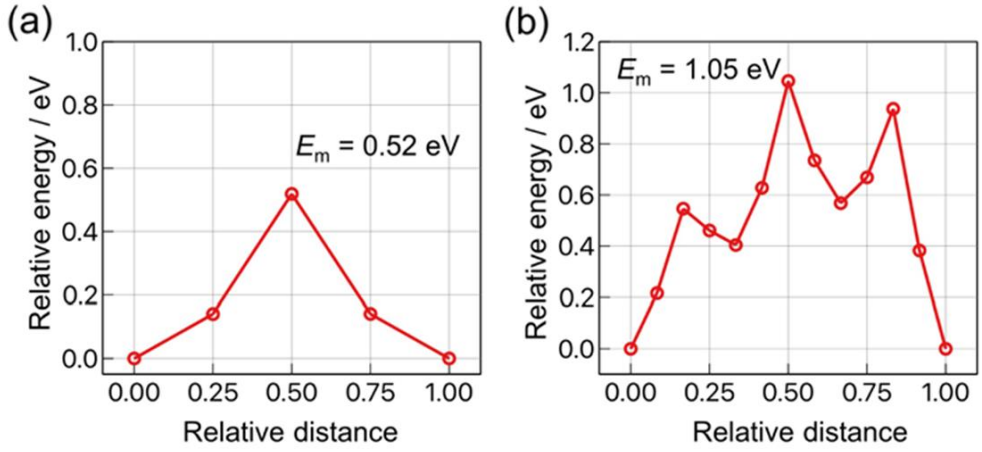

Figure 3.19 Migration energy of $Cl^{\cdot}_i$ in models with (a) the point defect $Cl^{\cdot}_i$ and (b) complex defects of $La^{\cdot}_{Ca}$ and $Cl^{\cdot}_i$.

3.4 Summary of Chapter 3

In summary, we demonstrated a unique strategy to design chloride-ion conducting channels using an open borate framework compound, $(Ca_{1-x}La_x)_2B_5O_9Cl_{1+2x}$, which is the first to exhibit one-dimensional chloride-ion transport defined by the dimensionality of the borate framework. The aliovalent substitution of La^{3+} for Ca^{2+} causes an increase in the concentration of chloride ions in one of the two non-equivalent chloride-ion channels surrounded by covalent $(B_5O_9)^{3-}$ units, involving significant chlorine deficiencies at the original site and site disorder along the channels. No oxygen deficiencies or disorder occurred, in contrast to oxide-ion conducting oxyhalides. First-principles molecular dynamics simulations show one-dimensional cooperative diffusion of interstitial chloride ions along the chloride-ion channels. The calculations of the formation energies of point defects suggest the presence of

nonnegligible association between $La^{\cdot}_{Ca}$ and $Cl^{'}_{i}$, which enhances the energy barrier for chloride ion migration, compared with that without defect association. As presented in this study, an open borate framework built with rigid covalent B–O bonds can be a useful tool for rationally designing 0D–3D chloride-ion conduction paths based on its structural dimensionality, which will contribute not only to understanding of the chloride-ion transport phenomena but also to improving the poor variety of chloride-ion conduction. In addition, it has significant advantages in terms of low environmental impact and abundant resources. The chloride-ion conductivity of the present compound is lower than those of previously reported perovskite chlorides and doped $PbCl_2$, however, further exploration using a rich variety of open borate frameworks could contribute to the realization of safe, low-temperature-driven fast chloride-ion conducting solid electrolytes with thermal and chemical stability for all-solid-state chloride ion batteries.

Reference in Chapter 3

(1) Lei, B.; Bai, S.; Ju, S.; Yin, C.; Chen, C.; Zhang, J. Review on Advances in Thermoelectric Conversion Using Ion-Conducting Polymers. *Mater. Res. Express*. **2021**, *8*(6), 062001.

(2) Yamazoe, N.; Miura, N. Gas Sensors Using Solid Electrolytes. *MRS Bulletin*. **1999**, *24*(6), 37-43.

(3) Famprikis, T.; Canepa, P.; Dawson, J. A.; Islam, M. S.; Masquelier, C. Fundamentals of Inorganic Solid-State Electrolytes for Batteries. *Nature Materials*. **2019**, *18*, 1278–1291.

(4) Nestler, T.; Schmid, R.; Münchgesang, W.; Bazhenov, V.; Schilm, J.; Leisegang, T.; Meyer, D.C. Separators - Technology Review: Ceramic based Separators for Secondary Batteries. *AIP Conf Proc*. **2014**, *1597*, 155–184.

(5) Nestler, T.; Roedern, R.; Uvarov, N. F.; Hanzi, J.; Elia, A. G.; Vivanco, M.D. Separators and electrolytes for rechargeable batteries: Fundamentals and perspectives. *Phys Sci Rev*. **2018**, *4*, 0155.

(6) Ueda, M.; Imasawa, K.; Konda, S.; Sasaki, T.; Ishikawa, T.; Ohtsuka, T. Improvement of Chlorine Electrode in Al-Cl_2 Cell in NaCl-KCl Melt by Rotation. *Electrochemistry*. **1999**, *67*(6), 695–699.

(7) Singhal, S. C. Advances in Solid Oxide Fuel Cell Technology. *Solid State Ionics*. **2000**, *135*, 305-313.

(8) Fertig, M. P.; Skadell, K.; Schulz, M.; Dirksen, C.; Adelhelm, P.; Stelter, M. From High- to Low-Temperature: The Revival of Sodium-Beta Alumina for Sodium Solid-State Batteries. *Batteries and Supercaps*. **2022**, *5*, e20210013.

(9) Kong, S. T.; Deiseroth, H. J.; Maier, J.; Nickel, V.; Weichert, K.; Reiner, C. Li_6PO_5Br and Li_6PO_5Cl: The First Lithium-Oxide-Argyrodites. *Z Anorg Allg Chem* **2010**, *636* (11), 1920–1924.

(10) Murin, I. V.; Glumov, O. V.; Mel'Nikova, N. A. Solid Electrolytes with Predominant Chloride Conductivity. *Russian Journal of Electrochemistry*. **2009**, *45*, 411–416.

(11) Wu, B.; Luxa, J.; Šturala, J.; Wei, S.; Děkanovský, L.; Parameswaran, A. K.; Li, M.; Sofer, Z. A Room-Temperature Chloride-Conducting Metal–Organic Crystal $[Al(DMSO)_6]Cl_3$ for Potential Solid-State Chloride-Shuttle Batteries. *Energy Environ. Mater*. **2024**, *7* (1), e12530.

(12) Gschwind, F.; Euchner, H.; Rodriguez-Garcia, G. Chloride Ion Battery Review: Theoretical Calculations, State of the Art, Safety, Toxicity, and an Outlook towards Future Developments. *Eur. J. Inorg. Chem*. **2017**, *21*, 2784–2799.

(13) Sakamoto, R.; Shirai, N.; Inoishi, A.; Okada, S. All-Solid-State Chloride-Ion Battery with Inorganic Solid Electrolyte. *ChemElectroChem*. **2021**, *8* (23), 4441–4444.

(14) Murin, I. V.; Glumov, O. V.; Mel'Nikova, N. A. Solid Electrolytes with Predominant Chloride Conductivity. *Russian Journal of Electrochemistry*. **2009**, *45*, 411–416.

(15) Hoshibo, H.; Yamazaki, M.; Nakamura, Y.; Shimoji, M. Ionic Conductivity of Lead Chloride Crystals. *J. Phys. Cos. Jpn*. **1969**, *26*(6), 1422–1426.

(16) Mizusaki, J.; Arai, K.; Fueki, K. Ionic Conduction of The Perovskite-Type Halides. *Solid State Ionics*. **1983**, *11*, 203–211.

(17) Derrington, C. E.; Lindner, A.; O'keeffe, M. Ionic Conductivity of Some Alkaline Earth Halides. Journal of Solid State Chemistry. **1975**, *15*, 171–174.

(18) Choudhuri, S. P.; Bichile, G. K. The Electrical Conductivity and Dielectric Behaviour of Polycrystalline Calcium Fluoride. *Solid State Communications*. **1987**, *64*(6), 993–995.

(19) Xia, T.; Li, Q.; Zhao, X.; Shen, X. Bismuth and Chlorine Dual-Doped Perovskite Chloride as a Phase-Structure-Stable and Moisture-Resistant Solid Electrolyte for Chloride Ion Batteries. *Adv. Mater*. **2024**, *36* (4), 2310565.

(20) Panja, S.; Miao, Y.; Döhn, J.; Choi, J.; Fleischmann, S.; Guddehalli Chandrappa, S.; Diemant, T.; Groß, A.; Karkera, G.; Fichtner, M. Synthesis, Structural Analysis, and Degradation Behavior of Potassium Tin Chloride as Chloride-Ion Batteries Conversion Electrode Material. *Adv. Funct. Mater*. **2024**, 2413489.

(21) Sakamoto, R.; Shirai, N.; Zhao, L.; Inoishi, A.; Sakaebe, H.; Okada, S. Room-Temperature Operation of All-Solid-State Chloride-Ion Battery with Perovskite-Type $CsSn_{0.95}Mn_{0.05}Cl_3$ as a Solid Electrolyte. *Electrochemistry*. **2023**, *91* (7), 077003.

(22) Verwey, J. F.; Westerink, N. G. Photoconductivity in Lead Chloride and Lead Bromide. *Physica*. **1969**, *42*, 293–302.

(23) Mizusaki, J.; Arai, K.; Fueki, K. Ionic Conduction of The Perovslite-Type Halides. *Solid State Ionics*. **1983**, *11*, 203–211.

(24) Distributed by the Office of Data and Informatics of the National Institute of Standards and Technology, Material Measurement Laboratory, *IUPAC-NIST Solubility Database, Version 1.1* NIST Standard Reference Database 106.

(25) Imanaka, N.; Okamoto, K.; Adachi, G. Y. Water-Insoluble Lanthanum Oxychloride-Based Solid Electrolytes with Ultra-High Chloride Ion Conductivity. *Angew. Chem. Int. Ed*. **2002**, *41* (20), 3890–3892.

(26) Matsumoto, H.; Miyake, T.; Iwahara, H. Chloride ion conduction in $PbCl_2$-PbO system. *Mater. Res. Bull*. **2001**, *36*, 1177–1184.

(27) Shitara, K.; Kuwabara, A.; Hibino, K.; Fujii, K.; Yashima, M.; Hester, J. R.; Umeda, M.; Nunotani, N.; Imanaka, N. Ionic Conduction Mechanism in Ca-Doped Lanthanum Oxychloride. *Dalton Transactions* **2021**, *50 (1)*, 151–156.

(28) Yaguchi, H.; Fujii, K.; Tsuchiya, Y.; Ogino, H.; Tsujimoto, Y.; Yashima, M. Ruddlesden-Popper Oxychlorides $Ba_3Y_2O_5Cl_2$, $Sr_3Sc_2O_5Cl_2$, and Sr_2ScO_3Cl: First Examples of Oxide-Ion-Conducting Oxychlorides. *ACS Appl Energy Mater*. **2022**, *5* (1), 295–304.

(29) Kluczny, M.; Song, J. T.; Akbay, T.; Niwa, E.; Takagaki, A.; Ishihara, T. Sillén-Aurivillius Phase Bismuth Niobium Oxychloride, Bi_4NbO_8Cl, as a New Oxide-Ion Conductor. *J Mater Chem A Mater*. **2022**, *10* (5), 2550–2558.

(30) Ueno, N.; Yaguchi, H.; Fujii, K.; Yashima, M. High Conductivity and Diffusion Mechanism of Oxide Ions in Triple Fluorite-Like Layers of Oxyhalides. *J Am Chem Soc*. **2024**, *146*, 11235–11244.

(31) Yaguchi, H.; Morikawa, D.; Saito, T.; Tsuda, K.; Yashima, M. High Oxide-Ion Conductivity through the Interstitial Oxygen Site in Sillén Oxychlorides. *Adv Funct Mater*. **2023**, *33* (27), 2214082.

(32) Hawthorne, F. C.; The structure hierarchy hypothesis. *Mineral. Mag*. **2018**, *78*, 957-1027.

(33) Calès, B. :; Levasseur, A.; Fouassier, C.; Réau, J. M.; Hagenmuller, P. Conductive Ionique Du Lithium Dans Les Solutions Solides De Structure Boracite $Li_{4+x}B_7O_{12+x/2}X$(X = CI, Br)($0 \leq x \leq 1$). *Solid State Communications*. **1977**, *24*, 323–325.

(34) Rousse, G.; Baptiste, B.; Lelong, G. Crystal Structures of $Li_6B_4O_9$ and $Li_3B_{11}O_{18}$ and Application of the Dimensional Reduction Formalism to Lithium Borates. *Inorg Chem*. **2014**, *53* (12), 6034–6041.

(35) Zhang, Z.; Wang, Y.; Zhang, B.; Yang, Z.; Pan, S. Polar Fluorooxoborate, NaB_4O_6F: A Promising Material for Ionic Conduction and Nonlinear Optics. *Angewandte Chemie*. **2018**, *130* (22), 6687–6691.

(36) Duchêne, L.; Lunghammer, S.; Burankova, T.; Liao, W. C.; Embs, J. P.; Copéret, C.; Wilkening, H. M. R.; Remhof, A.; Hagemann, H.; Battaglia, C. Ionic Conduction Mechanism in the $Na_2(B_{12}H_{12})_{0.5}(B_{10}H_{10})_{0.5}$ Closo-Borate Solid-State Electrolyte: Interplay of Disorder and Ion-Ion Interactions. *Chem. Mater*. **2019**, *31* (9), 3449–3460.

(37) Li, X. H.; Yang, L.; Zhu, Z. Y.; Wang, X. G.; Chen, P. Y.; Huang, S. C.; Wei, X. Y.; Cai, G. H.; Manuel, P.; Yang, S. H.; Lin, J. H.; Kuang, X. J.; Sun, J. L.; Borates as a new direction in the design of oxide ion conductors. *Sci. China Mater*. **2022**, *65*, 2737–2745.

(38) Wang, Z.; He, J.; Hu, B.; Shan, P.; Xiong, Z.; Su, R.; He, C.; Yang, X.; Long, X. $Ca_2B_5O_9Cl$ and $Sr_2B_5O_9Cl$: Nonlinear Optical Crystals with Deep-Ultraviolet Transparency Windows. *ACS Appl Mater Interfaces*. **2020**, *12* (4), 4632–4637.

(39) Dotsenko, V. P.; Berezovskaya, I. V.; Efryushina, N. P.; Shabanov, E. V.; Voloshinovskii, A. S. Luminescent Properties of Ce^{3+} Ions in $Ca_2B_5O_9Cl$. *Physica Status Solidi (A) Applications and Materials Science* **2006**, *203 (5)*, 892–897.

(40) Liang, J.; Yang, X.; Xiao, S. Enhancement on the Luminescence of $Ca_2B_5O_9Cl:Eu^{2+}$ by Co-Doping of Al^{3+} and Ba^{2+} Ions for Full Spectrum Lighting Application. *Opt Mater (Amst)* **2023**, *135*, 113269.

(41) Sheldrick, G. M. SHELXT-Integrated Space-Group and Crystal-Structure Determination. *Acta Crystallogr A* **2015**, *71*, 3-8.

(42) Hubschle, C. B.; Sheldrick, G. M.; Dittrich, B. ShelXle: a Qt graphical user interface for SHELXL. *J Appl Crystallogr* **2011**, *44*, 1281-1284.

(43) Dolomanov, O. V.; Blake, A. G.; Champness, N. R.; Schröder, M. OLEX: new software for visualization and analysis of extended crystal structures. *J Appl Crystallogr* **2003**, *36*, 1283-1284.

(45) Kumagai, Y.; Oba, F. Electrostatics-based finite-size corrections for first-principles point defect calculations. *Phys Rev B.* **2014**, *89*, 195205.

(46) Jain, A.; Ong, S. P.; Hautier, G.; Chen, W.; Richards, W. D.; Dacek, S.; Cholia, S.; Gunter, D.; Skinner, D.; Ceder, G.; Persson, K. A. Commentary: The Materials Project: A Materials Genome Approach to Accelerating Materials Innovation. *APL Materials. American Institute of Physics Inc*. **2013**, *1*, 011002.

(47) Kresse, G.; Joubert, D. From ultrasoft pseudopotentials to the projector augmented-wave method. *Phys Rev B.* **1999**, *59*, 1758–1775.

(48) Kresse, G.; Furthmüller, J. Efficient iterative schemes for *ab initio* total-energy calculations using a plane-wave basis set. *Phys Rev B.* **1996**, *54*, 11169–11186.

(49) Kresse, G.; Furthmüller, J. Efficiency of ab-initio total energy calculations for metals and semiconductors using a plane-wave basis set. *Comput Mater Sci*, **1996**, *6*, 15–50.

(50) Kresse, G.; Furthmüller, J. *Ab initio* molecular dynamics for liquid metals. *Phys Rev B Condens Matter*, **1993**, *47*, 558–561.

(51) Perdew, J. P.; Ruzsinszky, A.; Csonka, G. I.; Vydrov, O. A.; Scuseria, G. E.; Constantin, L. A.; Zhou, X.; Burke, K. Restoring the Density-Gradient Expansion for Exchange in Solids and Surfaces. *Phys Rev Lett* **2008**, 100 (13).

(52) Henkelman, G.; Jónsson, H. Improved Tangent Estimate in the Nudged Elastic Band Method for Finding Minimum Energy Paths and Saddle Points. *Journal of Chemical Physics* **2000**, 113, 9978–9985.

(53) Henkelman, G.; Uberuaga, B. P.; Jónsson, H. Climbing Image Nudged Elastic Band Method for Finding Saddle Points and Minimum Energy Paths., *J Chem Phys*, **2000**, 113, 9901–9904.

Chapter 4 $(La_{1-x}M_x)(BO_2)_2Cl_{1-x}$ (M = Ca, Sr, x = 0–0.15): A new open-framework layered borate chloride

4.1 Introduction

Chlorine is the second most abundant halogen after fluorine and is widely found in various chloride minerals,[1–3] the presence of large quantities of raw materials makes the study of chlorine valuable. Studies on inorganic chloride-ion conductors, especially for simple binary and ternary chlorides, have been continuously investigated over the last century, compounds such as $PbCl_2$, $Cs(Sn/Pb)Cl_3$ and others achieve high ionic conductivities via cation substitution even near room temperature.[4–12] However, low melting points and poor thermal and chemical stability limit their practical application.[13–15] Compared to simple chloride, a layered mixed-anion compound $La_{1-x}Ca_xOCl_{1-x}$ ($0 \leq x \leq 0.2$) with a tetragonal matlockite-type structure possesses great structural stability against humidity and high temperature.[16] This provides ideas for the design of chloride-ion conductors. As presented in chapter 3, the open borate framework built with rigid covalent B–O bonds can be a useful tool for rationally designing 0D–3D chloride-ion conduction paths based on its structural dimensionality.[17] Ions are significantly bigger than electrons, and in order for ions to move macroscopically, they must have a migration path that is appropriate for their size. Of course there are many factors involved in the migration of ions, but structurally, the ease of migration of ions is ranked according to 3D > 2D > 1D.[18–23]

In chemistry, a group is a column of elements in the Periodic Table. Elements in the same group have similar valence electron structures and exhibit progressively differing physical and chemical properties from top to bottom. [24,25] In fact, using a homologous element instead of one of the components of a compound is an effective way to expand its family. For example, $Ca_2B_5O_9Cl$, the base material discussed in Chapter 3, is reported to exhibit nonlinear

optical properties together with $Sr_2B_5O_9Cl$,[26] Cs(Sn/Pb)Cl_3 and others simple metal compounds have also been reported. However, replacing an element does not necessarily yield the same performance. As we previously introduced, in many studies on LaOCl, the introduction of Ca^{2+} considerably enhanced the Cl^-ion conductivity but the Mg^{2+} doping did not demonstrate as impressive an increase of Cl^- ion conductivity. [16, 27–30] One possible reason is the difference of the structural environment, but the exact reason remains unclear. However, it's still an effective method to expand exploration.

In order to explore more chloride ion conductors with borate open frameworks, in this chapter, we synthesized $(La_{1-x}M_x)(BO_2)_2Cl_{1-x}$ (M = Ca, Sr, x = 0–0.15) which show a two-dimensional (2D) chloride layers structure and exhibits complete insolubility. Single-crystal structure analysis revealed each Cl^- ion forms a triangular cone in the *ac* plane with the La^{3+} ions with the Cl^- ion at the apex, $(B_2O_4)^{2-}$ borate framework forms a one-dimensional chain along *a* direction and connects to La^{3+} ions on both sides, by doping Ca^{2+} or Sr^{2+} to substitute La^{3+} sites, it shows a decreased concentration of Cl^- ions. These solutions exhibit the highest conductivity of 1.84×10^{-4} S cm^{-1} at 700 °C when M = Ca and x = 0.10, and 7.59×10^{-4} S cm^{-1} at 700 °C when M = Sr and x = 0.15, respectively. The predominant chloride-ion conduction can be hypothesized to be diffusion through vacancies at chloride sites, suggesting that this is a promising material.

4.2 Experimental details of Chapter 4

Reagents. B_2O_3 (Sigma-Aldrich, 99.98%), $LaCl_3$ (High Purity Chemicals, 99.9%) $CaCl_2$ (Wako Pure Chemical Industries, 95.0%), $SrCl_2$ (Rare Metallic, 99.9%) powders were used as received. La_2O_3 (Rare Metallic, 99.99%) was heated overnight in a dry oven at 1000°C prior use. All raw materials were stored in an Ar-filled glovebox (moisture and oxygen levels less than 0.1 ppm).

Crystal Growth. Single crystals of $La(BO_2)_2Cl$, $(La_{0.82}Ca_{0.18})(BO_2)_2Cl_{0.82}$ and $(La_{0.8}Sr_{0.2})(BO_2)_2Cl_{0.8}$ were obtained by the flux growth method using a B_2O_3 molten salt. 3.0 mmol of La_2O_3, 3.0 mmol of $LaCl_3$, and 1g of B_2O_3 for the undoped sample and 3.0 mmol of La_2O_3, 2.1 mmol of $LaCl_3$, 0.9 mmol of $(Ca/Sr)Cl_2$, and 1g B_2O_3 for the (Ca/Sr)-doped sample were thoroughly mixed, loaded into a silica tube with a diameter of 11 mm, and flame-sealed under a vacuum level of 1 Pa. The starting materials were heated in a muffle furnace to 950°C within 12h and held for 24h, cooled to 580°C at 2°C/h, and finally naturally cooled to room temperature by turning off the heater. The products were then washed with sonicated water and extracted from the flux. Colorless transparent needle-shaped crystals of $La(BO_2)_2Cl$, $(La_{0.82}Ca_{0.18})(BO_2)_2Cl_{0.82}$ and $(La_{0.8}Sr_{0.2})(BO_2)_2Cl_{0.8}$ were collected by vacuum filtration, respectively.

Solid State Reaction. Polycrystalline powder samples of $(La_{1-x}M_x)(BO_2)_2Cl_{1-x}$ (M = Ca, Sr, x = 0, 0.05, 0.10, 0.125, 0.15, 0.20) were synthesized from a stoichiometric mixture of B_2O_3, La_2O_3, $LaCl_3$, and $(Ca/Sr)Cl_2$. The mixture was ground thoroughly with an agate mortar and pestle, pelletized by pressing at 8 kN into a pellet with a diameter of 6.9 mm, flame-sealed under a vacuum level of 1 Pa, and then heated in a muffle furnace at 900°C for 24h and cooled to room temperature for 6h. After the reaction was completed, the pellet was ground and pressing at 8 kN into a pellet again with a diameter of 6.9 mm to ensure more complete reaction of the raw materials. It was then sintered a second time under the same conditions.

Elemental Analysis. Elemental analysis on the single crystals of undoped and (Ca/Sr)-doped $La(BO_2)_2Cl$ was carried out using a scanning electron microscope (SEM, HITACHI-TM3000) equipped with an energy dispersive X-ray (EDX) spectrometer (Oxford Instruments, Swift ED3000). The accelerating voltage was 15 keV.

Single-Crystal Structure Determination. Single crystal X-ray diffraction (SCXRD) data of undoped and (Ca/Sr)-doped $La(BO_2)_2Cl$ that were obtained by flux method were

collected at room temperature using a Rigaku XtaLab mini II diffractometer (Mo *K*a radiation). The data collection covered 99% of the reciprocal space to $2\theta_{max}$ = 60.9° with R_{int} = 5.64% (undoped phase), 5.50% (Ca-doped phase) and 5.34% (Sr-doped phase) after absorption correction. The crystal structures were solved by a dual-space algorithm method (SHELXT)[31] and refined by a full-matrix least-squares method with SHELXL[32], using an Olex2 graphical user interface.[33]

Laboratory X-ray Powder Diffraction. Powder X-ray diffraction (PXRD) measurements of $(La_{1-x}M_x)(BO_2)_2Cl_{1-x}$ (M = Ca, Sr, x = 0, 0.05, 0.10, 0.125, 0.15, 0.20) powder samples were performed using a Rigaku MiniFlex600 diffractometer (Cu *K*α radiation) in the 2θ range from 5° to 60° at room temperature.

Thermal Gravimetric Analysis. Thermogravimetric analysis (TGA) of $(La_{0.9}Ca_{0.1})(BO_2)_2Cl_{0.9}$ and $(La_{0.85}Sr_{0.15})(BO_2)_2Cl_{0.85}$ powder samples were performed using a Rigaku TG-DTA8188 system under flowing N_2 and O_2 atmosphere (1.0 L/min). The sample was loaded in an platinum crucible and heated up to 700°C at 10°C/min.

EIS Measurements. $(La_{1-x}M_x)(BO_2)_2Cl_{1-x}$ (M = Ca, Sr, x = 0, 0.05, 0.10, 0.125, 0.15) powder samples were pelletized by pressing at 100 kN with diameter and thickness of 10 mm and 1 mm, respectively, followed by a second sintering with the same heating conditions. These obtained pellets were polished with waterproof abrasive papers until they were less than 0.6 mm thick. Formation of a gold sputtering layer in the center of the pellet surface using an ion coater (IB-3, Eiko), and then a gold paste was fixed on the sputtered layer. AC EIS of the pellets was measured using the complex impedance method (1260 impedance analyzer, Solartron) at 300 mV in the frequency range between 1 Hz and 10 MHz, starting at 400°C and testing at 100°C intervals up to 700°C in an Ar gas atmosphere. The Nyquist plot was fitted by using an equivalent circuit model composed of inductance from the electrical wire and equipment (L_0),

a total resistance (R_{total}), its constant phase element (CPE_{total}), an electrode-electrolyte interface resistance (R_i), and its constant phase element (CPE_i). The AC conductivity (σ_{ac}) was estimated from the total resistance. In order to investigate polarization behavior, dc conductivity (σ_{dc}) was calculated as a function of time at 700°C in an Ar gas atmosphere by applying a DC voltage of 300 mV using a DC voltage/current generator (R6144, Advantest) and an electrometer (R8240, Advantest).

4.3 Results and discussion

4.3.1 Crystal Structure.

Colourless transparent needle single crystals of $La(BO_2)_2Cl$ were grown by the self-flux method using a B_2O_3 molten salt and extracted by washing the products with water. The photo is shown in Figure 4.1.

Figure 4.1 Photograph of single crystals of undoped $La(BO_2)_2Cl$ on a 1mm-grid paper. The single crystals grew preferentially along the crystallographic *b*-axis.

The crystal structure of $La(BO_2)_2Cl$, determined by single-crystal structure analysis at room temperature, is shown in Figure 4.2. The borate chloride crystallizes in a triclinic cell

(space group *P* -1) with cell parameters *a* = 4.2536(2) Å, *b* = 6.6355(3) Å, *c* = 8.2169(4) Å, *α* = 82.041(4) °, *β* = 89.241(4) °, *γ* = 72.145(5) ° and V = 218.518(19) Å^3. The crystallographic data including the atomic coordinates (Table 4.1, Table 4.2, and Table 4.3) are consistent with previous reports.[34] The nearest neighbor (NN) distance between Cl^- ions in *ab* plane is 3.458(4) Å, similar with $PbCl_2$ (3.413(6) Å) and LaOCl (3.416(3) Å),[35,36] therefore, the migration of Cl^- ions can be induced by introducing ionic vacancies. Boron and oxygen atoms are formed as BO_3 units and form a double triangle by co-pointing, which extends along the *a* axis and connected La atoms by covalent bonds, this raises the migration barriers for O^{2-} ions significantly.

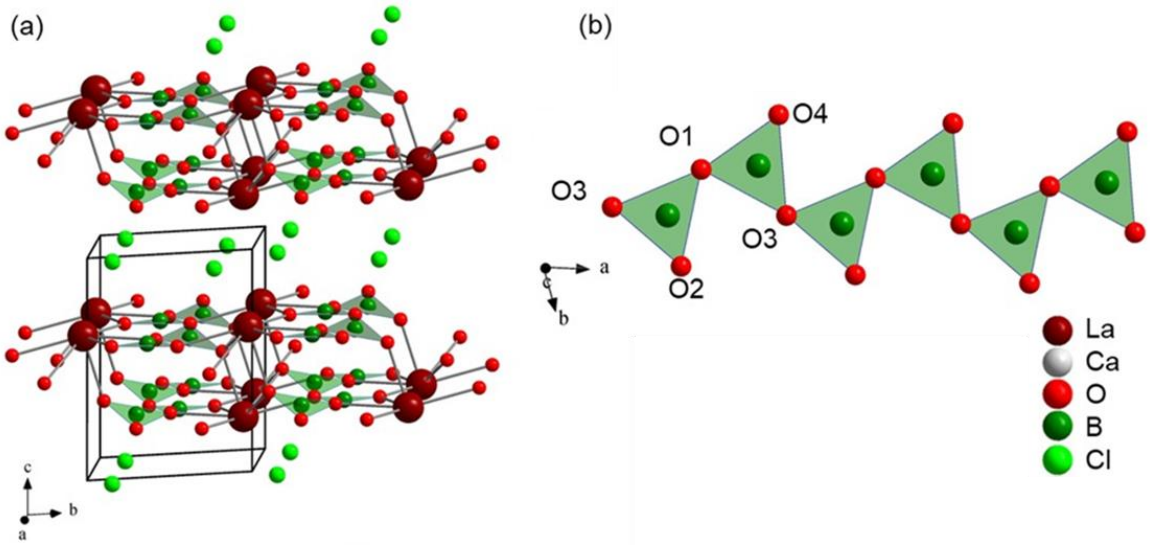

Figure 4.2 (a) Crystal structures of $La(BO_2)_2Cl$. (b) $(BO_2)_2^{2-}$ units extends along the *a* direction.

In order to verify the structure after the introduction of ionic vacancies, (Ca/Sr)-doped $La(BO_2)_2Cl$ single crystals was synthesized in the similar conditions by use the $(Ca/Sr)Cl_2$ as a Ca/Sr source with an atomic ratio of La/(Ca/Sr) = 8/2. The doped crystals have the same morphology as the undoped crystals, but the size is an order of magnitude smaller which may

be due to the deterioration of crystallinity by the introduction of ionic vacancies. The photo is shown in Figure 4.3.

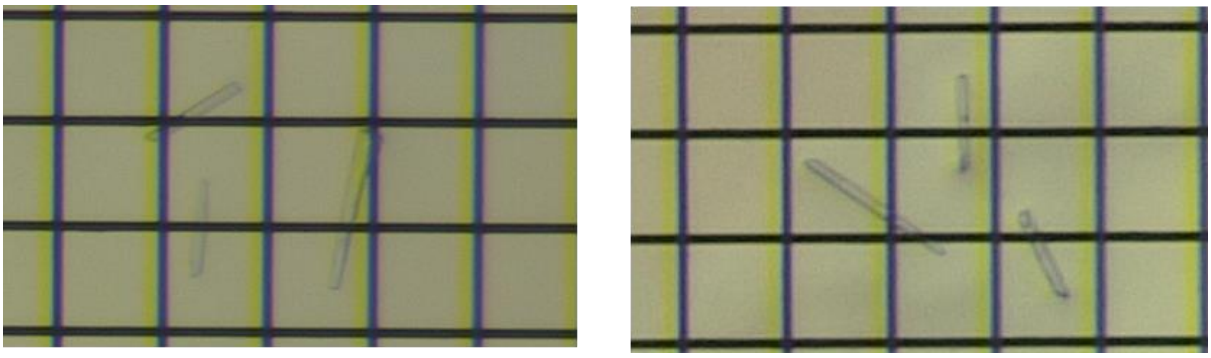

Figure 4.3 Photographs of single crystals of Ca-doped (left, on a 0.1mm-grid paper) and Sr-doped (right, on a 0.1mm-grid paper) $La(BO_2)_2Cl$. The single crystals grew preferentially along the crystallographic *b*-axis.

The crystal structure of (Ca/Sr)-doped $La(BO_2)_2Cl$, determined by single-crystal structure analysis at room temperature, is shown in Figure 4.4. After doping, SEM-EDX elemental analysis estimated the atomic ratio of La:Ca to be 0.82:0.16 and La:Sr to be 0.79:0.20, that is, approximately 16% substitution of La for Ca, and 20% substitution of La for Sr, respectively (Figure 4.5). The cell volume was also found to decrease by 0.36% for Ca doping (a = 4.2462(2) Å, b = 6.6321(2) Å, c = 8.2094(3) Å, α = 82.055(3) °, β = 89.230(3) °, γ = 72.055(3) ° and V = 217.725(15) $Å^3$) and 0.25% for Sr doping (a = 4.2499(3) Å, b = 6.6317(5) Å, c = 8.2099(6) Å, α = 82.097(7) °, β = 89.267(6) °, γ = 72.089(7) ° and V = 217.98(3) $Å^3$). Cl^- ion sites show vacancies and the atomic occupancy decreases to 0.82/0.80 for Ca/ Sr doping, the final refined chemical compositions were $(La_{0.82}Ca_{0.18})(BO_2)_2Cl_{0.82}$ and $(La_{0.8}Sr_{0.2})(BO_2)_2Cl_{0.8}$. The final refined crystallographic data are shown in Table 4.1, Table 4.4, Table 4.5, Table 4.6, and Table 4.7.

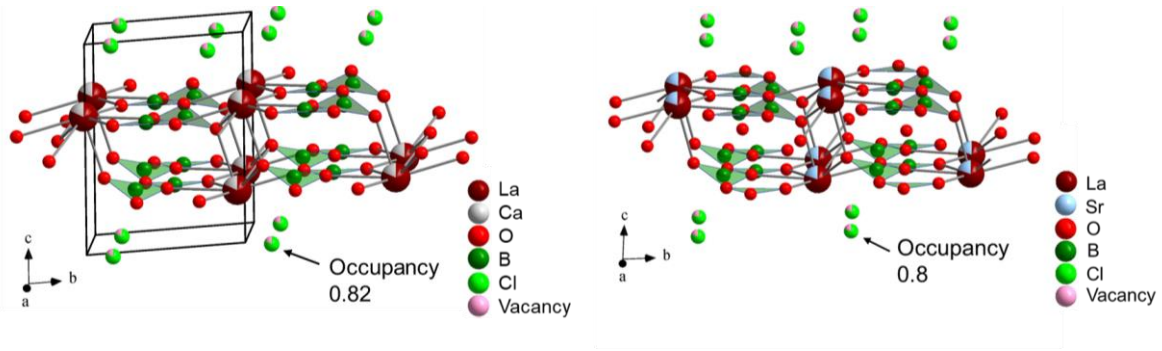

Figure 4.4 (a) Crystal structures of $(La_{0.82}Ca_{0.18})(BO_2)_2Cl_{0.82}$ by Ca^{2+} doping, Cl^- ion sites show vacancies and the atomic occupancy decreases to 0.82. (b) Crystal structures of $(La_{0.8}Sr_{0.2})(BO_2)_2Cl_{0.8}$ by Sr^{2+} doping, Cl^- ion sites show vacancies and the atomic occupancy decreases to 0.80.

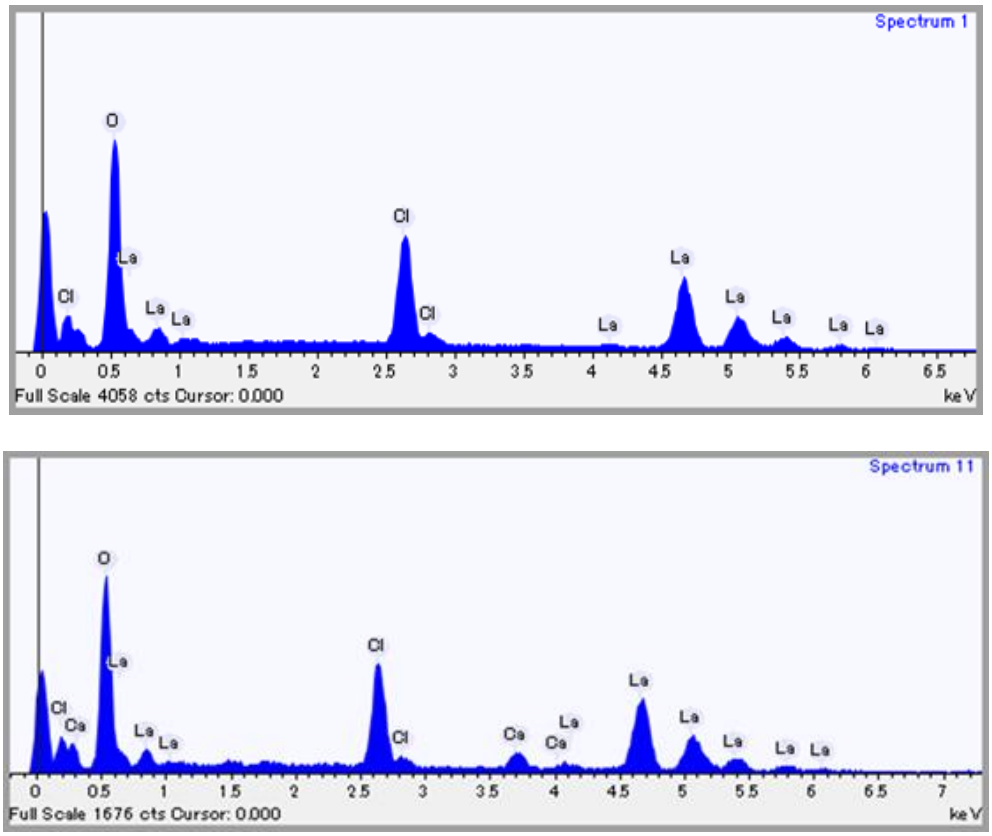

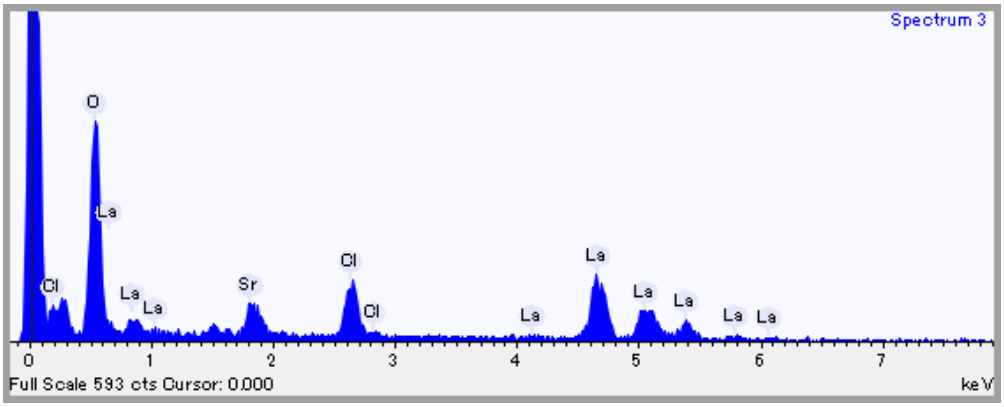

Figure 4.5 EDX spectra of undoped (upper panel), Ca-doped (middle panel) and Sr-doped (lower panel) $La(BO_2)_2Cl$. The EDX analysis indicates that the molar ratio of La/Cl/(Ca/Sr) is 1.0/1.1/0, 0.82/0.82/0.16 and 0.79/0.76/0.20, which are consistent with the results of single-crystal structure analysis.

Table 4.1 Results of Structure Refinement of undoped and (Ca/Sr)-doped $La(BO_2)_2Cl$ Using Single-Crystal XRD Data.

Formula	$La(BO_2)_2Cl$	$(La_{0.82}Ca_{0.18})(BO_2)_2Cl_{0.82}$	$La_{0.8}Sr_{0.2}(BO_2)_2Cl_{0.8}$
Formula weight	259.98	235.81	242.63
Radiation	Mo *K*α (λ=0.71073 Å)	Mo *K*α (λ=0.71073 Å)	Mo *K*α (λ=0.71073 Å)
***T* (K)**	293	293	293
Crystal system	Triclinic	Triclinic	Triclinic
Space group	*P* -1	*P* -1	*P* -1
***a* (Å)**	4.2536(2)	4.2462(2)	4.2499(3)
***b* (Å)**	6.6355(3)	6.6321(2)	6.6317(5)
***c* (Å)**	8.2169(4)	8.2094(3)	8.2099(6)
***α* (°)**	82.041(4)	82.055(3)	82.097(7)
***β* (°)**	89.241(4)	89.230(3)	89.267(6)
***γ* (°)**	72.145(5)	72.055(3)	72.089(7)
***V* (Å^3)**	218.518(19)	217.725(15)	217.98(3)
Z	2	2	2
***D*$_{calc}$ (g/cm^3)**	3.951	3.597	3.697

F_{000}	232	213	218
no. of measured reflns	2080	2824	3322
no. of unique reflns	884	1229	1249
no. of observed reflns ($F^2 > 2\sigma(F^2)$)	884	1229	1249
R_{int} **(%)**	1.86	2.72	5.34
$R[F^2 > 2\sigma(F^2)]/wR(F^2)$ **(%)**	2.03/5.30	2.80/5.50	5.05/9.09
GoF	1.089	1.065	1.055

Table 4.2 Refined Structural Parameters for the Single Crystal of $La(BO_2)_2Cl$.

atom	site	*x*	*y*	*z*	SOF[1]	U_{iso}/Å^2×10^2
La	2i	0.28484(5)	0.96890(3)	0.27739(3)	1	0.879(12)
B1	2i	0.9378(11)	0.4373(7)	0.6935(6)	1	0.81(9)
B2	2i	0.3352(11)	0.6498(7)	0.6469(6)	1	1.01(9)
O1	2i	0.6001(7)	0.4637(4)	0.6763(4)	1	1.16(6)
O2	2i	1.0215(7)	0.6258(4)	0.6815(4)	1	1.34(6)
O3	2i	0.3377(7)	0.8460(4)	0.5805(4)	1	1.10(6)
O4	2i	1.1345(7)	0.2370(4)	0.7088(4)	1	1.21(6)
Cl	2i	0.3527(3)	0.79651(17)	0.95756(13)	1	1.67(2)

[1] SOF stands for site occupancy factor.

Table 4.3 Anisotropic Displacement Parameters U_{ij} (Å^2) for $La(BO_2)_2Cl$.

atom	U_{11}	U_{22}	U_{33}	U_{23}	U_{13}	U_{12}
La	0.00767(16)	0.00629(16)	0.01313(17)	-0.00129(10)	-0.00027(10)	-0.00322(10)
B1	0.009(2)	0.008(2)	0.010(2)	-0.0015(16)	0.0003(17)	-0.0064(16)
B2	0.006(2)	0.010(2)	0.018(3)	-0.0059(18)	0.0016(18)	-0.0062(17)
O1	0.0068(13)	0.0081(13)	0.0211(17)	-0.0019(12)	-0.0003(12)	-0.0042(11)
O2	0.0134(15)	0.0073(13)	0.0125(15)	0.0002(11)	-0.0023(12)	-0.0039(11)
O3	0.0068(13)	0.0077(14)	0.0273(18)	-0.0026(12)	-0.0002(12)	-0.0042(11)

O4	0.0089(14)	0.0076(14)	0.0202(17)	-0.0028(12)	-0.0004(12)	-0.0029(11)
Cl	0.0232(5)	0.0141(5)	0.0149(6)	-0.0024(4)	0.0016(4)	-0.0086(4)

Table 4.4 Refined Structural Parameters for the Single Crystal of $(La_{0.82}Ca_{0.18})(BO_2)_2Cl_{0.82}$.

atom	**site**	***x***	***y***	***z***	**SOF[1]**	U_{iso}/Å^2×10^2
La	2i	0.28475(7)	0.96887(5)	0.27741(4)	0.818(6)	0.00656(11)
Ca	2i	0.28475(7)	0.96887(5)	0.27741(4)	0.182(6)	0.00656(11)
B1	2i	0.9377(14)	0.4373(9)	0.6935(7)	1	0.0143(11)
B2	2i	0.3340(14)	0.6507(9)	0.6470(7)	1	0.0161(12)
O1	2i	0.5986(8)	0.4655(6)	0.6765(5)	1	0.0175(8)
O2	2i	1.0214(8)	0.6255(5)	0.6814(5)	1	0.0192(8)
O3	2i	0.3384(8)	0.8463(5)	0.5807(4)	1	0.0171(8)
O4	2i	1.1349(8)	0.2373(6)	0.7085(5)	1	0.0196(8)
Cl	2i	0.3531(3)	0.7967(2)	0.95714(16)	0.819	0.0112(3)

[1] SOF stands for site occupancy factor.

Table 4.5 Anisotropic Displacement Parameters U_{ij} (Å^2) for $(La_{0.82}Ca_{0.18})(BO_2)_2Cl_{0.82}$.

atom	U_{11}	U_{22}	U_{33}	U_{23}	U_{13}	U_{12}
La	0.00543(15)	0.00573(15)	0.00838(16)	-0.00056(10)	-0.00067(9)	-0.00167(10)
Ca	0.00543(15)	0.00573(15)	0.00838(16)	-0.00056(10)	-0.00067(9)	-0.00167(10)
B1	0.015(3)	0.013(3)	0.014(3)	-0.001(2)	0.002(2)	-0.004(2)
B2	0.012(3)	0.017(3)	0.020(3)	-0.005(2)	-0.001(2)	-0.004(2)
O1	0.0117(17)	0.0151(18)	0.024(2)	0.0003(15)	-0.0024(14)	-0.0030(14)
O2	0.0141(18)	0.0126(18)	0.030(2)	-0.0003(16)	-0.0010(15)	-0.0041(14)
O3	0.0185(18)	0.0141(18)	0.0180(19)	0.0004(14)	-0.0025(15)	-0.0053(14)
O4	0.0146(18)	0.0140(18)	0.029(2)	-0.0024(16)	0.0023(15)	-0.0037(14)
Cl	0.0174(7)	0.0103(7)	0.0074(6)	-0.0016(5)	0.0005(5)	-0.0063(5)

Table 4.6 Refined Structural Parameters for the Single Crystal of $La_{0.8}Sr_{0.2}(BO_2)_2Cl_{0.8}$.

atom	site	*x*	*y*	*z*	SOF[1]	U_{iso}/Å^2×10^2
La	2i	0.71522(14)	0.03123(8)	0.72258(8)	0.8	0.914(16)
Sr	2i	0.71522(14)	0.03123(8)	0.72258(8)	0.2	0.914(16)
B1	2i	1.062(2)	0.5628(16)	0.3072(14)	1	1.5(2)
B2	2i	0.667(3)	0.3513(15)	0.3526(15)	1	1.6(2)
O1	2i	0.9752(15)	0.3748(9)	0.3185(9)	1	1.78(15)
O2	2i	0.4015(14)	0.5354(9)	0.3242(8)	1	1.45(14)
O3	2i	0.6620(14)	0.1534(9)	0.4195(9)	1	1.81(15)
O4	2i	0.8641(15)	0.7625(9)	0.2920(9)	1	2.05(16)
Cl	2i	0.6469(6)	0.2031(4)	0.0428(3)	0.8	0.90(5)

[1] SOF stands for site occupancy factor.

Table 4.7 Anisotropic Displacement Parameters U_{ij} (Å^2) for $La_{0.8}Sr_{0.2}(BO_2)_2Cl_{0.8}$.

atom	U_{11}	U_{22}	U_{33}	U_{23}	U_{13}	U_{12}
La	0.0057(2)	0.0051(2)	0.0155(3)	-0.00134(19)	0.00023(18)	-0.00026(16)
Sr	0.0057(2)	0.0051(2)	0.0155(3)	-0.00134(19)	0.00023(18)	-0.00026(16)
B1	0.011(5)	0.013(4)	0.021(6)	-0.003(4)	-0.001(4)	-0.004(4)
B2	0.009(5)	0.007(4)	0.028(7)	-0.001(4)	-0.003(4)	0.003(3)
O1	0.009(3)	0.010(3)	0.032(5)	-0.002(3)	-0.002(3)	-0.002(2)
O2	0.006(3)	0.012(3)	0.024(4)	-0.002(3)	0.002(3)	-0.001(2)
O3	0.013(3)	0.013(3)	0.026(4)	-0.003(3)	-0.001(3)	-0.001(2)
O4	0.013(3)	0.013(3)	0.036(5)	-0.004(3)	0.004(3)	-0.005(2)
Cl	0.0125(12)	0.0055(10)	0.0093(14)	-0.0014(9)	0.0011(10)	-0.0031(9)

4.3.2 Polycrystalline samples of $(La_{1-x}M_x)(BO_2)_2Cl_{1-x}$ (M = Ca, Sr, x = 0–0.20) solid solutions

From the chloride site vacancies observed by the single-crystal structure analysis, we can expect Cl^- ion conduction, To investigate the possible chloride ion conductivity and carrier concentration dependence, polycrystalline samples of $(La_{1-x}M_x)(BO_2)_2Cl_{1-x}$ (M = Ca, Sr, x = 0–0.20) solid solutions were synthesized using a conventional solid-state reaction. Figure 4.6 shows the room temperature PXRD patterns of the Ca-doped $La(BO_2)_2Cl$ along with the data for the undoped phase. All solid solutions could be obtained as the main phase, but several tiny peaks assigned to $LaBO_3$ were detected, suggesting deviation from the nominal chemical compositions. The cell volume decreased monotonically with an increase in $x \leq 0.10$; however, it remained almost unchanged at $0.125 \leq x$. It is likely that the solid solubility limit was between 0.10 and 0.125.

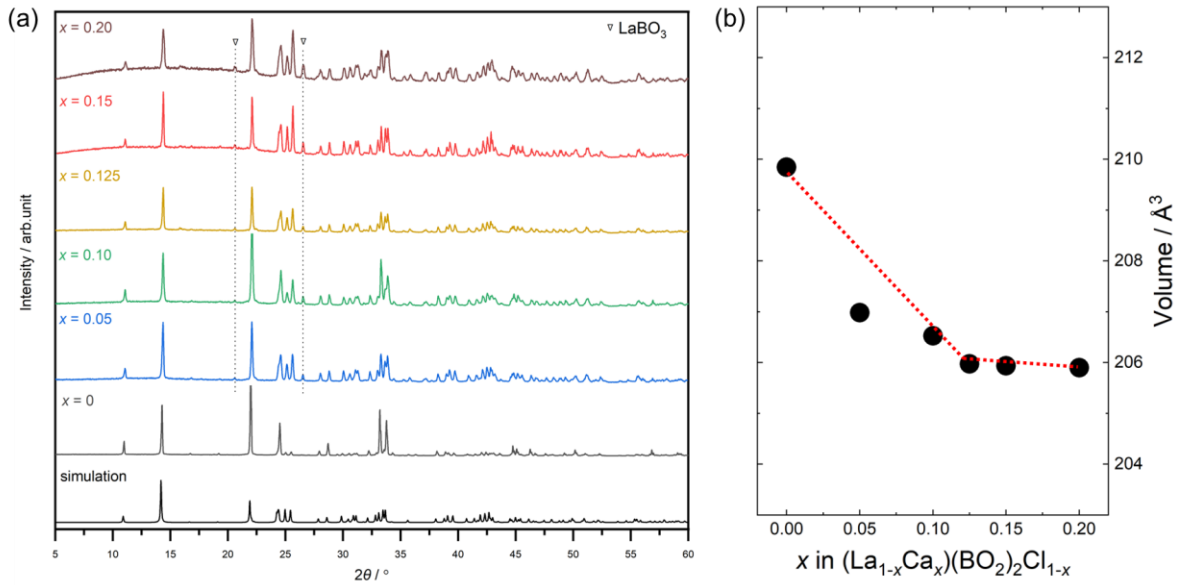

Figure 4.6 (a) Powder X-ray diffraction patterns of $(La_{1-x}Ca_x)(BO_2)_2Cl_{1-x}$ (x = 0–0.20) solid solutions measured at room temperature. (b) The cell volume as a function of x in $(La_{1-x}Ca_x)(BO_2)_2Cl_{1-x}$. The red curve is a guide to the eyes.

Figure 4.7 shows the room temperature PXRD patterns of the Sr-doped $La(BO_2)_2Cl$ along with the data for the undoped phase. When $x \leq 0$–0.15, all solid solutions could be obtained as the main phase, but several tiny peaks assigned to La_2O_3, $LaBO_3$ and $La(BO_2)_3$ were detected, suggesting deviation from the nominal chemical compositions. When $x = 0.20$, The peaks from $La(BO_2)_3$ became unnoticeable and thus the sample was not used for subsequent measurements. The cell volume decreased monotonically as x increased up to 0.15; however, when $x = 0.20$, the cell volume appears to increase. This may be due to the ionic radius of Sr^{2+} ion is larger than that of La^{3+} ion, and the volume effect from the vacancy of Cl ions dominates when $x \leq 0.15$, the volume effect from the introduction of Sr ions dominates when x is larger than 0.15.

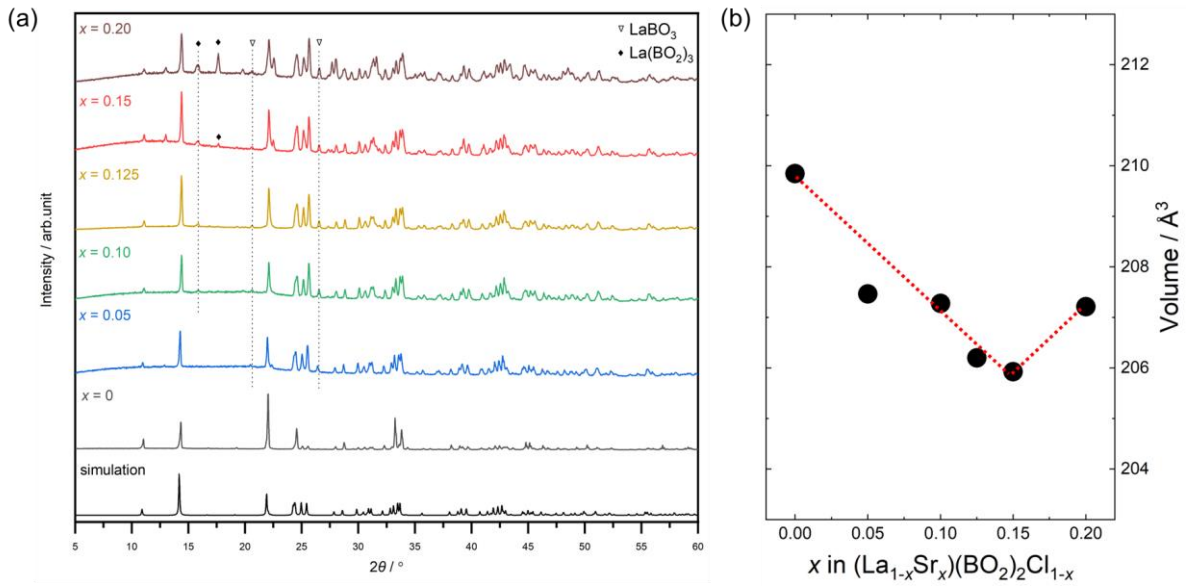

Figure 4.7 (a) Powder X-ray diffraction patterns of $(La_{1-x}Sr_x)(BO_2)_2Cl_{1-x}$ (x = 0–0.20) solid solutions measured at room temperature. (b) The cell volume as a function of x in $(La_{1-x}Sr_x)(BO_2)_2Cl_{1-x}$ (x = 0–0.15). The red curve is a guide to the eyes.

4.3.3 Humidity and thermal stability

(Ca/Sr)-doped $La(BO_2)_2Cl$ exhibit excellent humidity and thermal stability, polycrystalline samples PXRD measurements were conducted for $x = 0.1$ after the preparation of polycrystalline samples, which were then placed in an atmospheric environment. After several days, none of the PXRD results changed (Figure 4.8).

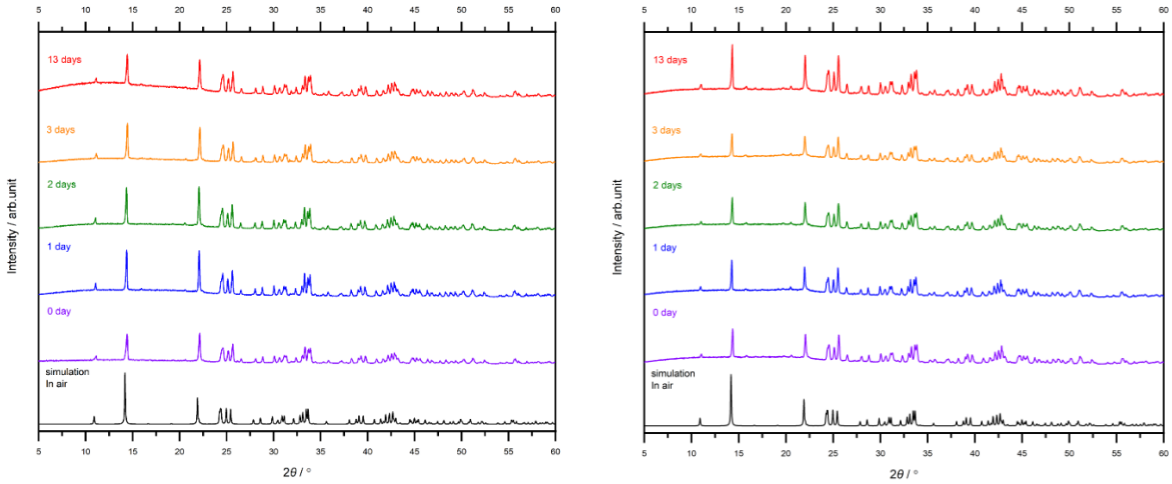

Figure 4.8 Stability of Ca-doped (left) and Sr-doped (right) $La(BO_2)_2Cl$ in air atmospheres. Room-temperature PXRD patterns collected from the borate chloride after 1–13 days of exposure to air atmosphere. No change in XRD patterns was observed under these experimental conditions.

The thermal stability in a flowing N_2 and O_2 gas atmosphere was studied using thermogravimetric and differential thermal analysis (TG-DTA) measurements, $x = 0.1$ and $x = 0.15$ for the Ca-doped and Sr-doped samples, respectively, as these two samples exhibit the highest conductivity. For Ca-doped sample, the TG curve continued to decrease until 700°C, with a mass loss of roughly 2.54% and 3.68% in N_2 and O_2 gas atmosphere, respectively (Figure 4.9). For Sr-doped sample, the TG curve continued to decrease until 700°C, with a mass loss of roughly 3.57% and 4.89% in N_2 and O_2 gas atmosphere, respectively (Figure 4.10). The reason for the mass loss probably due to the lack of purity of the sample. In addition, we

observed a significant decrease in the TG curves of all samples below 150°C, mass loss at this stage accounts for one third of the total, this may be due to the sample adsorbing moisture from the atmosphere during weighing. All samples have no change in the PXRD pattern after the TG measurement, demonstrating the thermal stability of the main phase. (Figure 4.9, Figure 4.10).

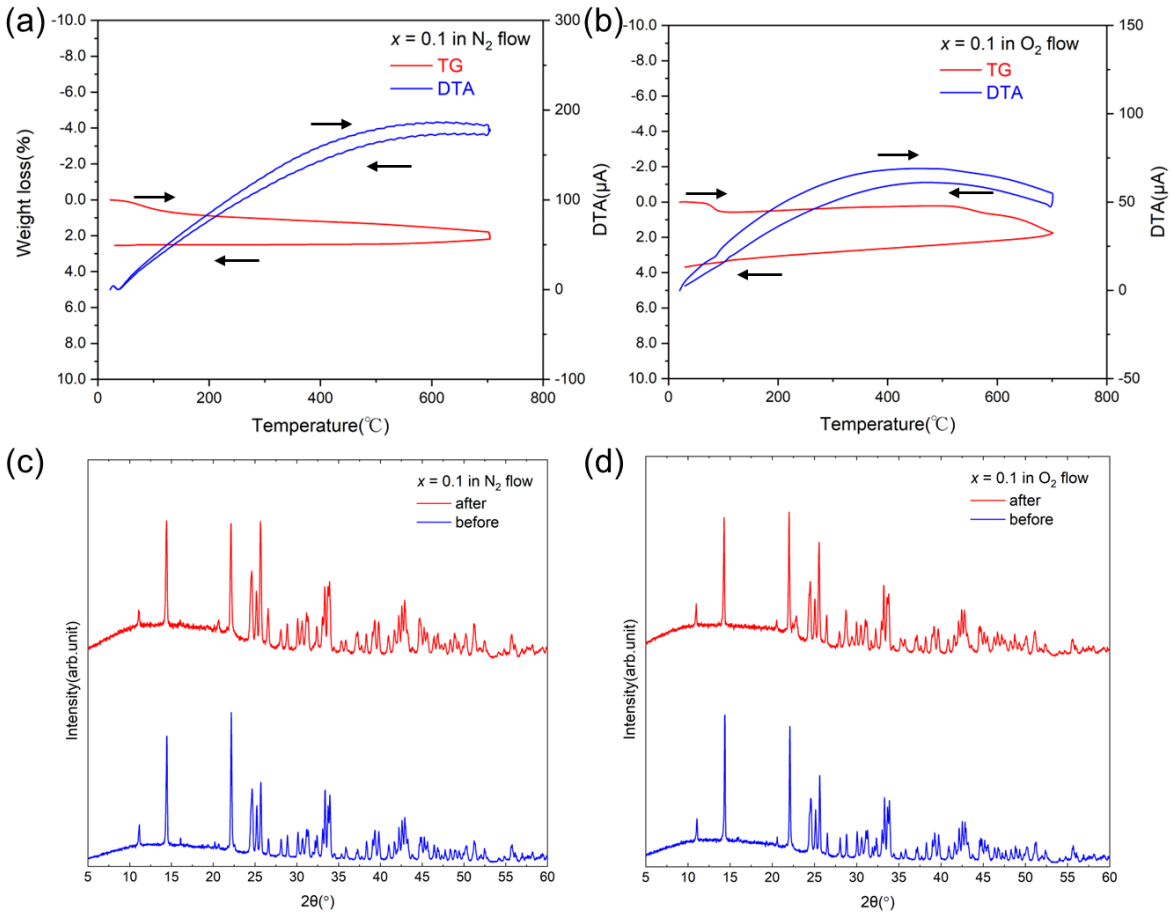

Figure 4.9 (a)(b) TG-DTA curves of Ca-doped $La(BO_2)_2Cl$ in a N_2 and O_2 gas atmosphere. (c)(d) Room-temperature PXRD patterns of Ca-doped $La(BO_2)_2Cl$ before and after the TG-DTA measurements. It remained unchanged after heating up to 700°C in N_2 and O_2 gas.

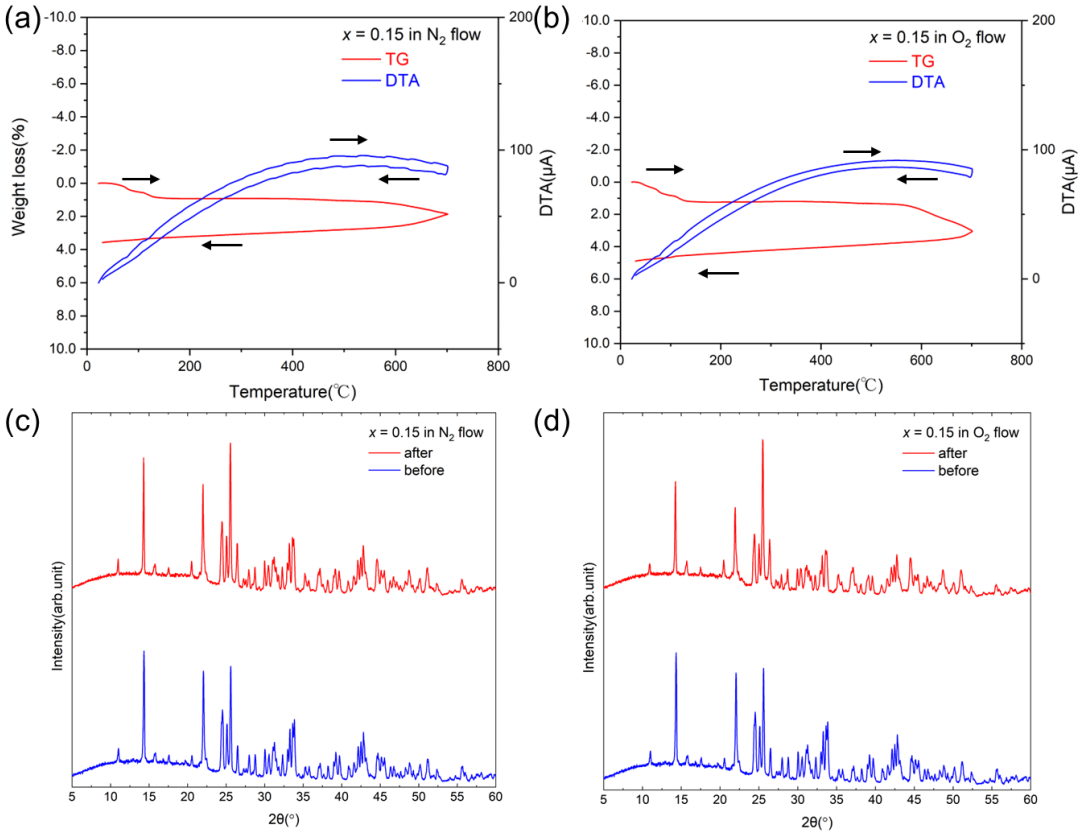

Figure 4.10 (a)(b) TG-DTA curves of Sr-doped $La(BO_2)_2Cl$ in a N_2 and O_2 gas atmosphere. (c)(d) Room-temperature PXRD patterns of Sr-doped $La(BO_2)_2Cl$ before and after the TG-DTA measurements. It remained unchanged after heating up to 700°C in N_2 and O_2 gas.

4.3.4 Conductive property of $(La_{1-x}M_x)(BO_2)_2Cl_{1-x}$ (M = Ca, Sr, x = 0–0.15)

The typical Nyquist plots of $(La_{1-x}M_x)(BO_2)_2Cl_{1-x}$ (M = Ca, Sr, x = 0–0.15) were recorded by impedance methods in an Ar gas atmosphere. The data obtained at 400, 500, 600, and 700 °C are shown in Figure 4.11 and Figure 4.12. For each sample, the plot was fitted using inductance from the electrical wire and equipment (L_0), a total resistance (R_{total}), its constant phase element (CPE_{total}), an electrode-electrolyte interface resistance (R_i), and its constant phase element (CPE_i), where the total components include the contributions from bulk and grain-boundary components.

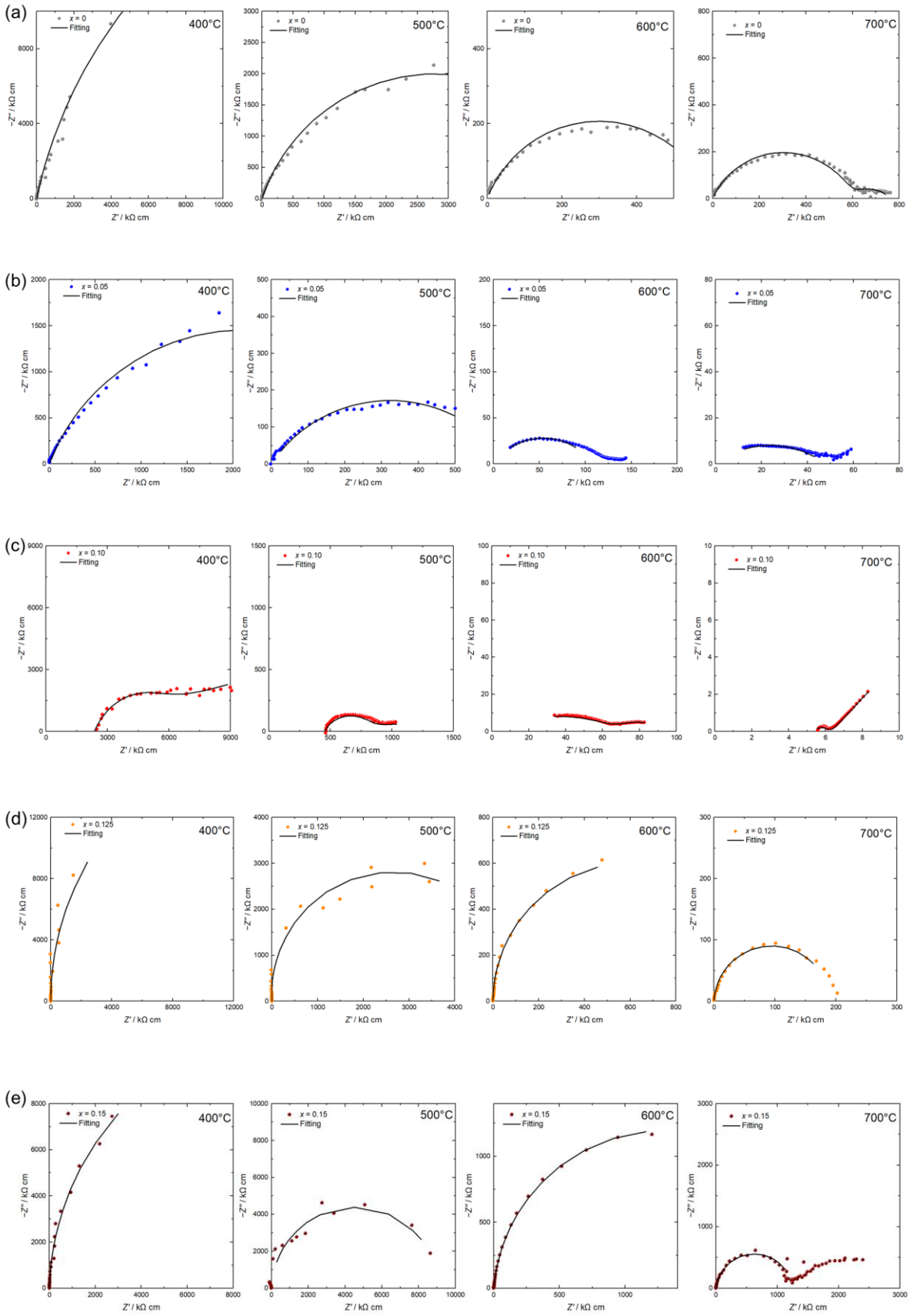
(a)
x = 0
Fitting
400°C
500°C
600°C
700°C
(b)
x = 0.05
(c)
x = 0.10
(d)
x = 0.125
(e)
x = 0.15
-Z'' / kΩ cm
Z' / kΩ cm

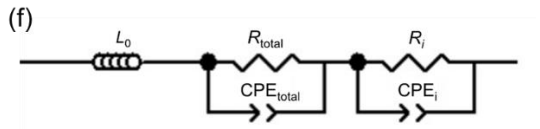

Figure 4.11 (a-e) Representative Nyquist plots of $(La_{1-x}Ca_x)(BO_2)_2Cl_{1-x}$ (x = 0–0.15) solid solutions recorded under an Ar gas atmosphere at 400, 500, 600, and 700 °C in an Ar gas atmosphere. Fitting curves are indicated by black lines. (f) Equivalent circuit model used to fit all data: inductance from the electrical wire and equipment (L_0), a total resistance (R_{total})including bulk and grain-boundary resistances, its constant phase element (CPE_{total}), an electrode-electrolyte interface resistivity (R_i), and its constant phase elements (CPE_i).

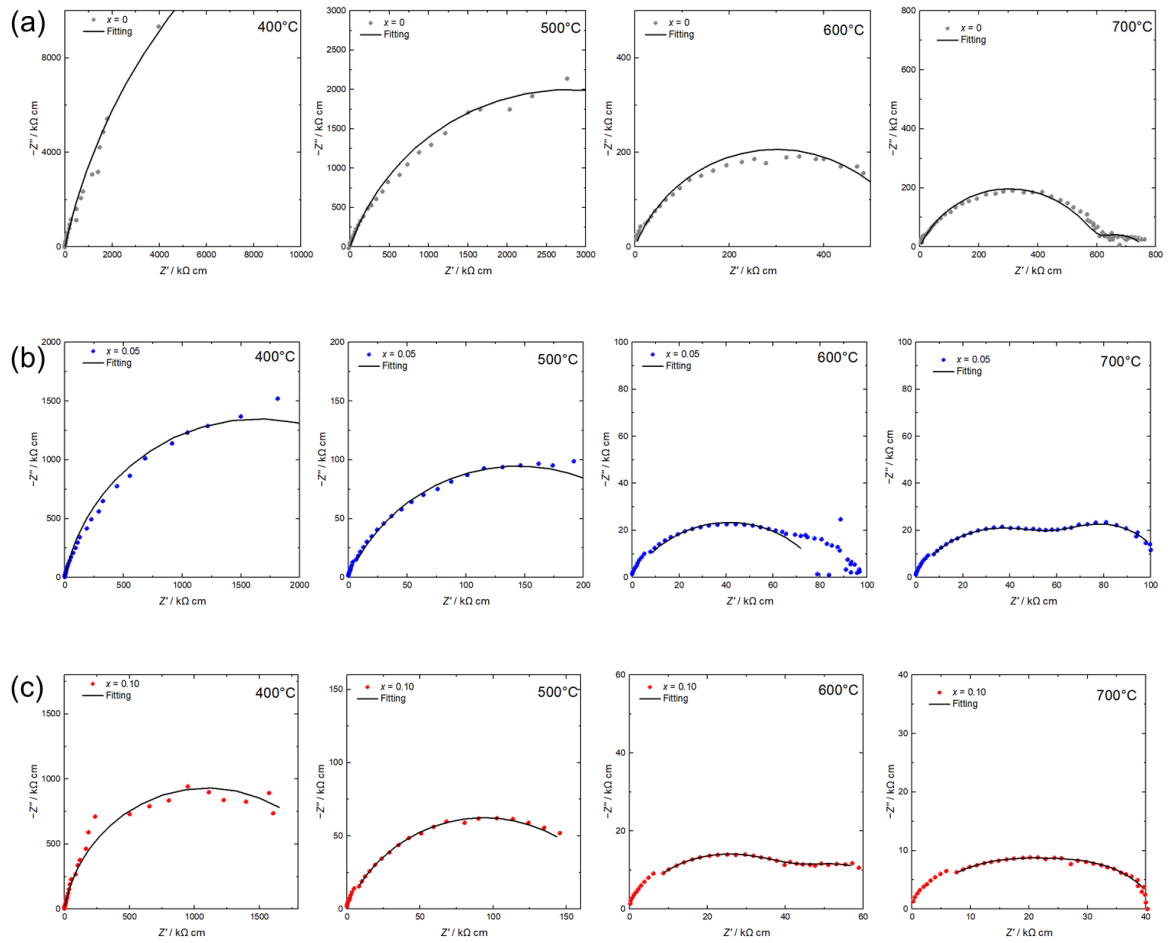

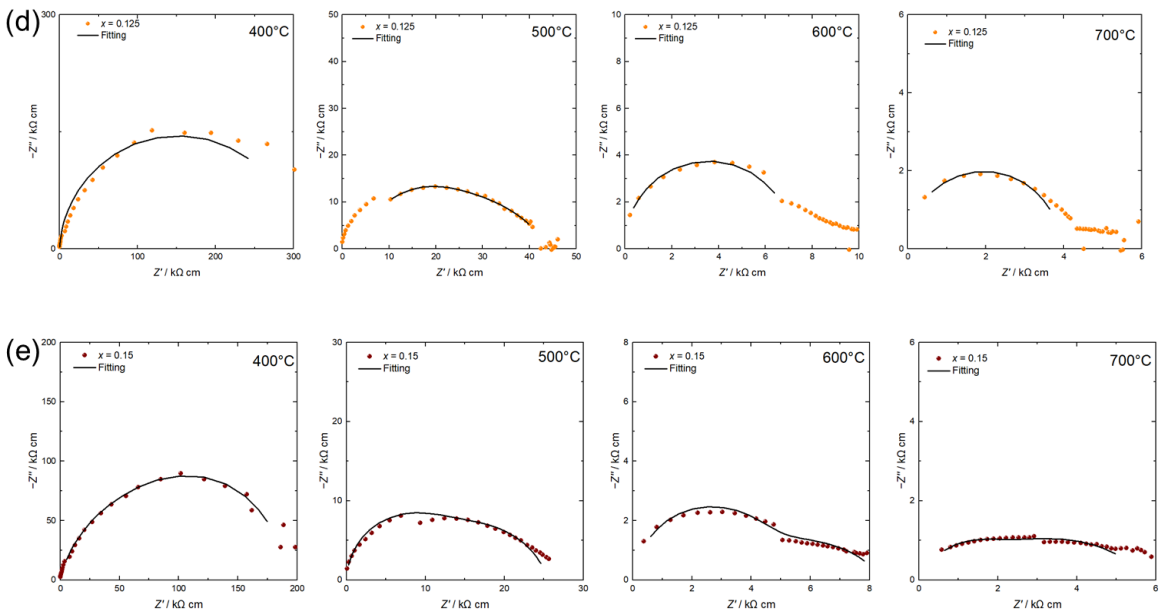

Figure 4.12 (a-e) Representative Nyquist plots of $(La_{1-x}Sr_x)(BO_2)_2Cl_{1-x}$ (x = 0−0.15) solid solutions recorded under an Ar gas atmosphere at 400, 500, 600, and 700 °C in an Ar gas atmosphere. Fitting curves are indicated by black lines. Equivalent circuit model was the same as that of $(La_{1-x}Ca_x)(BO_2)_2Cl_{1-x}$.

The temperature dependence of the ac conductivity (σ_{ac}) of $(La_{1-x}M_x)(BO_2)_2Cl_{1-x}$ (M = Ca, Sr, x = 0–0.15) solid solutions was estimated from the total resistance (Figure 4.13). The σ_{ac} of the undoped phase is comparable to the ionic conductivity of LaOCl at 600–700°C, and on the order of 10^{-5} S cm^{-1} at 700°C. The conductivity of all samples showed a trend positively correlated with temperature. For Ca-doped samples, 10% Ca-doped $(La_{0.9}Ca_{0.1})(BO_2)_2Cl_{0.9}$ exhibited the highest conductivity of 1.84×10^{-4} S · cm^{-1} at 700℃, which was about 30 times higher than that of undoped $La(BO_2)_2Cl$ and higher than $(Ca_{0.95}La_{0.05})_2B_5O_9Cl_{1.1}$, which show the highest conductivity in La-doped $Ca_2B_5O_9Cl$ in the Chapter 3. For Sr-doped samples, 15% Sr-doped $(La_{0.85}Sr_{0.15})(BO_2)_2Cl_{0.85}$ exhibited the highest conductivity of 7.59×10^{-4} S · cm^{-1} at 700℃, which was about 120 times higher than that of undoped $La(BO_2)_2Cl$.

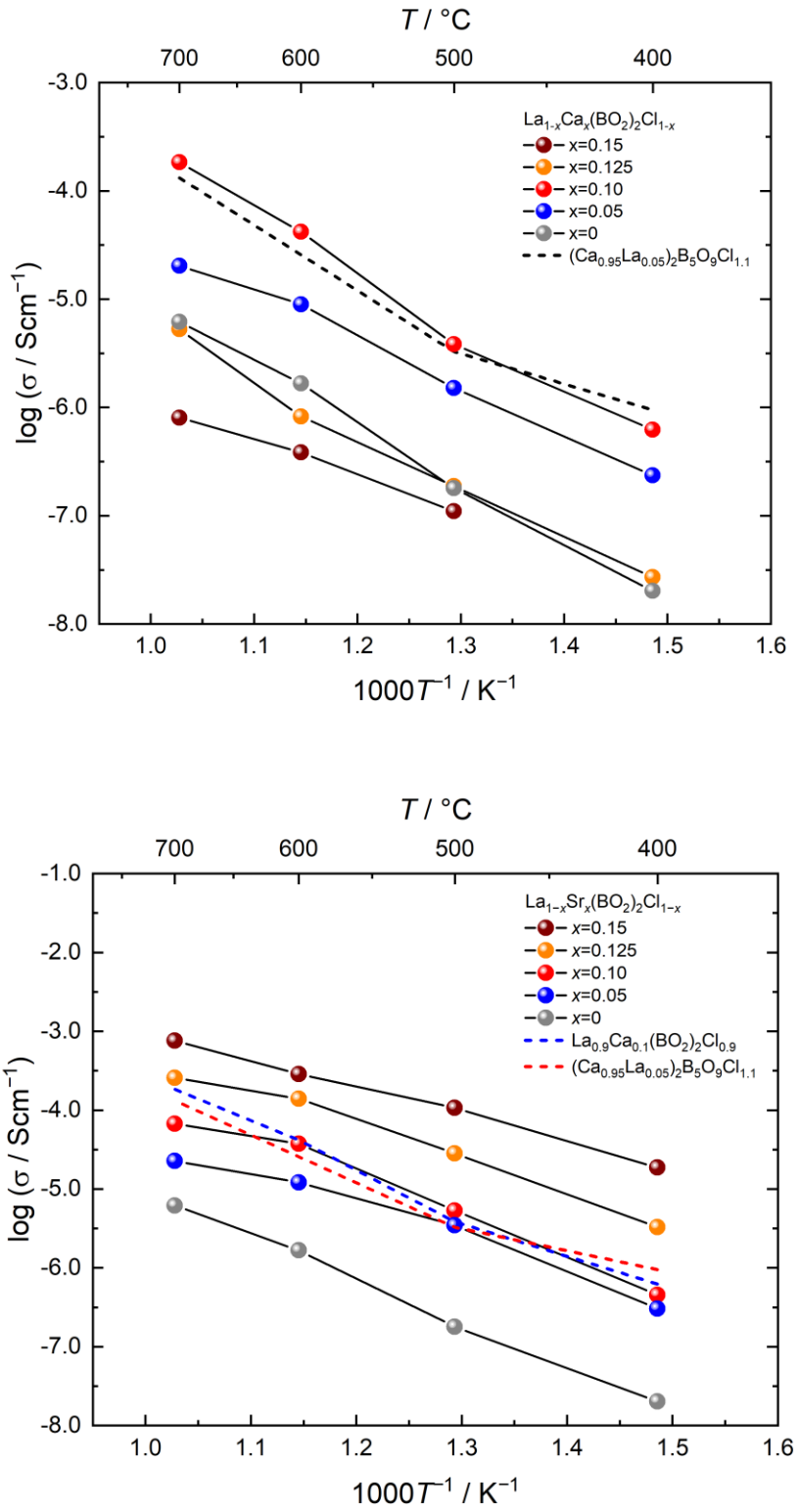

Figure 4.13 Arrhenius plots of the ac conductivity (σ_{ac}) of $(La_{1-x}Ca_x)(BO_2)_2Cl_{1-x}$ (x = 0–0.15) (upper) and of $(La_{1-x}Sr_x)(BO_2)_2Cl_{1-x}$ (x = 0–0.15) (lower) as a function of temperature.

The enhanced conductivity of $(La_{1-x}M_x)(BO_2)_2Cl_{1-x}$ (M = Ca, Sr, x = 0–0.15) can be attributed to the decreased ionic vacancies. However, when x > 0.1, the further increase in the amount of Ca doping tends to reduce the conductivity, which is probably because of the overdoping effects or the excessive ionic vacancies. The activation energy (E_a) of $(La_{1-x}M_x)(BO_2)_2Cl_{1-x}$ estimated using the Arrhenius equation is 1.17, 0.93, 1.16 eV for M = Ca, x = 0, 0.05, 0.10, and 1.17, 1.05, 0.91, 0.76 eV for M = Sr, x = 0, 0.10, 0.125, 0.15, respectively, lower than the La-doped $Ca_2B_5O_9Cl$ which is 1.67, 1.1, and1.21 eV for x = 0, 0.05, and 0.10, respectively. Polarization measurements of $(La_{1-x}M_x)(BO_2)_2Cl_{1-x}$ for x = 0.10 were carried out at 700°C in an Ar gas atmosphere (Figure 4.14). The time evolution of σ_{dc}/σ_{acl}, where σ_{dc} stands for the DC conductivity, exhibited a considerably high degree of polarization (σ_{dc}/σ_{ac} < 0.1 over 30 min), suggesting that ions are the dominant migrating species, not electrons, as expected from its high insulating nature.

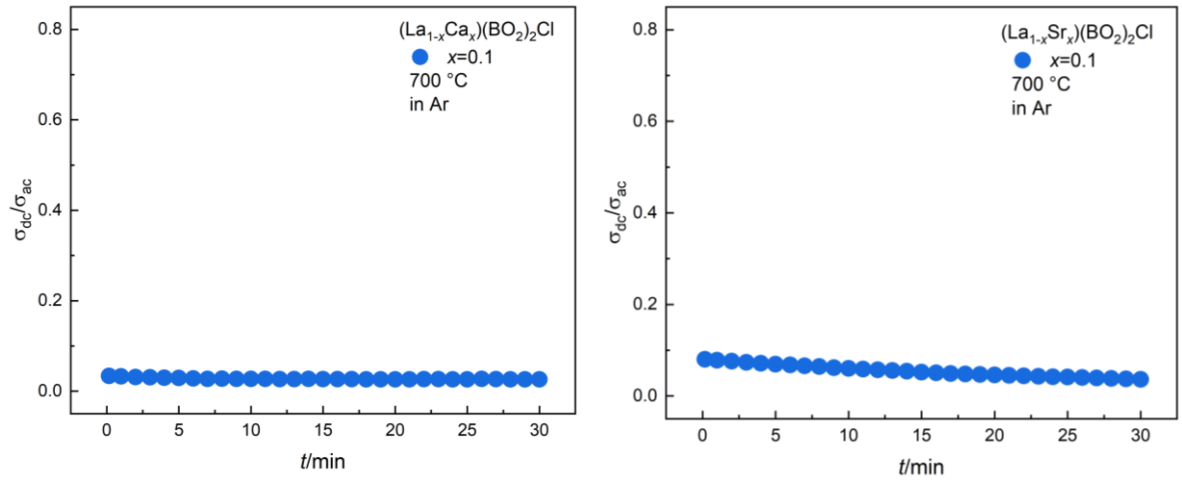

Figure 4.14 Polarization behavior for $(La_{1-x}Ca_x)(BO_2)_2Cl_{1-x}$ (x = 0.10) (left) and $(La_{1-x}Sr_x)(BO_2)_2Cl_{1-x}$ (x = 0.10, 0.125, 0.15) (right) in Ar gas atmosphere at 700°C.

4.4 Summary of Chapter 4

In summary, we prepared a very promising Cl^- ions conductor $(La_{1-x}M_x)(BO_2)_2Cl_{1-x}$ (M = Ca, Sr, x = 0–0.15) with two-dimensional (2D) chloride layers structure, $(B_2O_4)^{2-}$ units connected each other into double triangle by co-point and form a one-dimensional chain along the *a* direction. Difference with most metal chlorides, $(La_{1-x}M_x)(BO_2)_2Cl_{1-x}$ exhibits complete water insolubility and thermal stability until 700°C. Partial substitution of La by doping Ca or Sr, no oxygen vacancies or disorder occurred but Cl^- ion sites show vacancies, which can facilitates Cl^- ions migration. For Ca doping, when x = 0.10, it exhibits the highest ac conductivity of 1.84×10^{-4} S cm^{-1} at 700 °C. For Sr doping, when x = 0.15, it exhibits the highest ac conductivity of 7.95×10^{-4} S cm^{-1} at 700 °C. Both values are higher than that of $(Ca_{0.95}La_{0.05})_2B_5O_9Cl_{1.1}$, suggesting that this is a promising material. DC conductivity for M = Ca, x = 0.10 and M = Sr, x = 0.10, 0.125, 0.15 were also measurement at 700°C in an Ar gas atmosphere, x = 0.10 exhibited a considerably high degree of polarization, suggesting that ions are the dominant migrating species. However, M = Sr, x = 0.125, 0.15, exhibited a not so high degree of polarization, implies the possibility of sample decomposition, even though the main conductive species are ions. This means that its high-temperature conductivity, as well as theoretical calculations of the conductive species, need to be investigated subsequently.

Reference in Chapter 4

(1) Johns, W, D.; Huang, W, N. Distribution of chlorine in terrestrial rocks. *Geochim Cosmochim Ac*, **1967**, *31*, 35–49.

(2) Yudovich, Y, E.; Ketris, M, P. Chlorine in coal: A review. *Int J Coal Geol*, **2006**, *67*, 127–144.

(3) Magenheim, A, J.; Spivack, A, J.; Michael, P, J.; Gieskes, J, M. Chlorine stable isotope composition of the oceanic crust: Implications for Earth's distribution of chlorine. *Earth Planet Sc Lett*, **1995**, *131*, 427–432.

(4) Sakamoto, R.; Shirai, N.; Inoishi, A.; Okada, S. All-Solid-State Chloride-Ion Battery with Inorganic Solid Electrolyte. *ChemElectroChem*. **2021**, *8* (23), 4441–4444.

(5) Murin, I. V.; Glumov, O. V.; Mel'Nikova, N. A. Solid Electrolytes with Predominant Chloride Conductivity. *Russian Journal of Electrochemistry*. **2009**, *45*, 411–416.

(6) Hoshibo, H.; Yamazaki, M.; Nakamura, Y.; Shimoji, M. Ionic Conductivity of Lead Chloride Crystals. *J. Phys. Cos. Jpn*. **1969**, *26*(6), 1422–1426.

(7) Mizusaki, J.; Arai, K.; Fueki, K. Ionic Conduction of The Perovskite-Type Halides. *Solid State Ionics*. **1983**, *11*, 203–211.

(8) Derrington, C. E.; Lindner, A.; Okeeffe, M. Ionic Conductivity of Some Alkaline Earth Halides. Journal of Solid State Chemistry. **1975**, *15*, 171–174.

(9) Choudhuri, S. P.; Bichile, G. K. The Electrical Conductivity and Dielectric Behaviour of Polycrystalline Calcium Fluoride. *Solid State Communications*. **1987**, *64*(6), 993–995.

(10) Xia, T.; Li, Q.; Zhao, X.; Shen, X. Bismuth and Chlorine Dual-Doped Perovskite Chloride as a Phase-Structure-Stable and Moisture-Resistant Solid Electrolyte for Chloride Ion Batteries. *Adv. Mater*. **2024**, *36* (4), 2310565.

(11) Panja, S.; Miao, Y.; Döhn, J.; Choi, J.; Fleischmann, S.; Guddehalli Chandrappa, S.; Diemant, T.; Groß, A.; Karkera, G.; Fichtner, M. Synthesis, Structural Analysis, and Degradation

Behavior of Potassium Tin Chloride as Chloride-Ion Batteries Conversion Electrode Material. *Adv. Funct. Mater*. **2024**, 2413489.

(12) Sakamoto, R.; Shirai, N.; Zhao, L.; Inoishi, A.; Sakaebe, H.; Okada, S. Room-Temperature Operation of All-Solid-State Chloride-Ion Battery with Perovskite-Type $CsSn_{0.95}Mn_{0.05}Cl_3$ as a Solid Electrolyte. *Electrochemistry*. **2023**, *91* (7), 077003.

(13) Verwey, J. F.; Westerink, N. G. Photoconductivity in Lead Chloride and Lead Bromide. *Physica*. **1969**, *42*, 293–302.

(14) Mizusaki, J.; Arai, K.; Fueki, K. Ionic Conduction of The Perovslite-Type Halides. *Solid State Ionics*. **1983**, *11*, 203–211.

(15) Distributed by the Office of Data and Informatics of the National Institute of Standards and Technology, Material Measurement Laboratory, *IUPAC-NIST Solubility Database, Version 1.1* NIST Standard Reference Database 106.

(16) Imanaka, N.; Okamoto, K.; Adachi, G. Y. Water-Insoluble Lanthanum Oxychloride-Based Solid Electrolytes with Ultra-High Chloride Ion Conductivity. *Angew. Chem. Int. Ed*. **2002**, *41* (20), 3890–3892.

(17) Meng, Y.; Nunotani, N.; Shitara, K.; Matsushita, Y.; Imanaka, N.; Yamaura, K.; Tsujimoto, Y. Rational Design of Chloride Ion Transport Channels in an Open Borate Framework. *J Mater Chem A Mater*, **2024**, *12*, 27229–27234.

(18) Tatsumisago, M.; Imanaka, N. ベーシック無機材料科学 化学同人 辰巳砂昌弘, 今中信人. 2021.

(19) Park, M.; Zhang, X.; Chung, M.; Less, G. B.; Sastry, A. M. A Review of Conduction Phenomena in Li-Ion Batteries. *Journal of Power Sources*. Elsevier **2010**, pp 7904–7929.

(20) Tripathi, R.; Gardiner, G. R.; Islam, M. S.; Nazar, L. F. Alkali-Ion Conduction Paths in LiFeSO4F and NaFeSO4F Tavorite-Type Cathode Materials. *Chemistry of Materials* **2011**, *23* (8), 2278–2284.

(21) Umeyama, D.; Horike, S.; Inukai, M.; Itakura, T.; Kitagawa, S. Inherent Proton Conduction in a 2D Coordination Framework. *J Am Chem Soc* **2012**, *134* (30), 12780–12785.

(22) Zhang, H.; Wang, Y.; Ju, S.; Gao, P.; Zou, T.; Zhang, T.; Wang, J.; Xia, G.; Yu, X. 3D Artificial Electron and Ion Conductive Pathway Enabled by MgH2 Nanoparticles Supported on G-C3N4 towards Dendrite-Free Li Metal Anode. *Energy Storage Mater* **2022**, *52*, 220–229.

(23) Ye, C.; Zhang, Z.; Li, J.; Jiang, W.; Ding, G.; Li, W.; Zhang, J.; Huang, L.; Yue, Z.; Zhou, N.; Sun, F. Synergetic Control of Heterogeneous Nucleation and 3D Mixed Electron/Ion-Conducting Paths for Dendrite-Free Li Metal Anodes. *Chemical Engineering Journal* 2023, *462*.

(24) Scerri, E. R. The Periodic Table. *Philosophy of Chemistry*. **2012**, *6*, 329-338.

(25) Scerri, E. R.; Worrall, J. Prediction and the periodic table. *Stud Hist Phi Part C*. **2001**, *32*(3), 407-452.

(26) Wang, Z.; He, J.; Hu, B.; Shan, P.; Xiong, Z.; Su, R.; He, C.; Yang, X.; Long, X. $Ca_2B_5O_9Cl$ and $Sr_2B_5O_9Cl$: Nonlinear Optical Crystals with Deep-Ultraviolet Transparency Windows. *ACS Appl Mater Interfaces*. **2020**, *12* (4), 4632–4637.

(27) Nunotani, N.; Misran, M. R. I. Bin; Inada, M.; Uchiyama, T.; Uchimoto, Y.; Imanaka, N. Structural Environment of Chloride Ion-Conducting Solids Based on Lanthanum Oxychloride. *Journal of the American Ceramic Society* 2020, *103* (1), 297–303.

(28) Imanaka, N.; Okamoto, K.; Adachi, G.-Y. Chloride Ion Conducting Characteristics in Rare Earth Oxychlorides. *Chem Lett*. **2001**, *30*, 130-1.

(29) Okamoto, K.; Imanaka, N.; Adachi, G. Chloride Ion Conduction in Rare Earth Oxychlorides. *Solid State Ionics*. **2002**,154–155:577–80.

(30) Imanaka, N.; Tamura, S.; Okamoto, K.; Adachi, G. Y. Chloride ion conducting behavior of lanthanum oxychloride based solid electrolyte. *Electrochemical Society Proceedings*. **2002-26**, (Solid State Ionics Devices III); 2003: p. 438–43.

(31) Sheldrick, G. M. SHELXT-Integrated Space-Group and Crystal-Structure Determination. *Acta Crystallogr A* **2015**, *71*, 3-8.

(32) Hubschle, C. B.; Sheldrick, G. M.; Dittrich, B. ShelXle: a Qt graphical user interface for SHELXL. *J Appl Crystallogr* **2011**, *44*, 1281-1284.

(33) Dolomanov, O. V.; Blake, A. G.; Champness, N. R.; Schröder, M. OLEX: new software for visualization and analysis of extended crystal structures. *J Appl Crystallogr* **2003**, *36*, 1283-1284.

(34) Nikelski, T.; Schleid, T. $LaCl(BO_2)_2$ Und $Er_2Cl_2[B_2O_5]$: Zwei Chlorid-Oxoborate Dreiwertiger Lanthanide. *Z Anorg Allg Chem*. **2003**, *629* (11), 2028–2033.

(35) Lumbreras, M.; Protas, J.; Jebbari, S.; Dirksen, G. J.; Schoonman, J. *STRUCTURE AND IONIC CONDUCTIVITY OF MIXED LEAD HALIDES PbCl2x Br2(1-x)" II*; 1986; Vol. 20.

(36) Brixner, L. H.; Moore, E. P. *Single-Crystal Refinement of the Structure of LaOCI*; 198.

Chapter 5 General Conclusions and Future Prospects

5.1. General conclusions

In this thesis, three oxychlorides of two different structural types with open borate structure were synthesized. The crystal structures, humidity and thermal stability, chloride-ion conducting properties, and theoretical computations are discussed in detail.

Colorless transparent single crystals of $(Ca_{0.92}La_{0.08})_2B_5O_9Cl_{1.16}$ were grown by the self-flux method using a $CaCl_2$ molten salt. The crystal structure crystallizes in an orthorhombic space group *Pnn*2 with cell parameters a = 11.3807(5) Å, b = 11.3109(6) Å, c = 6.3692(3) Å, and V = 819.88(7) $Å^3$, which is the first to exhibit 1D chloride-ion transport defined by the dimensionality of the borate framework. The aliovalent substitution of La^{3+} for Ca^{2+} causes an increase in the concentration of chloride ions, but no oxygen deficiencies or disorder occurred. The $(Ca_{1-x}La_x)_2B_5O_9Cl_{1+2x}$ (x = 0–0.15) solid solutions were synthesized by using a conventional solid-state reaction, it exhibits the highest conductivity of 1.32×10^{-4} S cm^{-1} at 700 °C when x = 0.05. First-principles molecular dynamics simulations indicate that the predominant chloride-ion conduction is attributed to cooperative diffusion through interstitial chloride sites. Suggesting the rational design of chloride-ion channels and conduction paths based on the dimensionality of the borate framework would provide a new direction for the development of the variety and conducting properties of chemically and thermally stable chloride-ion solid electrolytes.

Colorless transparent single crystals of $(La_{0.82}Ca_{0.18})(BO_2)_2Cl_{0.82}$ with 2D chloride planes were grown by the self-flux method using a B_2O_3 molten salt. The crystal structure crystallizes in a triclinic space group P -1 with cell parameters a = 4.2462(2) Å, b = 6.6321(2) Å, c = 8.2094(3) Å, α = 82.055(3) °, β = 89.230(3) °, γ = 72.055(3) ° and V = 217.725(15) $Å^3$. The aliovalent substitution of Ca^{2+} for La^{3+} causes an decrease in the concentration of chloride

ions, but no oxygen deficiencies or disorder occurred. $(La_{1-x}Ca_x)(BO_2)_2Cl_{1-x}$ (x = 0–0.15) solid solutions were synthesized by using a conventional solid-state reaction, it exhibits the highest conductivity of 1.84×10^{-4} S cm^{-1} at 700 °C when x = 0.10. However, theoretical calculations need further research.

By changing the doped elements, single crystals $(La_{0.8}Sr_{0.2})(BO_2)_2Cl_{0.8}$ of the same structure with Ca-doped were synthesized using the same conditions. The cell parameters is a = 4.2499(3) Å, b = 6.6317(5) Å, c = 8.2099(6) Å, α = 82.097(7) °, β = 89.267(6) °, γ = 72.089(7) ° and V = 217.98(3) Å^3. The introduction of Sr similarly induced a decrease in chloride concentration, rather than in oxygen. $(La_{1-x}Sr_x)(BO_2)_2Cl_{1-x}$ (x = 0–0.15) solid solutions were synthesized by using a conventional solid-state reaction, it exhibits the highest conductivity of 7.59×10^{-4} S cm^{-1} at 700 °C when x = 0.15. However, the stability of the sample and theoretical calculations need further research.

5.2. Future prospects

In this thesis, we have synthesized a series of promising chloride-ion conductors with open borate structures and enhanced their conductivity through the aliovalent substitution of heterovalent elements, which induces an increase or decrease in chloride-ion concentration. Elements in the same group tend to exhibit similar properties, as our future exploration method, we are very interested in developing compounds with the same structure using elements from the same group or period. For example, synthesis of $(Mg/Sr/Ba)_2B_5O_9Cl$ and doping with La/Ce/Pr, synthesis of $(Ce/Pr/Nd)(BO_2)_2Cl$ and doping with Mg/Ca/Sr/Ba. Moreover, alterations in the structure of open borates can also cause disorder in the concentration of chloride ions. For example, in $Ca_2B_5O_9Cl$, the substitution of Al for B may lead to deformation of the chloride channels, promoting chloride migration, while the substitution of Si for B could increase the chloride ion concentration. Finally, to explore the conduction species and

mechanisms, can refer to the study of LaOCl, which uses both experimental and theoretical evidence.[1–6]

Therefore, there are still a lot of possibilities in designing and preparation of new members of chloride-ion conductors, as well as various ways to modify their physical properties.

References in Chapter 5

(1) Nunotani, N.; Misran, M. R. I. Bin; Inada, M.; Uchiyama, T.; Uchimoto, Y.; Imanaka, N. Structural Environment of Chloride Ion-Conducting Solids Based on Lanthanum Oxychloride. *Journal of the American Ceramic Society* 2020, *103* (1), 297–303.

(2) Imanaka, N.; Okamoto, K.; Adachi, G.-Y. Chloride Ion Conducting Characteristics in Rare Earth Oxychlorides. *Chem Lett*. **2001**, *30*, 130-1

(3) Okamoto, K.; Imanaka, N.; Adachi, G. Chloride Ion Conduction in Rare Earth Oxychlorides. *Solid State Ionics*. **2002**,154–155:577–80.

(4) Imanaka, N.; Okamoto, K.; Adachi, G. Y. Water-Insoluble Lanthanum Oxychloride-Based Solid Electrolytes with Ultra-High Chloride Ion Conductivity. *Angew. Chem. Int. Ed*. **2002**, *41* (20), 3890–3892.

(5) Imanaka, N.; Tamura, S.; Okamoto, K.; Adachi, G. Y. Chloride ion conducting behavior of lanthanum oxychloride based solid electrolyte. *Electrochemical Society Proceedings*. **2002-26**, (Solid State Ionics Devices III); 2003: p. 438–43.

(6) Shitara, K.; Kuwabara, A.; Hibino, K.; Fujii, K.; Yashima, M.; Hester, J. R.; Umeda, M.; Nunotani, N.; Imanaka, N. Ionic Conduction Mechanism in Ca-Doped Lanthanum Oxychloride. *Dalton Transactions*. **2021**, *50* (1), 151–156.

List of appended publications

This thesis is based on the following publications.

1. Scientific papers

1. **Y. Meng**, N. Nunotani, K. Shitara, Y. Matsushita, N. Imanaka, K. Yamaura and Y. Tsujimoto, “Rational Design of Chloride Ion Transport Channels in Open Borate Framework”, J Mater Chem A, **12** 27229-27234 (2024) DOI:10.1039/D4TA04624B.

2. Presentation

1. **Y. Meng**, N. Nunotani, Y. Matsushita, N. Imanaka, K. Yamaura and Y. Tsujimoto, “Zeolite-type chloroborate $Ca_2B_5O_9Cl$ as a possible chloride ion conductor”, The 32nd Annual Meeting of MRS-J, Yokohama, Japan (Dec. 5-7, 2022).

2. **Y. Meng**, N. Nunotani, Y. Matsushita, N. Imanaka, K. Yamaura and Y. Tsujimoto, “Synthesis and ionic conducting properties of chloride ion conducting oxychloride”, The Ceramic Society of Japan, The 36th Fall Meeting, Kyoto, Japan (Sept. 6-8, 2023).

3. **Y. Meng**, N. Nunotani, Y. Matsushita, N. Imanaka, K. Yamaura and Y. Tsujimoto, “Synthesis and chloride ion conductivity of a new oxychloride”, The 33rd Annual Meeting of MRS-J, Yokohama, Japan (Nov. 14-15, 2023).

4. **Y. Meng**, N. Nunotani, Y. Matsushita, N. Imanaka, K. Yamaura and Y. Tsujimoto, “New chloride-ion conductor $Ca_2B_5O_9Cl$ with a 3D open borate framework”, The Ceramic Society of Japan, Symposium on Basic Science of Ceramics, Tokyo, Japan (Jan. 7-8, 2024).

5. **Y. Meng**, N. Nunotani, Y. Matsushita, N. Imanaka, K. Yamaura and Y. Tsujimoto, “Synthesis and ionic conducting properties of chloride ion conducting oxychloride”, The

International Conference on the Science and Technology for Advanced Ceramics, Tsukuba, Japan (Feb. 29, 2024).

6. **Y. Meng**, N. Nunotani, Y. Matsushita, N. Imanaka, K. Yamaura and Y. Tsujimoto, "New chloride-ion conductor $Ca_2B_5O_9Cl$ with a 3D open borate framework", International Core-to-Core Symposium on Mixed-Anion Compounds 2024, Nantes, France (Mar. 11-13, 2024).

7. **Y. Meng**, N. Nunotani, Y. Matsushita, N. Imanaka, K. Yamaura and Y. Tsujimoto, "Synthesis and ionic conductivity of a new open-framework layered borate chloride", The Ceramic Society of Japan, The 37th Fall Meeting, Nagoya, Japan (Sept. 10-12, 2024).

8. **Y. Meng**, N. Nunotani, Y. Matsushita, N. Imanaka, K. Yamaura and Y. Tsujimoto, "Synthesis and chloride ion conductivity of a new layered borate oxychloride", Joint Workshop LANL/NIMS Quantum and Functional Materials and MANA International Symposium 2024, Tsukuba, Japan (Oct. 15-17, 2024).

9. **Y. Meng**, N. Nunotani, Y. Matsushita, N. Imanaka, K. Yamaura and Y. Tsujimoto, "Synthesis and chloride ion conductivity properties of $La(BO_2)_2Cl$ with a layered borate oxychloride", The 34th Annual Meeting of MRS-J, Yokohama, Japan (Dec. 16-18, 2024).

Acknowledgement

I would like to express my deepest gratitude to everyone who helped me to complete my PhD study. First and foremost, I gratefully appreciate my supervisor, Professor Tsujimoto Yoshihiro, who has given me a lot of gracious guidance, both academically and in life. It is because of his help that I am able to be interested in research and full of love for life during the past three years.

Second, I would like to express my heartfelt gratitude to Dr. Nunotani Naoyoshi and Professor Imanaka Nobuhito in Osaka University, Dr. Shitara Kazuki in JFCC, Dr. Matsushita Yoshitaka in NIMS. They have helped me with my experiments, and I couldn't have done my research without them.

Besides, I would like to express my heartfelt gratitude to Professor Yamaura Kazunari, Professor Alexei A. Belik. they taught me a lot of useful tips so that I can do my experiments more smoothly. I am also greatly indebted to Mrs. Sakai Etsuko and Mrs. Matsuda Kumiko for the daily affairs. I would like to give my gratitude to Dr. Shirako Yuichi, Dr. Liu Ran, Dr. Yan Hong, Dr. Kang Xun, Dr. Hayashi Hiroaki, Mr. Liang Xuan, Mr. Li Shaoxuan, Mrs. Yuan Hongbo and Mrs. Li Zhijun in our group, they help make my life more colorful.

Lastly, I would like to express my heartfelt gratitude to my family. thanks for their continued support!